

Interpretation of geophysical and geochemical data in a 3D geological model construction of a contaminated site

—A case study at Alingsås drying-cleaning facility, Sweden

HAOYU WEI

FACULTY OF ENGINEERING | ENGINEERING GEOLOGY | LUND UNIVERSITY



Thesis work for Master of Science 30 ECTS

Water Resources Engineering

Interpretation of geophysical and geochemical data in a 3D
geological model construction of a contaminated site

— A case study at Alingsås drying-cleaning facility, Sweden

Tolkning av geofysisk och geokemisk data i en geologisk 3D-
modellerad konstruktion av en förorenad plats

— En fallstudie vid Alingsås tvätter, Sverige

Haoyu Wei

Engineering Geology / Teknisk Geologi

Faculty of Engineering / Lunds Tekniska Högskola

Lund University / Lunds Universitet

Lund 2018

Main Supervisor / Huvudhandledare:

Matteo Rossi, Engineering Geology

Assistant Supervisor / Biträdande Handledare

Torleif Dahlin, Engineering Geology

Examiner / Examiner:

Tina Martin, Engineering Geology

Author:

Haoyu Wei

Title:

Interpretation of geophysical and geochemical data in a 3D geological model
construction of a contaminated site

— A case study at Alingsås drying-cleaning facility, Sweden

Titel:

Tolkning av geofysisk och geokemisk data i en geologisk 3D-modellerad
konstruktion av en förorenad plats

— En fallstudie vid Alingsås tvätteri, Sverige

84 pages + 2 Appendices (4 pages)

65 figures

8 tables

ERRATA CORRIGE

Interpretation of geophysical and geochemical data in a 3D geological model construction of a contaminated site —A case study at Alingsås drying-cleaning facility, Sweden.

Haoyu Wei

Faculty of Engineering, Engineering Geology, Lund University

The first version of this M.Sc. thesis included previously unpublished data that were not yet authorised by the owner for publication. This was due to misunderstandings and miscommunication, which was beyond the control of the author. As a result, proper references for this data were missing. This version of the thesis has been corrected in these respects, and is replacing the first version, which should be discarded in order to avoid it being used by mistake.

Corrections of the manuscript from the version dated 2018-06-19 to the current version dated 2019-03-28 (page numbers refer to the first version dated 2018-06-19):

- Page 17: the sentence
“*The chemical analysis was undertaken by SYNLAB, a leading European laboratory company, on behalf of Department of Geology, Lund University.*”
is changed to
“*The detailed geochemical data of the groundwater samples are unpublished and were kindly provided by Sofia Åkesson, Department of Geology/Lund University, Sweden (S. Åkesson, pers.com., 2018-04-05).*”
- Figure 42:
Removed upper plot, added reference of groundwater data in the caption.
- Figure 43:
Added reference of groundwater data in the caption.
- Figure 44:
Removed groundwater chemistry box in upper plot, added reference of groundwater data in the caption.
- Figure 45:
Added reference of groundwater data in the caption.
- Section 3.3.1 “*Degradation state for groundwater samples*” has been removed, including Table 9, that showed the concentrations of contaminants in groundwater.
- Figure 55:
Added reference of groundwater data in the caption.
- Figure 56:
Added reference of groundwater data in the caption.

- Figure 57:
Added reference of groundwater data in the caption.
- Figure 58:
Added reference of groundwater data in the caption.
- Section 4.2.3 “Groundwater sampling data”.
The last paragraph at page 64 has been removed.
The entire text included from “*In terms of the water quality notes by sampling pipes,...*” to “*...After the temperature calibration, all the pH values oscillate around the neutral level.*”
- Section 4.2.4 “Degradation state”
The first sentence in the last paragraph has been changed from
“*Although some extremely high ratio values can be witnessed both in groundwater samples and in MIP-sounding points, it is really hard to say if these ratios authentically indicate higher natural degradation activities have been going on at these positions.*”
into:
“*Although some extremely high ratio values can be witnessed in MIP-sounding points, it is really hard to say if these ratios authentically indicate higher natural degradation activities have been going on at these positions.*”
- APPENDIX B. “*Appendix iii. Groundwater chemistry data at the Alingsås site.*” and all references to it has been removed.
- APPENDIX C (APPENDIX B in the last version).
Added reference of groundwater data in the caption of figures “Appendix iv” (now Appendix iii), “Appendix v” (now appendix iv) and “Appendix vi” (now appendix v).

Interpretation of geophysical and geochemical data in a 3D geological model construction of a contaminated site

— A case study at Alingsås dry-cleaning facility, Sweden

Abstract:

The Alingsås dry-cleaning facility is one of the heavily halogenated hydrocarbon contaminated sites in Sweden. The source of contamination dates back to the 1970s when a large scale tetrachloroethylene leakage outbreaked inside the dry-cleaning building. After years of propagation and dissemination, the tetrachloroethylene together with its degradation products was widely found in soil and groundwater at the site. Although no drinking water source is located in the contaminated zone, the potential risk due to the spreading plume cannot be neglected in a long run. Albeit, the natural self-cleaning potential was demonstrated by the previous investigations, the whole process can be enhanced and accelerated by the engineered biological remediation. Funded by Formas, SGU, and Tyréns, the “MIRACHL” project is set up to realize the monitoring of in-situ bio-geochemical remediation process with electrical imaging tomography. The first pilot injection of remediation products was conducted in November 2017.

This master’s thesis work serves as a part of the “MIRACHL” project. In this thesis work, a refined three-dimensional conceptual model was built up via GeoScene3D, a 3D geological modelling software. The three-dimensional model consists of terrain surface, interpolated bedrock surface, interpolated groundwater surface, soil and groundwater chemistry data, borehole logs, as well as geophysical data. Of them, the geophysical data came from the 2D inversion results of electrical resistivity and induced polarization (DCIP) measurements along four buried horizontal arrays. The DCIP measurements data were collected before the first pilot injection.

Through the visualization in GeoScene3D, it can be clearly seen that most halogenated hydrocarbons concentrate on the lower part of the unconsolidated layer, closely situated to the bedrock surface. In the latest set of measurement, the highest tetrachloroethylene concentration body was found nearby the source of leakage. The highest concentration bodies of trichloroethylene and *cis-1,2-dichloroethene* are situated at the same location with a slight difference in elevation. Vinyl chloride generally has a relatively low concentration level at the site, but a zone with extremely high concentration level was found at the northern edge of the measurement zone. Also, the concentration of halogenated hydrocarbons in groundwater samples is much lower than that measured via Membrane Interface Probe soundings (MIP-Soundings). Three possible reasons were assumed for such phenomenon: diffusional limitation, temperature factor, and contaminants multi-phase pattern. The DCIP inversion results were also correlated with the superposed geological and geochemistry reference data. However, no strong correlations were found between halogenated hydrocarbons and the DCIP responses due to the varieties of factors such as the phase pattern of the contaminants. In spite of this, several changes are expected to be seen in the inversion results after a couple of time steps, due to the boosted biological degradation process after the first pilot injection as well as the injection itself. However, due to the limited information provided, it is not possible to predict these changes at this stage.

Keyword: Halogenated hydrocarbon, Geophysics, DCIP, GeoScene3D, Groundwater chemistry.

Subject: Engineering Geology

Haoyu Wei, Division of Engineering Geology, Faculty of Engineering, Lund University, John Ericssons väg 1, SE-223 63 Lund, Sweden. E-mail: ha3527we-s@student.lu.se

Acknowledgements

The two-year master's programme in Water Resources Engineering has come to an end with this master's thesis work carried out at the Division of Engineering Geology, Lund University in Sweden. These two years' living in Sweden will become the endless motivation for the rest of my life, both mentally and physically. What this country offered me is more than the education itself, but a new perception of living.

I felt my great honour to have chosen this thesis work and be able to contribute to the "MIRACHL" project. I would like to show my sincere appreciation to my supervisors Matteo Rossi and Torleif Dahlin for good supervision. Also, I am extremely grateful to Torleif Dahlin for offering me the precious chance to take a training course of GeoScene3D at the headquarter office of I-GIS, in Aarhus, Denmark. The part of the work with Geoscene3D was supported by the European Union, Eurostars Programme, together with Innovation Fund Denmark and The Swedish innovation agency Vinnova under the project "Mapping Geology in Cities" (E10096 MAGIC).

I also want to thank Le Thanh Vu and Tom Martlev Pallesen at I-GIS for providing patient tuition and helpful guiding. I would also like to thank Aris Nivorlis at the Division of Engineering Geology for giving me some inspirations for the thesis work. A special thank should also be given to Pontus Nordberg, Sophie Gruschka, and Clemens for supporting me during the hard time.

A special thanks to Sofia Åkesson, Geology Dept., Lund University, for the access to some of her unpublished groundwater data.

Last but not least, I want to thank my parents Qing He and Jianxuan Wei for encouraging and supporting my studies at Lund University, Sweden.

Table of contents

1. Introduction.....	1
1.1 The Contaminated Lands	1
1.2 MIRACHL Project.....	2
1.3 Research questions and objectives	3
1.4 Outline.....	3
2. Methods & Site Description	4
2.1 Site Overview.....	4
2.1.1 History and field installations	4
2.1.2 Geological settings.....	7
2.1.3 Hydrogeological conditions	12
2.2 Dense Nonaqueous Phase Liquids (DNAPLs).....	13
2.3 Geochemical Methods.....	15
2.3.1 MIP-Sounding Probe	15
2.3.2 Multilevel Groundwater Sampling Pipes	17
2.4 Geophysical Methods.....	17
2.4.1 Theoretical backgrounds of DCIP measurements.....	18
2.4.2 Theoretical backgrounds of DCIP inversion.....	25
2.4.3 Field measurement settings	26
2.5 GeoScene3D	31
3. Results	33
3.1 Interpolated Bedrock surface and Groundwater Free Surface	33
3.2 Contaminants: three-dimensional distribution	35
3.2.1 Vertical slices over Profile 1 – 5	36
3.2.2 Horizontal slices over Alingsås site	47
3.2.3 Iso-surfaces generated for the Alingsås site.....	52
3.3 Degradation State for MIP-sounding Measurements	53
3.4 DCIP inversion results	54

3.4.1 Inversion results along line 1	56
3.4.2 Inversion results along line 2	57
3.4.3 Inversion results along line 3.....	59
3.4.4 Inversion results along line 4.....	60
4. Interpretation & Discussion.....	62
4.1 Interpolated surfaces	62
4.2 Contaminants three-dimensional distribution	64
4.2.1 Assessment of the 3D interpolation of MIP-soundings	64
4.2.2 Contaminants Distribution features	65
4.2.3 Groundwater sampling data	66
4.2.4 Degradation state	67
4.3 DCIP inversion results	68
5. Conclusions and Recommendations.....	71
5.1 Conclusions.....	71
5.2 Recommendations.....	71
Reference	72
Appendix A. 3D Vision Clips in GeoScene3D	I
Appendix B. Vertical Slices Along the Cross-section	IV

1. Introduction

1.1 The Contaminated Lands

The chemical industry has been playing an important role in the economic chain, simultaneously affecting other sections of society such as agriculture, environment, and construction. Also, due to the widespread use of chemicals, together with the globalization trend, the worldwide raising demand has been pushing the manufacture of chemical compounds. Such expansion of the chemical fabrication is a double-edged sword. On one hand, such tendency can enhance the chemical engineering industry so as to boom the economy. On the other hand, inevitably has it increased the exposure of human beings, animals, and even the whole eco-system to all kinds of chemical substance (Milieu Ltd, 2017). Even though the exposure to chemicals does not necessarily indicate the danger or hazard, a large number of chemicals without thorough evaluation or proper disposal before emission have been risking the environment through the contacts with air, soil, and water. Even worse, the complexity of the water-soil-air system makes it rather harder to assess the future risk level (Cairney, 2002). Specifically, uncertainties such as whether the introduced chemical is bonded with the soil, and whether the groundwater flow will affect the chemical mobility, will all contribute to the unpredictability of the consequences. In spite of this, the relatively high liability of potential risk and threat caused by those hazardous chemicals cannot be neglected. Furthermore, evidence has shown a high concentration of hazardous chemicals is eroding our daily life. For example, a high concentration of cadmium were found in human's kidney, polychlorinated biphenyls (PCBs) being found in breast milk (Naturvårdsverket, 2012)

To better cope with such potential risks, the assessment and registration of contaminated land were initiated in Europe and North America, which dates back to the late 1970s (Cairney, 2002). Since then, increasing attention and focus has been put on perfecting the registration of contaminated sites as well as conducting site remediation. For example, Sweden is putting this focus into action to reach a 'Non-Toxic' environment by 2020. However, the difficulty of the situation makes this objective unachievable. To be more exact, in Sweden, there are around 25,000 hazardous sites have been found and more sites are being assessed and evaluated. Among those, approximately 1000 of them are classified as seriously polluted (risk class 1) and about 7000 sites are categorized as risk class 2 indicating a less polluted level (Lundin, 2017). In addition to a large number of contaminated sites, the remediation projects witness a rather slow progress with merely about 43 ongoing projects annually (Lundin, 2017). Such slow progress is not caused by the lack of funding since every year approximately 550 million SEK is allocated to the contaminated sites remediation projects (Lundin, 2017). Instead, the various contaminants together with the complex soil-water-air environments make every contaminated site unique (Cairney, 2002). Amid all kinds of contaminants found at the contaminated sites in Sweden, the primary contamination is heavy metals with a proportion of 45%, followed by Halogenated hydrocarbons (30%), Polycyclic Aromatic Hydrocarbon (PAH) (10%) and Oil (10%) (Figure 1).

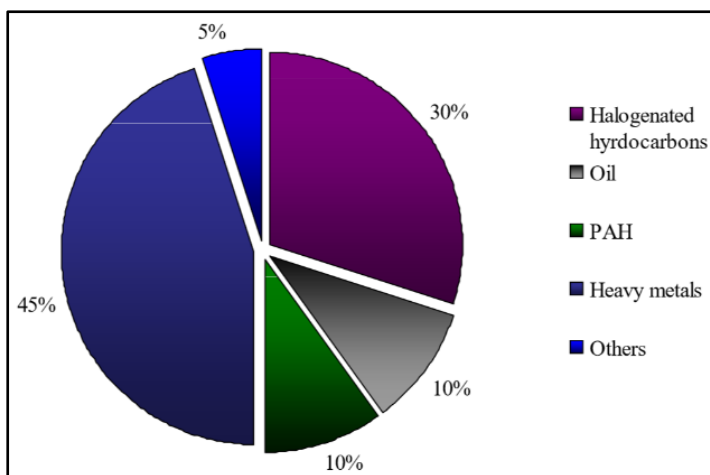


Figure 1. Distribution of the most common contaminants among contaminated sites in Sweden (Naturvårdsverket, 2005).

In recent years, growing focus has been put on the remediation of the sites contaminated by Halogenated hydrocarbons (Usually chlorinated hydrocarbons). These chlorinated hydrocarbons usually appear as tetrachloroethene (PCE) and trichloroethene (TCE) at the sites together with their accumulated degradation products. The application of PCE and TCE had a rather prosperous market which can be categorized into dry-cleaning, metal-cleaning, and vapour degreasing with 80%, 15%, and 4% occupation in the whole production amount in the 1950s (Doherty, 2000). Especially in dry-cleaning, the merits such as the nonflammability as well as its outstanding performance in degreasing without swelling and shrinking the fabric made it a perfect product at that time (Linak E, 1992). In Sweden specifically, although up to 50% of the PCE and TCE employed in dry-cleaning industry was replaced by chlorofluorocarbons (CFO) in the 1980s, PCE and TCE were used as a primary detergent for fairly a long time ever since 1950s (Travier et al., 2002).

The disputation and research about the health effect caused by these halogenated hydrocarbons never ended. Extensive experiments and investigations aimed at figuring out the possible carcinogenicity of these halogenated hydrocarbons were carried out in the USA and Nordic countries. The overall evaluation classified the chlorinated hydrocarbons by the risk of carcinogenicity level (Table 1). National concentration standard for these halogenated hydrocarbons in drinking water was also set up though it differed from country to country. For example, in Sweden, the maximum allowed concentration for PCE and TCE together is 10 µg/l and the maximum allowed concentration for Vinyl chloride (VC) is 0.5 µg/l (Livsmedelsverkets, 2017), but no standard set for Cis-1,2-Dichloroethene (cDCE). By contrast, the maximum allowed concentrations for PCE, TCE, and VC are 5 µg/l, 5 µg/l, and 2 µg/l respectively (EPA, 2009).

Table 1. The cancer classification of PCE and its degradation products (IARC, 2015). The classification groups meanings: 1 – Carcinogenic to humans, 2A – Probably carcinogenic to humans, 2B – Possibly carcinogenic to humans, 3 – Not classifiable as to its carcinogenicity to humans.

	PCE	TCE	DCE	VC
Cancer Classification group	2A	2A	3	1

1.2 MIRACHL Project

In terms of the remediation approaches, the widespread method adopted in Sweden is usually excavation-and-refilling. Such a method is rather straightforward: digging out the contaminated soil and transporting to an appointed facility for the further soil treatment. Albeit, the main three shortcomings cannot be neglected. Firstly, the possible exposure to human beings during soil transportation cannot be underestimated (Suer and Andersson-Sköld, 2011). Secondly, the substantial expense of excavation makes it unrealistic to be applied in all the cases. Apart from that, the micro-

ecological damage to the local environment also goes against the purpose of the remediation. In contrast, the in-situ remediation approaches are becoming more popular because they are less expensive and eliminate the second-time exposure. Plus, the high oxidation state of the chlorinated hydrocarbons makes them easily degraded under biological metabolism process (Chen, 2004). This provides the possibility of carrying out in-situ bioremediation at the chlorinated hydrocarbons polluted site.

In spite of the promising condition for carrying out in-situ bioremediation, the strong need for comprehensive monitoring and verification of in-situ remediation arises simultaneously (MIRACHL, 2017). Accordingly, the 'MIRACHL' (full name: Characterisation and Monitoring of In-situ Remediation of Chlorinated Hydrocarbon Contamination Using an Interdisciplinary Approach) project was founded to improve the understanding of in-situ remediation processes through a series of monitoring approaches. Such combined approaches for monitoring and verification of in-situ remediation are applied at three sites in Kristianstad, Alingsås, and Hagfors. The monitoring approaches involve interdisciplinary methods such as biogeochemistry, geophysics, as well as isotopic analysis. According to the task allocation, the Division of Engineering Geology of Lund University has undertaken the geophysics related issues, mainly dealing with the geoelectrical tomography.

The purpose of geoelectrical tomography is to achieve a profound understanding of the subsurface in an economical way. Specifically, the approaches used to derive the information of the subsurface can be principally categorized into two types. The first one is referred to as invasive methods such as drilling, digging, tunnelling. These invasive methods can usually provide precise information of the near-surface zone. However, the significantly high cost of these methods may prohibit the use at the site over a long period. In addition to the relatively high cost, there is also a high risk of spreading out the contaminant vertically (Johansson et al., 2015). By contrast, the non-invasive methods such as resistivity and induced polarization can yield an integral imaging of the subsurface through quantified observations of subsurface electrical properties (Styles, 2012).

1.3 Research questions and objectives

On the whole, this master's thesis work serves as a part of the 'MIRACHL' project, dealing with a three-dimensional geological model construction of the baseline data at the Alingsås site. To be more exact, this research has three main objectives. The first objective is to conduct Direct Current resistivity (DC) and Induced Polarization (IP) data processing and inversions of the baseline measurement via Res2Dinv (commercial software for the fast 2D resistivity and IP inversions). Those DCIP data comes from the measurements before the injection of remediation products. The second objective is to merge all the derived data into a three-dimensional model via GeoScene3D (a three-dimensional geological modelling software). These derived data mainly include two-dimensional DCIP inversion results, the borehole logs, the soil and groundwater geochemistry data via groundwater sampling pipes and Membrane Interface Probes (MIP-soundings), and terrain surface. The third objective is to conduct the interpretation of all the data in the geological model and see if any correlations can be concluded.

1.4 Outline

The outline of this master's thesis is as follows: Chapter 2 introduces the geological and hydrogeological conditions of Alingsås site, as well as the detailed description of the methods adopted in field measurements. The DCIP inversion theories, and inversion procedures adopted in this thesis work are also included. Chapter 3 presented the main results, while the corresponding interpretations and discussions can be found in chapter 4. Chapter 5 contains conclusions of this master's thesis work and recommendations for the future project work.

2. Methods & Site Description

This chapter will firstly discuss the site history, local geological settings, and hydrogeological conditions to achieve a comprehensive overview of the investigated site. Secondly, this chapter will conclude the critical chemical and physical properties of main halogenated hydrocarbons, followed by the detailed description of the geochemical and geophysical measurements, including the measurements theories and how they were conducted in the field. The introduction to the main modelling software GeoScene3D is also included in this chapter.

2.1 Site Overview

2.1.1 History and field installations

The following site description was mainly translated from Haglund (2010). Alingsås, the investigated site for this master's thesis work, is located in the western part of Sweden. The specific study area is 'Alingsås tvättereri', a dry-cleaning facility, located in Kristineholm's industry region, about 1.5 kilometres east of the Alingsås city centre. Both the overview map of Alingsås as well as the orthophoto of the specific study area are displayed in [Figure 2](#).

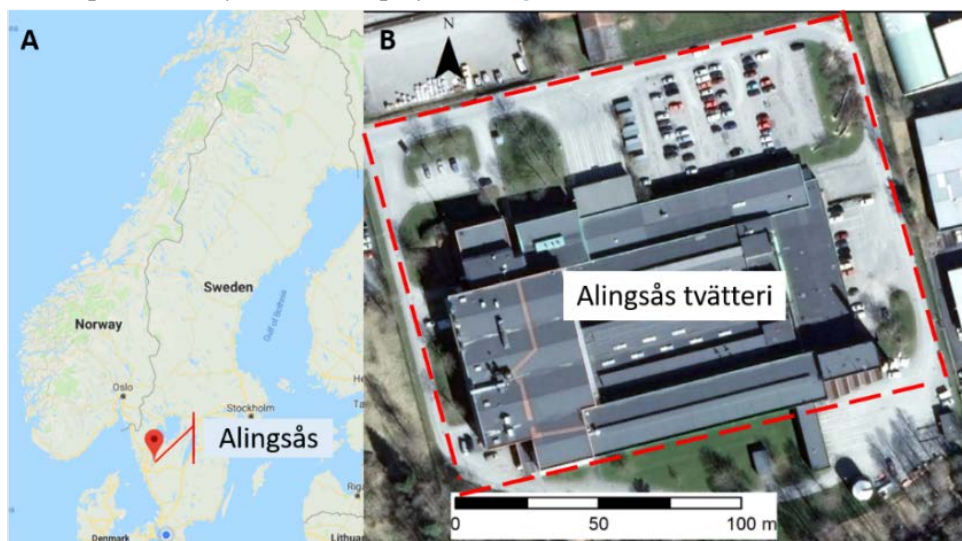


Figure 2. A) displays the national map of Sweden with a highlight on Alingsås location. © Google Maps. B) is the orthophoto of the study area in Alingsås where a dry-cleaning facility has been running for years.

'Alingsås tvättereri' was put into operation in the early 1960s. This facility used to employ large amounts of PCE in its operation, which was one of the most widespread solvents employed in the dry-cleaning industry. These PCE solvents were initially stored in several different tanks in this facility. In the 1970s, a large-scale leakage of these PCE solvents, up to 200 litres, occurred inside the facility. The leakage partially poured down into a floor drain which was connected to a smaller concrete-made collection basin in the basement. In reaction to the emergency, the basin was then sealed instantly according to the rule, leaving a layer of PCE on the bottom (Haglund, 2010). Even though the leakage from the tanks had been stopped, the worry remained that the leftover PCE substance may further seep from the concrete basin into soil and groundwater according to experience from similar leakage accidents in

other sites. Unfortunately, such worry was subsequently substantiated by two consulting companies (J & W, ÅF) in 2002 and 2004 respectively. Chlorinated hydrocarbons were found both in the soil and groundwater through the comprehensive environmental field investigation conducted at the Alingsås site. Specifically, the results of the investigations indicate that the contaminants plume is about 70 meters to 100 meters long with the widest section of 30 meters (Haglund, 2010).

In 2006, Swedish Geotechnical Institute (SGI) was commissioned by Sveriges Geologiska Undersökning (SGU) to estimate the capability of natural self-cleaning in the contaminated aquifer at the Alingsås site. The survey through the analysis of the geochemical parameters such as acidity, nitrite, and methane, indicated an anaerobic to strong anaerobic condition at the site. Such a condition is the prerequisite for microbials to reduce these chlorinated hydrocarbons (Haglund et al., 2012). Despite this, the natural self-degradation process is believed to last for a long time. It is estimated to take approximately 29 years before the average concentration of PCE reaches the safe value and 50-60 years before the concentration of PCE degradation products reaches the acceptable level (Haglund et al., 2012). Accordingly, to accelerate the remediation process, the enhanced (engineered) biological degradation process is recommended at the Alingsås site.

During the periods 6th-15th of November and 27th November – 5th December in 2017, the pilot test injection work was implemented by Ejlskov, a Danish consultancy company and WSP, a Swedish consultancy company. The distribution of injection wells is illustrated in Figure 3. As it is indicated, the injection test was carried out in two sub-areas with two different commercial products within the contaminated zone. Both products were injected between 3.5 meters below ground level (m bgl) to 7m bgl (refer to Figure 4). Note that, such elevation range of injection was provided with a relatively rough estimation. While carrying out the injection at the Alingsås site, the injection wells were drilled until they reached the bedrock. In area A, the injection products were CAT100TM which basically consists of BOS100® (granular activated carbon, GAC), a slow release electron donor, a process catalytic as well as chlorinated hydrocarbon degrading microorganisms. In addition to these, Provect-CH4® was added at the injection site. Provect-CH4® is a type of Methane Inhibitor, serving as a type of nutrient resource for microorganisms. It can also enhance the dehalorespiration (ZVI, 2016). In area B, the injection products were ERD-CH4TM, together with the bioaugmentation and microbes. Before this injection, the anaerobic microbial consortium (SDC-9) had been installed in each injection holes. In all, the remediation effects of these two products will be evaluated and compared in approximately 6 months. The further full-scale remediation plan will be developed based on the conclusion drawn from this pilot test injection (EJLSKOV, 2017).



Figure 3. Distribution of injection wells in the contaminated zone. The purple dashed-line marks out the estimated plume shape according to the previous investigation conducted by WSP. The red rectangular zone is where the initial leakage took place. The dashed arrow with an eye represents the 3D vision angle in Figure 4.

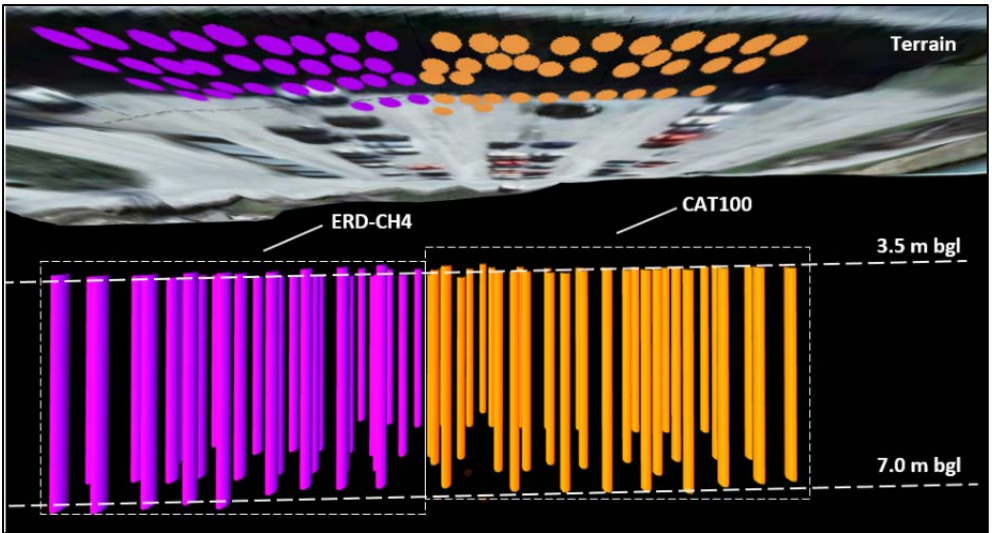


Figure 4. 3D Vision of injection wells of two type of substance in GeoScene3D.

In addition to the pilot injection wells, instruments for other field investigations were also installed. These investigations include groundwater sampling pipes, MIP-sounding points, borehole logs, and DCIP horizontal measurement lines. The location for these installations can be referred to Figure 5.

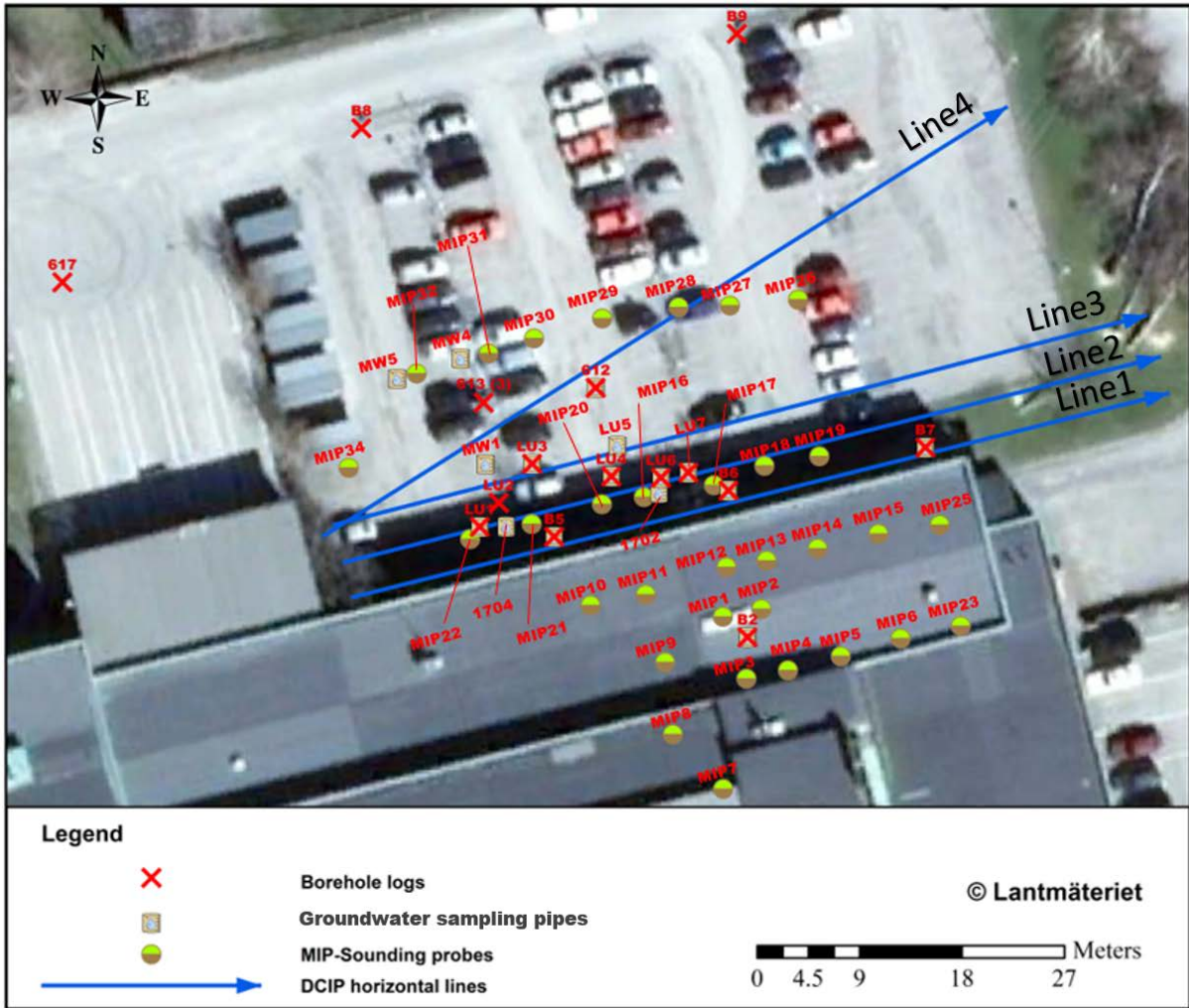


Figure 5. Overall measurement installations at the Alingsås site, including MIP-sounding, Groundwater sampling, borehole logs, and DCIP horizontal lines. Note that some borehole logs overlap with groundwater sampling pipes. These borehole logs were recorded while installing these groundwater sampling pipes.

2.1.2 Geological settings

Figure 6 displayed the local quaternary deposits map. The Alingsås dry-cleaning facility building is marked out with a red five-pointed star. As can be noticed, the Alingsås dry-cleaning facility building is situated at the boundary between postglacial sand and glacial clay.

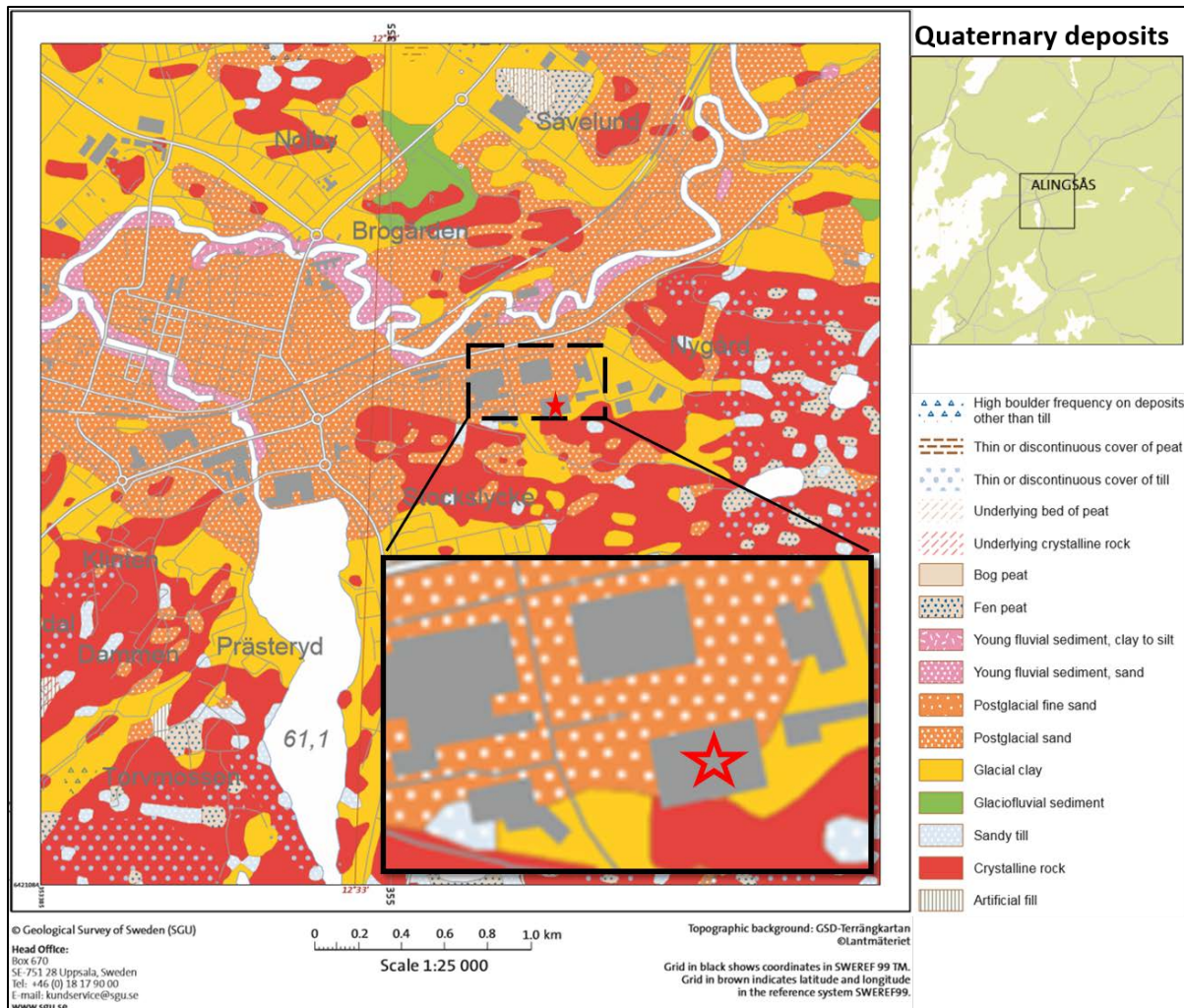


Figure 6. Quaternary deposit map over Alingsås at scale 1: 25 000, mapped by SGU, showing the surface and near-surface distribution of different soil types. The Alingsås dry-cleaning facility building is marked with a red five-pointed star. © Sveriges Geologiska Undersökning.

Although no bedrock drilling and sampling was conducted at the Alingsås site, the bedrock information provided by SGU showed that the local bedrock mainly consists of acidic intrusive rock (e.g. granite, granodiorite, and monzonite). As a type of acidic intrusive rock, it consists of relatively higher siliceous material, which tends to have a generally lower pH value (Glasgow, 2007). Also, the comparatively slower formation process of this type of igneous rock yielded coarser textures such as dykes, sills, and laccoliths (Gill, 2010). Such features offer the convenience for the contaminants to move deeper into bedrocks once they fully penetrate through the unconsolidated layer. However, whether the obvious coarser textures exist in this case still remains to be seen.

The topography of the investigated area is rather flat with a maximum surface elevation variation of 7 meters. A rough presentation of the topography variation at the Alingsås site can be seen in Figure 7. The southern part of the investigated area is higher than the northern part.

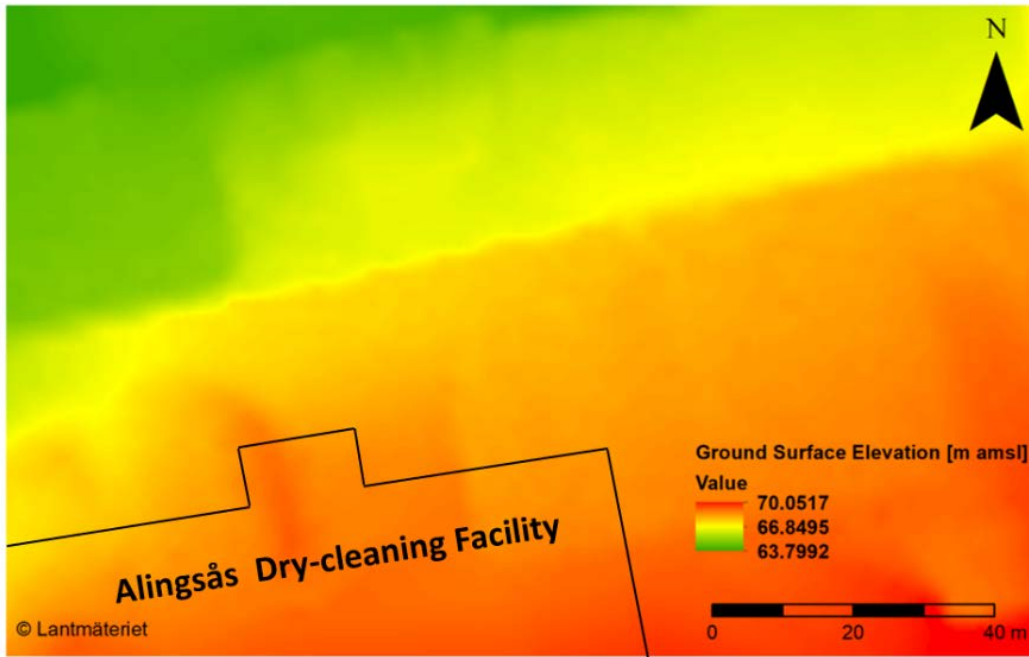


Figure 7. Ground surface elevation map. © Lantmäteriet.

Figure 8 displays the interpolated isolines of the soil depth variation over the area. The soil depth data was collected during the previous investigations at the site. Overall, the upper part of the bedrock shows an lean-northward trend, which is reasonable considering the topography of the region (Engelke, 2007).

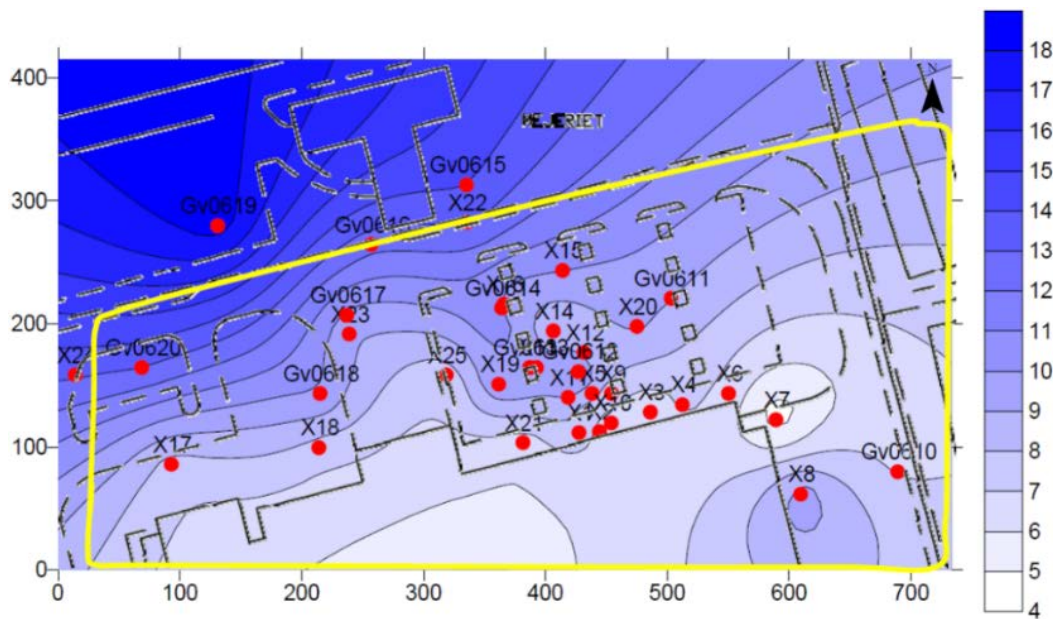


Figure 8. Isolines of depth in meters from the ground surface down to the upper surface of bedrock. Red points represent the original bedrock depth data. Contour lines generated by kriging in the program Surfer (Golden Software). The area within the yellow solid line shows a horizontally uniform surface area (Engelke, 2007).

The layers information was mainly provided by those 15 borehole logs with valid recorded global coordinates (Figure 5), conducted by different institutes and companies. The borehole logs for 612, 613 and 617 were conducted by EJLSKOV. B2, B5, B6, B7 and B9 borehole logs were carried out by J&W, a Swedish energy, and environment company. LU-series borehole logs were managed by Tyréns AB, a Swedish consultancy company. The borehole logs were then put into the GeoScene3D and the 3D vision clip can be referred to Appendix i.

Table 2. Geo-symbols for borehole logs in GeoScene3D.

Geo symbol	Layer description	Geo symbol	Layer description
Fsa	"Fine Sand"	Sa_so_	"Sand with some topsoil"
clFSa	"clayey Fine Sand"	saSo	"sandy Top soil"
siFSa	"silty fine Sand"	sagrSo	"sandy gravelly Top soil"
Sa	"Sand"	grCSa	"gravelly coarse size Sand"
Msa	"Medium Sand"	grSa	"gravelly Sand"
MSa_cl_	"Medium Sand with somewhat clay"	clsiSa	"clayey silty Sand"
clSa	"clayey Sand"	saGr	"sandy Gravel"
Sa_cl_	"Sand with somewhat clay"	MsaGr	"medium sandy Gravel"
Sa_Fcl_	"Sand with somewhat fine size clay"	Cl_Gr_Sa	"Clay, gravel, sand"
clsiSa	"clayey silty Sand with somewhat clay"	Sa_saGr	"Sand, Gravel, much water"
Sa_Si_Gr	"Sand, silt, gravel"	siCldc	"silty Dry rusty clay"
Mg_C_	"Concrete"	siCl	"silty Clay"
Mg_As_	"Asphalt"	Cldc	"Dry clay"
Pr	"Plant Remains"	saFCl	"sandy fine Clay"
Ro	"Bedrock"	FsaCl	"Fine sandy Clay"
sagrCl	"sandy, gravelly Clay"	FCl_sa_	"Fine size Clay with somewhat sand "
siCl_Fsa_	"silty Clay with somewhat fine sand"	Cl_si_	"Clay with silt layer"
FsiCl_pr_	"mulled silty Clay with somewhat plant remains"	Cl	"Clay"
sasiCl	"sandy silty Clay"	FCl	"Fine size Clay"
FsasiCl	"Mulled sandy silty Clay"		

Table 2 displays the geo-symbols adopted in GeoScene3D for the visualisation of borehole logs. The geo-symbols are compiled based on SGF (2016), abbreviation system for soil and bedrock.

The 15 borehole logs, derived from the Alingsås site, are displayed in

[Figure 9](#). In general, in each borehole, at the site, the subsurface can be roughly divided into 4 to 5 layers. The composition of the top layers varies from each other according to spatial characteristics. For instance, the top layer of borehole B2 is made of concrete, which is likely because of the filling due to its position inside the facility building. The top layers of boreholes outside the building within the parking lot area, such as B8, B9, LU2, LU3, and LU4, are mostly made of asphalt. Exceptions such as borehole 612, 613 and 617 might be caused by the different standards adopted to the geological description by different companies. The thin layer of man-made asphalt might be neglected in the geological logging. The core material of the second layers is clay with varying content of sand and gravel. The composition of the third layers is relatively cluttered with different combinations of sand of various sizes, gravel, silt and occasionally some clay. The thickness of the third layers varies largely as well, ranging from 0.05 m (LU7) to 4.1 m (613). In some borehole logs such as LU6, an elevation gap can be noticed between the surface of the ground and the surface of the top layer. This might be due to the inaccuracy of the terrain surface. The terrain data provided by Lantmäteriet was updated in 2009. This data set is in the form of regular grids with 2-meter resolution, which is a little bit too rough for such a small site. The surface changes during these years, as well as the insufficient resolution, could explain the elevation gap error.

In addition to the naturally-formed geological units, utilities (storm-water pipes) are also reported to be existing at the Alingsås site. Although no detailed information of these storm-water pipes was provided, location of these pipes was inspected at the site and can be referred to [Figure 10](#), and the estimated depth of pipes is around 1.8 meters below the ground surface. The diameter of the storm-water pipes is assumed to be 1 meter, in order to input the storm-water pipes into GeoScene3D ([Appendix ii](#)).

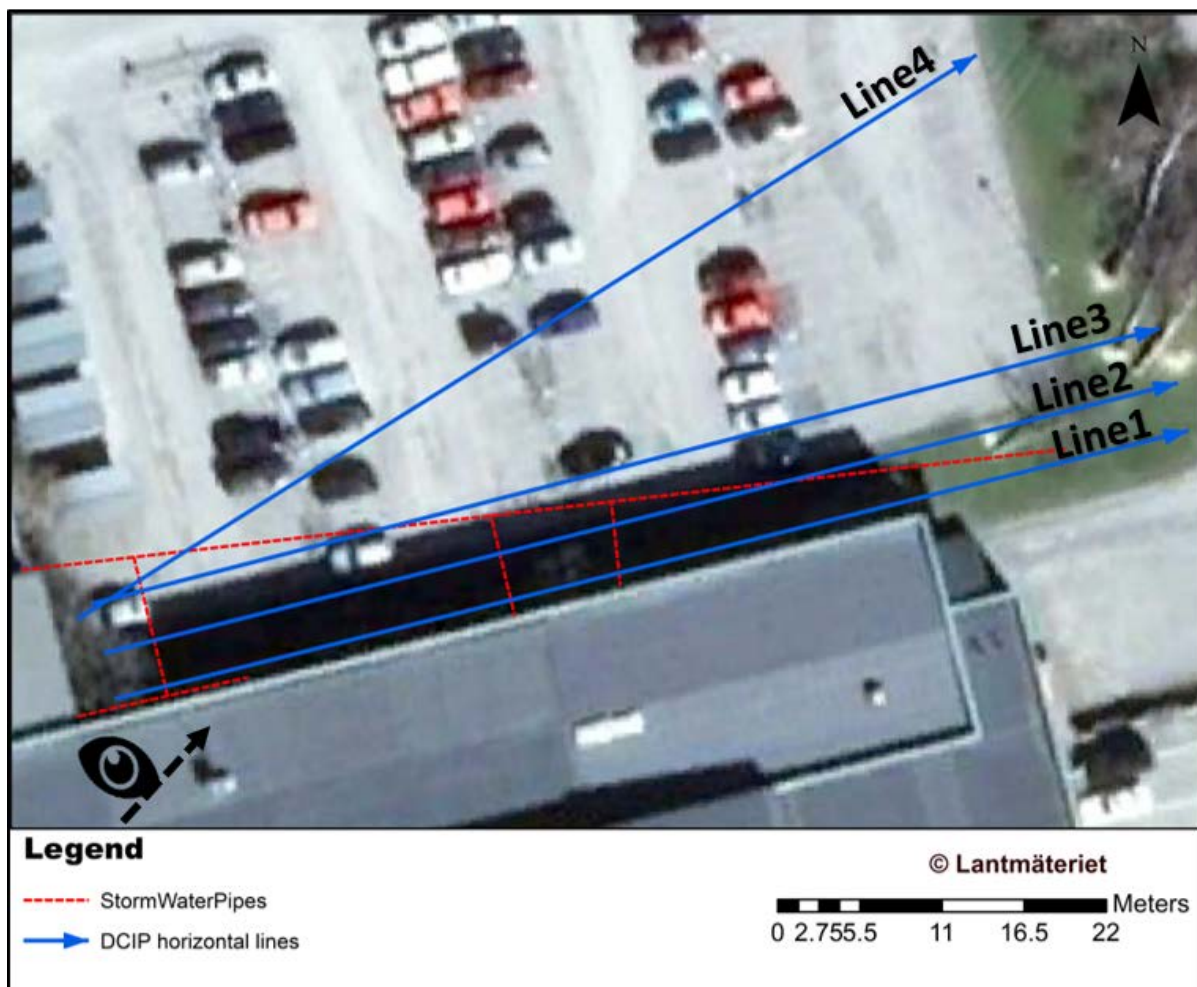


Figure 10. Approximate location of Storm-water pipes. These pipes have a lot of crossing points with four DCIP lines. The dashed-arrow with an eye marks out the 3D vision angle in [Appendix ii](#).

2.1.3 Hydrogeological conditions

According to the site stratigraphic description in section 2.1.2, based on the site borehole logs, the middle low-pervious clay layer makes aquifer at the Alingsås site likely characterized as the confined or leaky confined aquifer. However, whether it is leaking confined or not depends on the authentic attribute of the clay layer. In some cases, according to the field borehole logs (

Figure 9), the clay layer appears as a layer of dry clay (for example B6) or silty dry clay (for example B5). The fractures existing in the dry clay makes it a leaky confined aquifer, which provides the chance to drain the surface water (precipitation for example) to the aquifer. In addition to the dry clay layer, in some boreholes such as 612 and 613, the mixing of coarser material with clay may also contribute to the leaking potential. Depending on fractures and alteration of the bedrock, shallow zone of the bedrock layer could potentially hold some storage of the groundwater.

A previous investigation conducted by WSP (on April 28th, 2017; see WSP, 2017) also looked into the hydrogeological condition of the Alingsås site. Figure 11 illustrates the groundwater equipotential lines as well as the flow direction with a gradient of 0.005-0.01. The flow rate in the sand layer is estimated to be 50-200m/year and the flow rate in fractured clay layer is estimated to be 0.1-0.5 m/year (WSP, 2017). The reason for the groundwater depression zone witnessed around MW4 point remained unknown, but it was suspected to be caused by the problematic borehole itself. The groundwater levels of eleven groundwater sampling wells were also inspected during the most recent groundwater sampling activity at the Alingsås site (October 4th, 2017). The groundwater surface was subsequently interpolated and put into the final refined geological model.

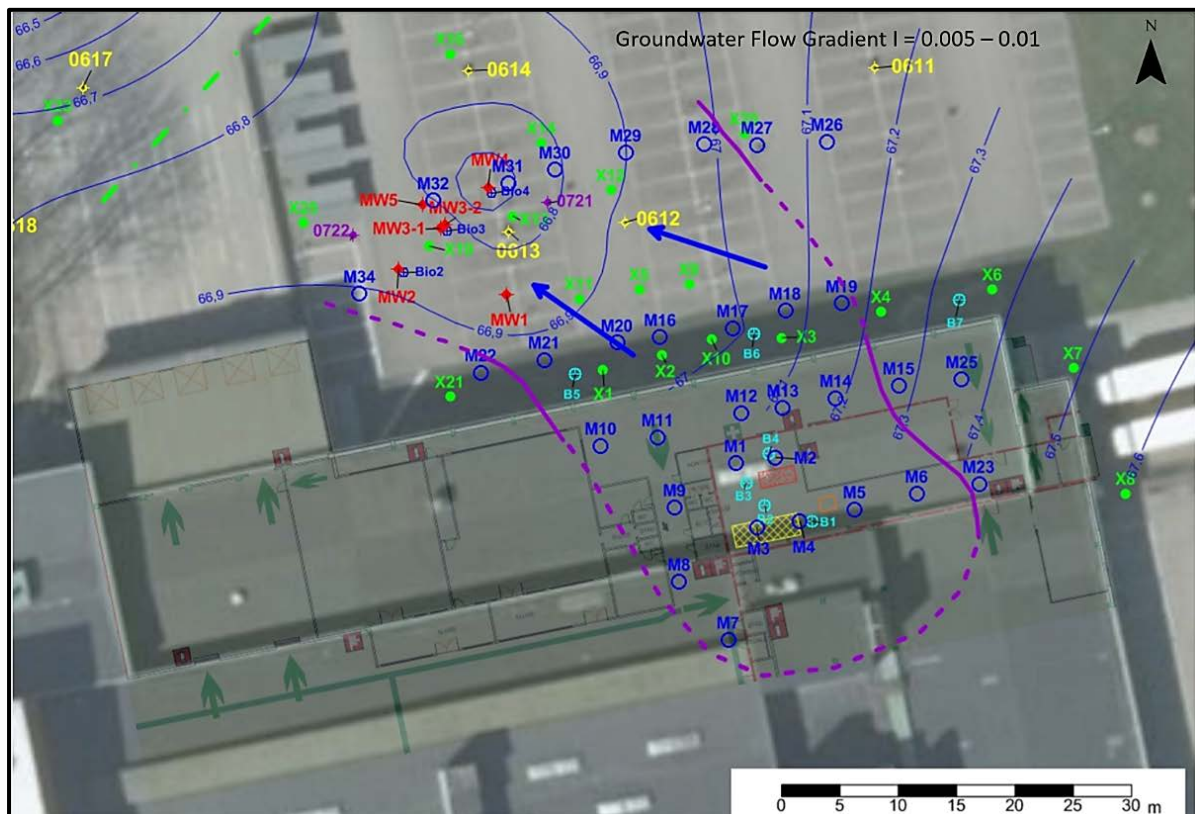


Figure 11. Groundwater equipotential lines and a depression zone around MW4 point can be evidently witnessed. Blue arrows represent the groundwater flow direction. Purple solid and dashed lines depict the estimated contaminant plume shape at the Alingsås site. Figure modified from WSP (2017).

2.2 Dense Nonaqueous Phase Liquids (DNAPLs)

Chlorinated hydrocarbons are characterized by liquids heavier than water, slight solubility in water, and low viscosity (Jia et al., 1999). The quantified description of these mentioned characteristics of the chlorinated hydrocarbons can be referred to [Table 3](#).

Table 3. Some of the chemical and physical parameters of four prevalent chlorinated hydrocarbon compounds, modified from Huling and Weaver (1991).

Vapour Compound	Density [kg/m ³]	Dynamic Viscosity 20°C [pa•s]	Solubility 25°C [mg/L]	Henry's Constant [pa]	Colour	Molar mass [g/mol]
PCE	1.625	0.89	206	14	Colourless	165.83
TCE	1.462	0.57	1280	58.7	Colourless	131.4
cDCE	1.248	0.467	3500	200	Colourless	96.95
VC	0.911	/	2700	/	Colourless	62.5

These physical features can make a big difference to the specific behaviours of those chlorinated hydrocarbons in the subsurface. For example, the dynamic viscosity has a great impact on the hydraulic conductivity of a specific type of liquid. In general, the dynamic viscosity indicates the resistance of the liquid to flow, which is mainly caused by the cohesion between the liquid molecular and the media surrounding the liquid. In Equation (2.2.1), capital K [m/s] denotes the hydraulic conductivity, lower case k [m²] denotes the intrinsic permeability, ρ [kg/m³] denotes the fluid mass density, g [m/s²] denotes the gravity, and the μ [pa•s] stands for the dynamic viscosity. As can be implied from this equation, the liquid with higher density and lower dynamic viscosity, in comparison with the water (1.0016 Pa•s at 20 °C), tends to bear a higher hydraulic conductivity than water. Consequently, the dense chlorinated hydrocarbons have a higher potential of mobility by contrast with water.

$$K = k * \rho * g / \mu \quad (2.2.1)$$

Consequently, the high potential of mobility of the dense chlorinated hydrocarbons makes it even harder to predict the flowing path of them in the subsurface. In addition to this hydrological feature of the dense chlorinated hydrocarbons, the different concurrent phases, and the variable stratigraphic units also complicate the situation of the chlorinated hydrocarbons contaminated sites.

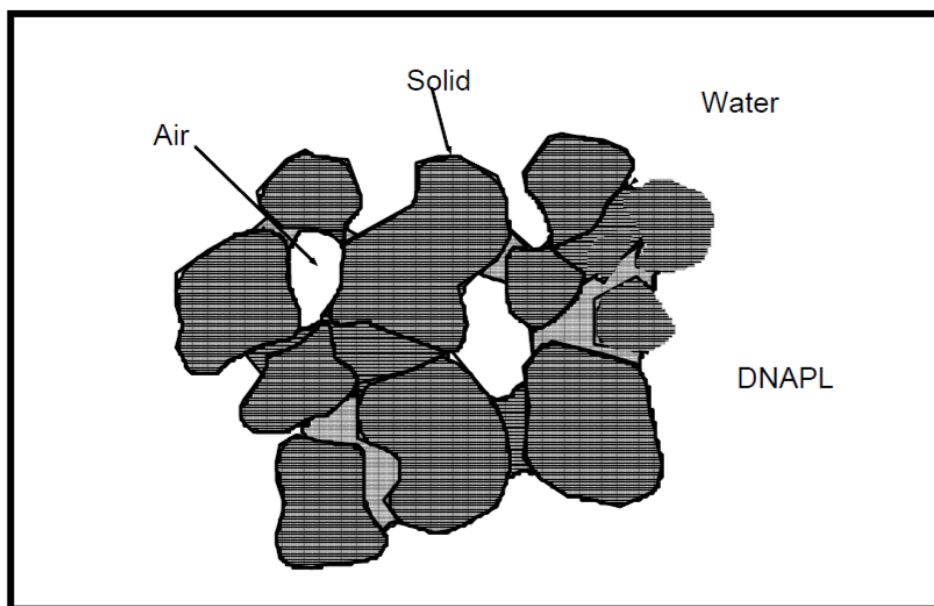


Figure 12. Four phases of the chlorinated hydrocarbons of a DNAPLs contaminated unsaturated zone. The contaminants appear in all possible combinations among these four phases (Huling and Weaver, 1991).

The four phases of the chlorinated hydrocarbons include the volatilized vapour existing in the pores among geological units, absorbed in the soil, solubilized in the groundwater, and immiscible DNAPLs without any mixture with surrounding media (Huling and Weaver, 1991). As can be noticed from Figure 12, the contaminants can appear with a sole phase or the combination of all four phases (the most complex case). Also, phase pattern of the DNAPLs existence can also be converted by location and time within the same chlorinated hydrocarbon contaminated site. However complex the pattern is, the characterization of the existing pattern of the chlorinated hydrocarbon contaminant is believed to contribute a lot to the understanding of the site as well as the planning for the future remediation.

Figure 13 depicted one of the typical models which describe how the leaching DNAPLs develops in the subsurface with the groundwater passing through. The relatively high density of the contaminants causes them to vertically settle down in the aquifer. The low viscosity makes it possible for them to rapid mix and spread out in the soil, groundwater, rock cracking. After a certain period, the contaminant can diffuse to the passing by groundwater (Lerner et al., 2003), or penetrate the layers and further seep into the bedrock. Huling and Weaver (1991) did a considerably complete description of the all possible patterns of the DNAPLs dissimilation in the subsurface. Some of them are involved in the discussion in association with the situation at the Alingsås site.

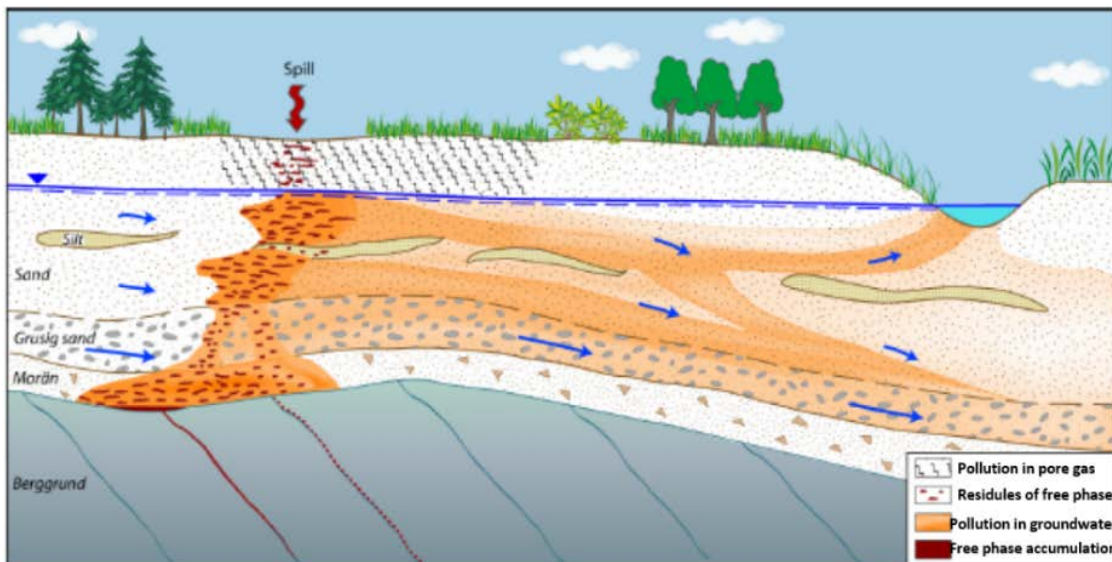


Figure 13. Conceptual sketch of how chlorinated hydrocarbons can develop in the ground. Blue arrows present groundwater flow directions. Figure modified from Haglund et al. (2012).

2.3 Geochemical Methods

At the Alingsås site, extensive geochemical explorations were carried out via mainly MIP-sounding probes, as well as groundwater sampling pipes. The results concluded from these measurements helped to gain a thorough knowledge of the contaminants concentration distribution. These data were also incorporated into the final refined geological model via GeoScene3D and correlated with geophysical measurement results.

2.3.1 MIP-Sounding Probe

A Membrane Interface Probe (MIP) is an environmental probe for fast in-situ detection of volatile hydrocarbons (including chlorinated components) (Bennett et al., 2010). Depending on the types of sensors it is equipped with, MIP-sounding can qualitatively characterize different parameters and substance in soil and groundwater. Figure 14 displays how MIP-sounding works in operation. The whole MIP-Sounding system consists of two parts: gas chromatograph placed on the ground, and the membrane interface probe installed in the soil (Geoprobe-Systems®, 2018). The probe has a heating plate which can be heated to approximately 120 °C and it is put adjacent to the semipermeable membrane. As the probe is in contact with the groundwater or soil, the heating plate will thus evaporate and sublime the surroundings. At a specific time point, the volatile contaminants can be released from the ambient soil and diffuse through the semipermeable membrane into the measurement system. The gas carrier (usually nitrogen) will thus carry the contaminant into the gas chromatograph and the content of the contaminant can be analyzed simultaneously (Haglund et al., 2012).

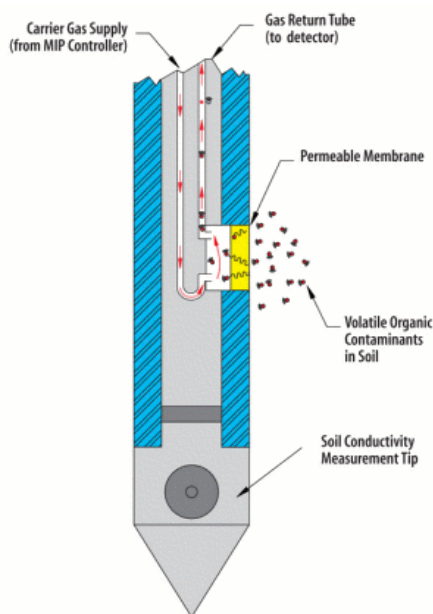


Figure 14. Sketch of MIP-Sounding probe in operation (Geoprobe-Systems®, 2018).

At the Alingsås site, for the sake of detecting chlorinated hydrocarbon-related contaminants, the detectors equipped to the gas chromatograph at the Alingsås site are the photoionization detector (PID), flame ionization detector (FID), and dry electric conductivity detector (DELCD). Each of them has a target group to detect. Specifically, PID detects volatile aromatic hydrocarbons (Yamamoto et al., 2000). FID is sensitive at detecting straight chains of hydrocarbons (Haglund et al., 2012), DELCD is sensitive to chlorinated compounds such as TCE and PCE (Bronders et al., 2009). In addition to these three sensors, the following parameters were also logged continuously: Reducing Speed, Electrical Conductivity, and Temperature.

Overall, there were two sets of integrated MIP-sounding carried out during two different periods. The first set of MIP-sounding was conducted during November 2006, by Ejlskov A/S, with a conventional

MIP probe. Much later, the second set of MIP-sounding was carried out by EnISSA, a Belgium company, on behalf of WSP, in February 2017 (WSP, 2017). This set of MIP-sounding was accomplished by using the MiHPT method which expanded the detection limit of the contaminants to a microgram per litre level (Balzarini, 2017). Even though only the data derived from the second set of MIP-soundings was incorporated into the baseline model due to its time-effectiveness, the first set of MIP-sounding is still presented here to provide a complete description over the Alingsås site.

During the first set of MIP-sounding, in total, 25 MIP-sounding probes were examined (Figure 15). All the MIP-sounding probes were drilled from the ground surface down to the bedrock; thus this sounding measurement also provided some information about the bedrock surface elevation level (Haglund et al., 2012). As can be noted from the result of this set of measurement, most of the contaminants are concentrated in the area in front of the facility building, with a propagation trend towards the northwest direction.

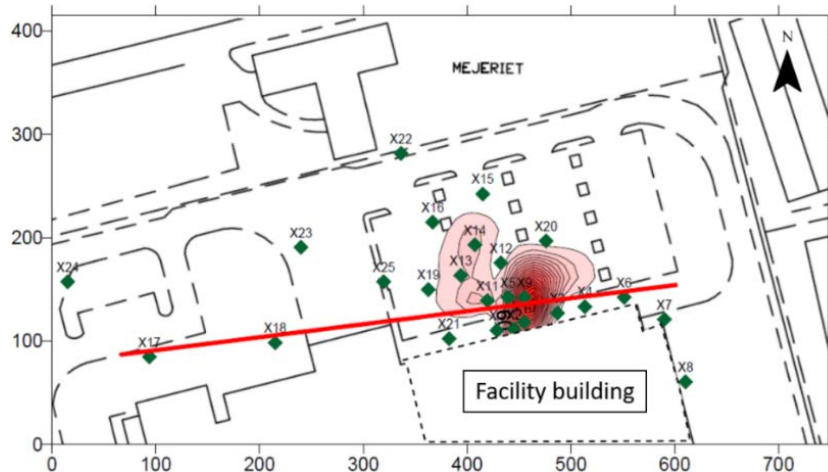


Figure 15. The result of the first set of 25 MIP-Sounding probes at Alingsås site. Interpreted propagation of chlorinated aliphatic was in a northwest direction. The green points represent the first set of MIP-sounding points. The red solid line refers to the wastewater drainage in front of the Alingsås dry cleaning facility building. It is estimated to be 2-2.5 m bgl, but it is not guaranteed. Figure modified from Haglund et al. (2012).

The distribution of the second set of 32 MIP-Sounding points was devised based on the result from the first set of 25 MIP-sounding points and they can be seen in Figure 5. Similar to the first set of MIP-Sounding installations, all the MIP-Sounding probes in the second set measurement were drilled until the bedrock came into being. This was also demonstrated by the rather low permeability value when the bedrock appeared. The analyzed chemicals include PCE, TCE, cDCE, Trans1,2-Dichloroethylene (tDCE), and VC. Apart from PCE itself, the rest of the chemicals are main degradation products with different degradation orders which are illustrated in Figure 16.

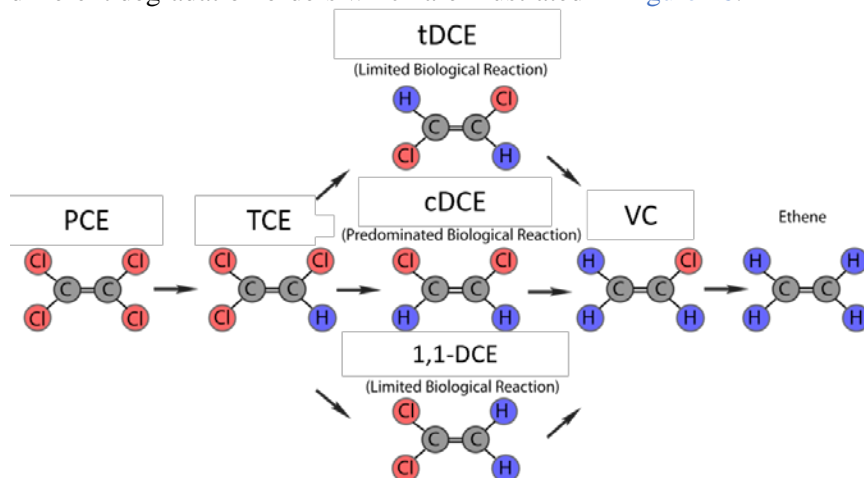


Figure 16. Degradation process from PCE to Ethene. To simplify, TCE is the primary degradation product; tDCE, cDCE, and 1,1 - Dichloroethene (1,1-DCE) are second-order degradation products; VC is third order degradation product. Figure modified from Wiedemeier (1999).

The data provided by EnISSA and WSP was in the form of points with the concentration values attached to them at different elevation level down in the subsurface and the minimum spacing between two adjacent data points is 0.1-meter. To better visualize the distribution of these four contaminants, these data points are displayed as 0.1-meter high cylinders in GeoScene3D.

2.3.2 Multilevel Groundwater Sampling Pipes

In comparison with the MIP-Sounding probes which specialize in detecting chlorinated hydrocarbons in soil, groundwater sampling wells are designed to detect chlorinated hydrocarbons in groundwater. The exploration of the plume's propagation in groundwater can also provide important information about the pollutant status in the zone.

Due to the relatively high density of chlorinated hydrocarbons (DNAPLs) compared with water, the spreading mechanisms of the contaminants not only consist of diffusion (because of the spatial concentration differences) and advection (dominated by groundwater flow rate) but also includes vertical sedimentation due to gravity. Hence, multilevel groundwater sampling pipes were adopted. Moreover, the multilevel groundwater sampling pipes can facilitate characterizing the three-dimensional mapping of the contamination at different levels in the subsurface in comparison with the traditional one level sampling, where the sample is a mixed collection from different levels.

The most recent groundwater sampling was conducted during the period of 2nd-18th October 2017. Overall, 16 samples were taken from 16 different groundwater sampling wells (refer to [Figure 5](#)). The detailed geochemical data of the groundwater samples are unpublished and were kindly provided by Sofia Åkesson, Department of Geology/Lund University, Sweden (S. Åkesson, pers.com., 2018-04-05).

Of all the measured groundwater quality parameters, the concentrations of PCE, TCE, cDCE, and VC were put into the final refined conceptual model. The concentration of different contaminants was provided in accordance with the corresponding sampling screen level of the pipe. Although, the adoption of the multi-level groundwater sampling pipes prevented the sample from being an overall groundwater mixture from the whole sampling pipe at all levels vertically, the adopted 1-1.5 meter screen still yielded the sample of a 1-1.5 meter mixed water column.

By referring to the degradation flowing chart ([Figure 16](#)), the degradation phase of different blocks in the subsurface can also be estimated. The estimation of the degradation state can be conducted via the following ratio (Wiedemeier et al., 1995):

$$\frac{\text{Metabolites}}{\text{Parent Compounds}} = \frac{[cDCE] + [VC]}{[PCE] + [TCE]} \quad (2.3.1)$$

Where the [cDCE], [VC], [PCE], and [TCE] are concentrations in $\mu\text{mol/L}$. A higher ratio value indicates a higher conversion rate from parent compounds (PCE and TCE) to (cDCE and VC).

The ratio is calculated for both groundwater samples and MIP-sounding measurements.

2.4 Geophysical Methods

Geophysical methods, namely DC measurement (also known as Electrical Resistivity Tomography (ERT)) as well as the IP measurement can be promising methods for detecting the contamination or monitoring the remediation process in soils when dealing with DNAPLs (Johansson et al., 2015). Consequently, these two methods are also applied in this project work. This section will start with the theoretical backgrounds of these two geophysical methods, followed by the inversion theories. How the field data was measured and inverted will also be described in this section.

2.4.1 Theoretical backgrounds of DCIP measurements

2.4.1.1 DC measurement

One prerequisite deciding whether the target in the subsurface can be noticed or not when applying the geophysical methods is the contrasts and changes in physical properties of the subsurface. In terms of the electrical resistivity method specifically, the contrasts apply to the electrical resistivity (or conductivity) values, which can further indicate different materials, porosities, water saturation level, etc. Theoretically, such changes can be described through Archie's Law.

$$\frac{\sigma_w}{\sigma_f} = a\phi^{-m} \quad (2.4.1)$$

$$\rho = \frac{1}{\sigma} \quad (2.4.2)$$

Here in Equation (2.4.1), the σ_w and σ_f denote the electrical conductivity [SI Unit: S/m] of water and the formation of the rock respectively. 'a' and 'm' are empirical numbers. Besides, ϕ (ratio value) denotes the effective porosity yielding the possibility for the fluid to flow throughout the subsurface media (Fetter, 2013). Equation (2.4.2) interprets the relationship between conductivity (σ) and resistivity (ρ) [unit: $\Omega \cdot m$]. Overall, Archie's law deciphers that the conductivity of the rock formation is proportional to the conductivity of the fluid in the pores as well as the effective porosity.

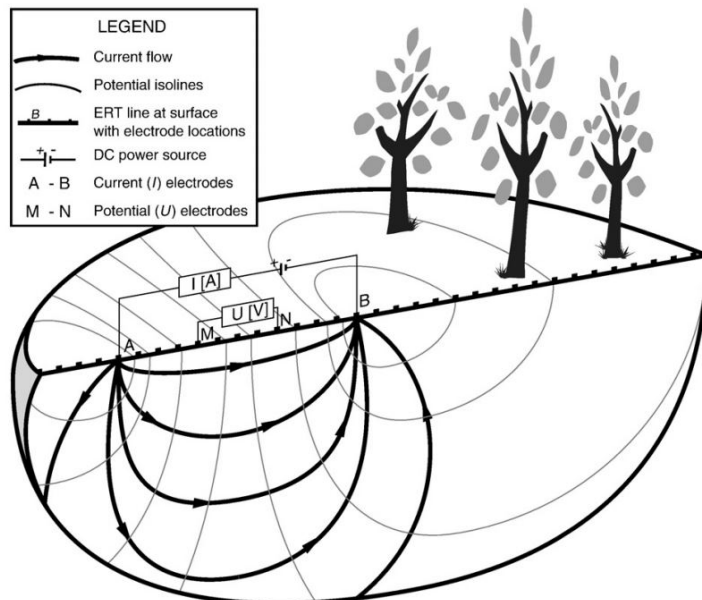


Figure 17. Current flow distribution within a homogeneous media. A and B are current electrodes while M and N are potential electrodes (Alamry et al., 2017).

Figure 17 shows a simplified sketch of the field measurement. As we can see, four electrodes are needed in a single measurement, two current electrodes (A, B) for current injection, and two potential electrodes (M, N) for voltage jump. Consequently, in this set of measurement, the resistance can be calculated based on ohm's law:

$$R = \frac{V}{I} \quad (2.4.3)$$

Where R denotes electrical resistance in ohms (Ω); V denotes the electric potential difference in volts (v); I denotes the electric current in ampere (A).

However, the resistance cannot authentically reflect the intrinsic electrical property of the material since the resistance is also affected by the length and cross-section area of the measured object. To eliminate the geometry effect, the geometric factor k [m] is consequently introduced (Equation 2.4.4).

$$\rho = k * R \quad (2.4.4)$$

Such geometric factor depends on the arrangement of the four electrodes, and the arrangement depicted in Figure 17 is only one of the alternatives, which is called Wenner Alpha array in Figure 18.

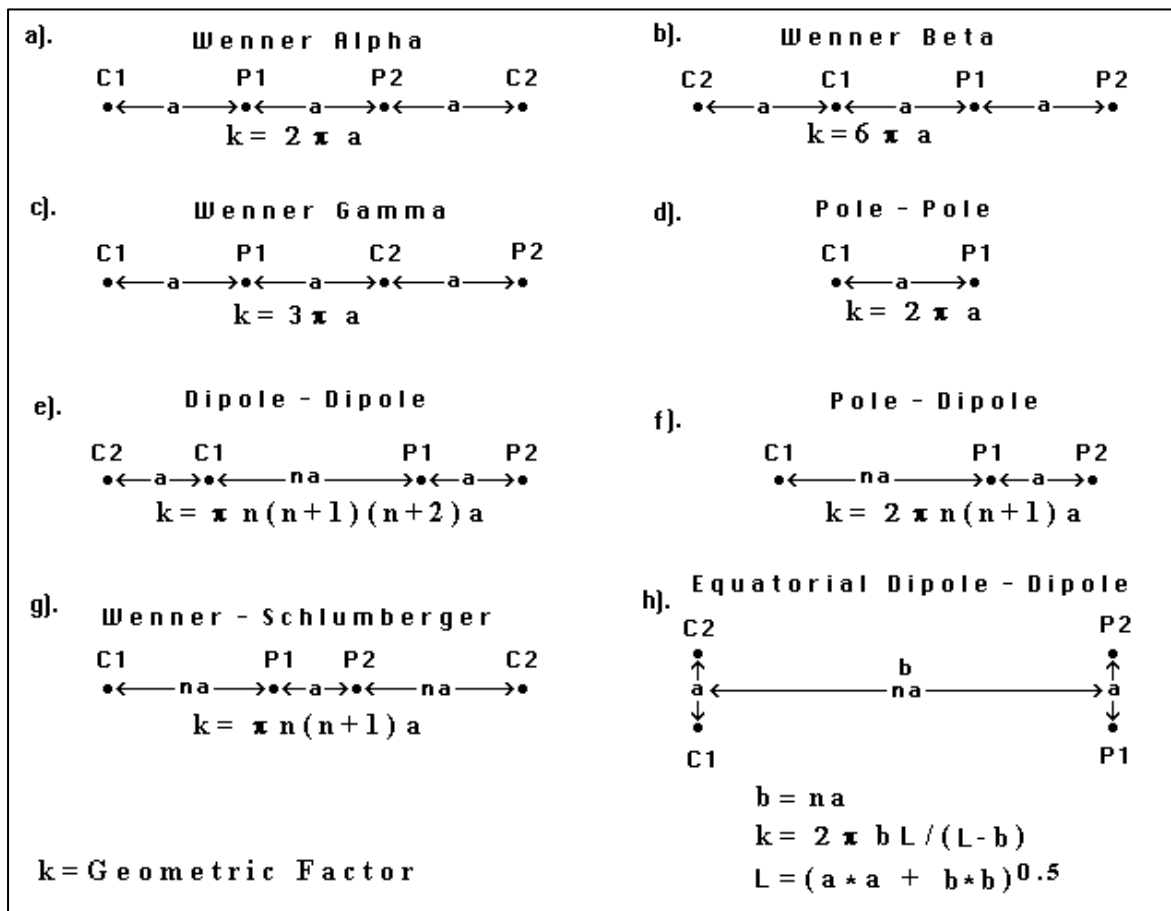


Figure 18. Commonly used arrays in the electrical resistivity measurement. *k* represents the geometric factor. 'a' is the electrode spacing length while 'n' factor is usually the integer value (Loke, 2016).

With the improved Automatic Control System, a relatively new array called Multiple gradient array was developed by Dahlin and Zhou (2006), which was also adopted at this site. By using multi-channel system, potential electrodes pairs at different positions along the horizontal line can conduct the measurements simultaneously with the same positions of current electrodes (Figure 19).

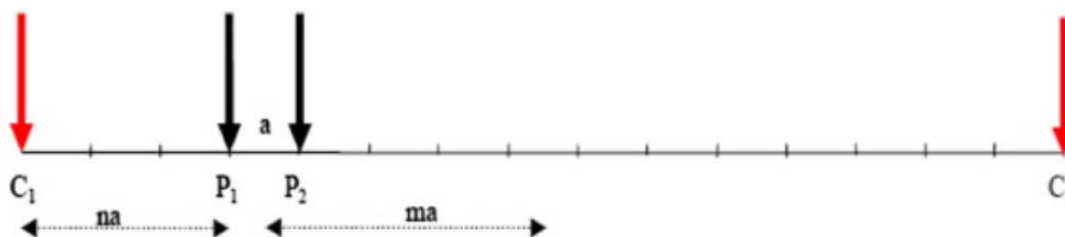


Figure 19. Electrodes configuration for Multiple gradient array. *C*₁ and *C*₂ are the current electrodes. *P*₁ and *P*₂ are the potential electrodes. In the measurement, the current electrodes are kept fixed at the end of the survey line or other specified electrode positions while the potential measuring electrodes are progressively moved within the current electrodes for each data measurement at an interval of the minimum electrode spacing *a* (Aizebeokhai and Oyeyemi, 2014).

This type of array provides the possibility that several measurements can be carried out simultaneously at each current injection point, thus saving time during the field work (Dahlin and Zhou, 2004). Also, in contrast with the regular arrays such as Wenner array and dipole-dipole array, the results derived from the Multiple-gradient array generally show a relatively higher resolution level (Dahlin and Zhou, 2006).

Another thing that need to be noted is that even if the geometric factor is taken into consideration, the measured resistivity here can only be referred to as apparent resistivity which cannot be understood as

the true resistivity value in the subsurface. This is because of the measurement assumption that the earth is a homogeneous media and the behaviour of the current flow is relatively predictable while injected into the ground through the current electrodes (Figure 17).

However, the reality shows up with an inhomogeneous media with different resistivity contrasts (Figure 20) in a three-dimension level. Thus, the ‘Authentic current’ behaviour can no longer be described as a simplified case, instead, the current flow refracts at the layer boundaries, and the measured resistivity will consequently deviate from the ‘true’ value. However, deviation and errors like this can be improved by the data processing and inversions via complex mathematical factors and conversions (Reynolds, 2011). The detailed description can be referred to section 2.4.2.

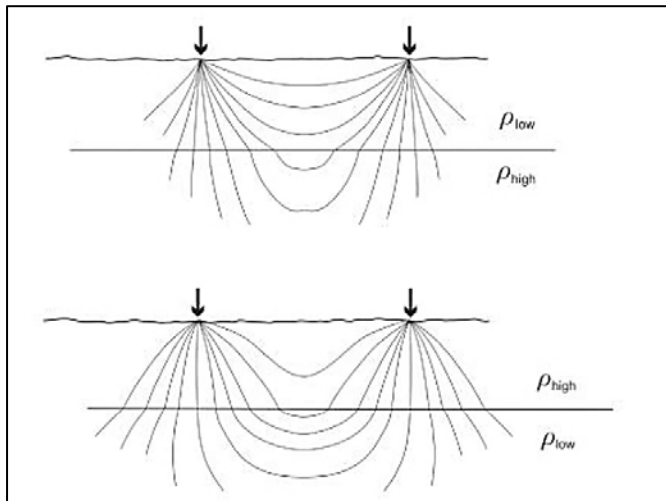


Figure 20. Electrical resistivity contrasts result in the distortion of current flow (Johansson, 2017).

2.4.1.2 IP measurement

In a lot of cases, DC measurement has especially been carried out in the field in order to conclude the possible relationship between the resistivity data response and the DNAPLs contaminant plume. However, the conclusions drawn from those cases resulted in an apparent contradiction. In some cases, the DNAPLs contaminant proved to give a rise to the resistivity values in the subsurface, which can be interpreted by the insulating property of the free-phase contaminant (Atekwana et al., 2000, Chambers et al., 2004, Naudet et al., 2011). In contrast, in some other cases, due to the microbiological degradation process during which organic acid may be produced and the ions are released, it will result in the decrease of the resistivity value in the contaminated zone (Atekwana and Atekwana, 2010).

To cope with the complexity of the situation, more focuses are being put on the IP measurement. Different from the DC measurement which measures the bulk resistivity value, the IP method is more sensitive to small-scale changes such as ions, grain sizes, pore throat sizes (Slater and Lesmes, 2002, Scott and Barker, 2003, Binley et al., 2005). Induced polarization can be measured in time-domain or frequency-domain measurement. Since the field measurement adopted the former one in the Alingsås site, the focus below will be put mainly on time-domain Induced polarization (TDIP) measurement.

IP measurements are usually carried out with DC measurements simultaneously, sharing the same set of electrodes. In comparison with the latter one, the former one put the focus on the undervoltage or overvoltage curve after switching on or off the current injection respectively. Figure 21 exhibits the typical measurement curve from the TDIP measurement. Black solid line denotes the alternating current waveform and the red solid line denotes the potential response to the alternating current injection for a polarisable material. As it is illustrated, after switching on the current injection, it takes a certain time before the potential reaches the maximum value. Correspondingly, after switching off the current injection, it takes a period before the potential drops to zero (Johansson, 2016). However, since the time it takes to drop to zero voltage can be longer in some cases due to several internal and external factors, the measurement of the decaying curve, in the reality, does not wait until it reaches the zero voltage.

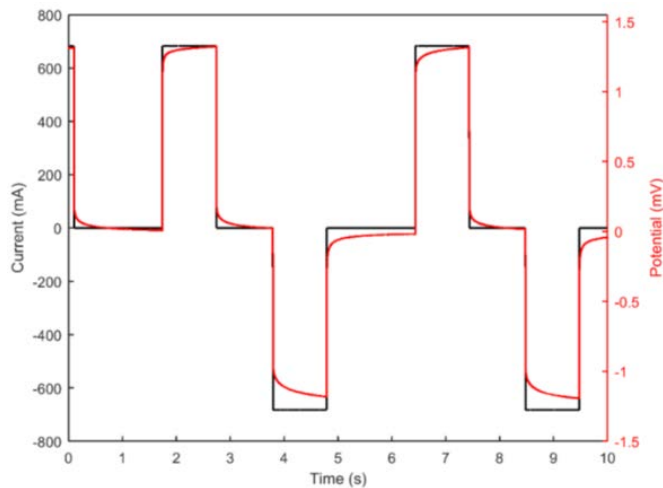


Figure 21. Typical TDIP measurement curve. The black solid line represents the current waveform curve. The red solid curve represents the potential response measured by potential electrodes (Johansson, 2016).

Such IP phenomena can also be put as an analogy to the capacitor due to its dielectric property. While injecting current of high voltage into the ground, the soil acts as a huge electrical capacitor, storing the charges (Kaya and Fang, 1997). As the current injection is switched off, the capacitor will subsequently release the charges stored during the current injection (Knight et al., 1985, Guéguen and Palciauskas, 1994, Glover, 2015).

From a broad point of view, the principal mechanism of the IP phenomenon can be described as a process of deviation and recovery with respect to the equilibrium status, triggered by an added electrical field. Such process can originate from the various ions mobility, the selectivity of the clay, natural charges of the geological particles, etc. Even though no quantified descriptive model has been clarified to date (Dahlin and Leroux, 2012, Reynolds, 2011), the main mechanisms of the Induced polarization phenomenon can be concluded as electrode polarization, electrochemical polarization, and membrane polarization. All of these mechanisms are closely related to the Electrical Double Layer (EDL).

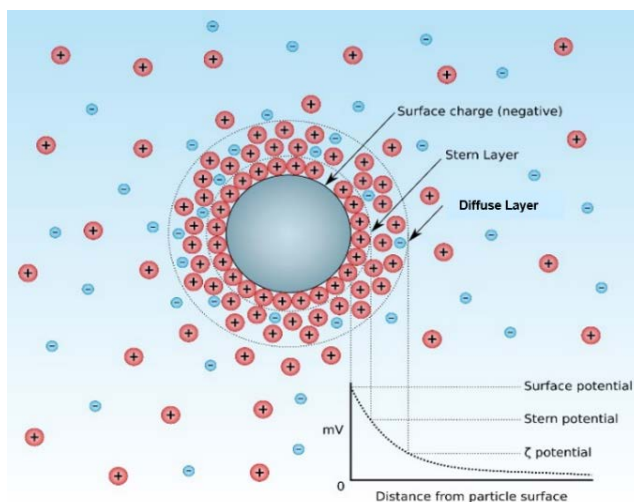


Figure 22. The diagram shows the ionic concentration and potential difference as a function of distance from the charged surface of a particle suspended in a dispersion medium. Figure modified from Mjones (1984).

Figure 22 displays the sketch of an EDL surrounding a negatively charged particle. The naturally charged particles are normally conductive minerals (Sumner, 1976), though semiconductor quartz was also set as an example of EDL in Glover (2015). In general, double-layer structure consists of a stern (or Helmholtz) layer, as well as a diffuse layer. Taking the negatively charged particle in Figure 22 as an example, it attracts a layer of counter ions, namely a layer of cations. This layer of cations tightly surrounds the surface of the negatively charged particle. Consequently, a relatively high potential level can be noticed from the corresponding potential function in Figure 22. This layer is followed by the stern layer which is a layer of mixed cations and anions with the former type of ions of higher

equilibrium concentration level due to the negativity of the central particle. However, such zone of unbalanced charges will be alleviated by a gradient by the distance from the central particle until the charges are balanced at a point in the liquid. The further away from the central particle, the less equilibrium concentration difference between cations and anions (Glover, 2015).

Electrode polarization

The electrode polarization is associated with the conductive minerals in the soil (Sumner, 1976, Ward, 1988). As a conductive mineral particle is disseminated in the soil and surrounded by the electrolyte, the particle's surface will become negative charged. Similar to the description of EDL formation above, surrounding this negatively charged mineral particle forms EDL as well.

As an external electrical field is added, it will subsequently cause the collapse of the steady state, resulting in the inevitable polarization trend. Overall, the electrode polarization is strongly interrelated with two processes that take place at the mineral-electrolyte interface, electrochemical oxidation-reduction reactions and electron transport. Specifically, as the injected currents pass through the conductive mineral, it can generally trigger two procedures. For one thing, a redox reaction takes place on the surface of the central particle, acting as the electrode of the electrochemical reaction. Simultaneously, reaction ions are continuously transported from the electrolyte to the surface of the particle as well. However, the redox reaction rate and the transport rate are usually not equivalent to each other, resulting in two unparalleled processes. If the reaction rate is faster than the transport rate, the ions concentration nearby the electrode is smaller than that in the fluid. Such concentration difference will act as a barrier to the overall reaction, which is namely called concentration polarization. Likewise, if the redox reaction rate is smaller than the transport rate, the former becomes the barrier of the overall reaction and it is namely called the electrochemical reaction polarization. Note that both types of polarization contribute to the deviation of the potential in regard to the equilibrium state.

Johansson (2016) refers the two procedures mentioned above to as the faradic and non-faradic processes. Such faradic charge transfer between the electrode as well as the electrolyte corresponds well with the "leaky capacitor" model brought up by (Wong, 1979). It explains the dielectric characteristic of the system under the alternating currents with high frequency.

Electrochemical polarization

EDLs are not only special to the disseminated conductive minerals, they can also form at the interfaces of the electrically insulating minerals such as silicates (Johansson, 2016). Under the influence of the external electric field, the ions which compose the EDLs are redistributed (Figure 23).

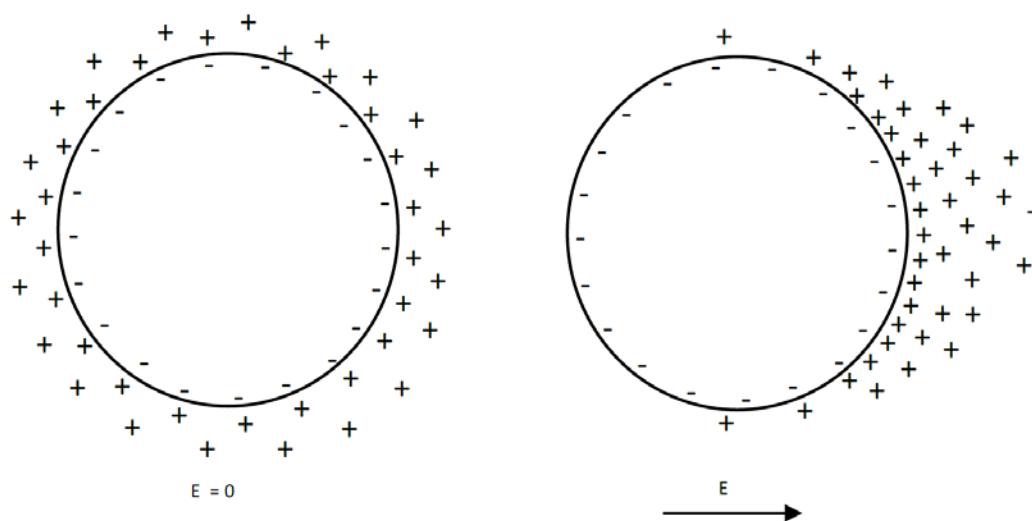


Figure 23. Conceptual sketch of the electrochemical polarization under the influence of the external electric field. The ions that compose the EDLs are redistributed (Johansson, 2016).

There have been extensive discussions about how the stern layer and diffuse layer participate in the electrochemical polarization process. Within these discussions, the recognition of this process has also

been greatly expanded ever since the first time when Schwarz (1962) brought up the theory for the polarization of the stern layer. To date, the recognition of the electrochemical polarization is not only limited to the stern and diffuse layers, but also takes many more factors into consideration, for example the ions mobility, ions densities, and cation exchange capacities (Johansson, 2016). Still, the understanding of the electrochemical polarization awaits to be deepened in association with the Alingsås site since this polarization is potentially one of the main polarization effect contributors, according to the local geological settings.

Membrane polarization

Marshall and Madden (1959) for the first time proposed the membrane polarization model as one of the fundamental mechanisms of the IP phenomenon. Such mechanism is superficially similar to the electrode polarization, which indeed does not involve any chemical reactions (Sumner, 2012). The rooted cause of the membrane polarization is the selective zones existing in the media around the pore zones.

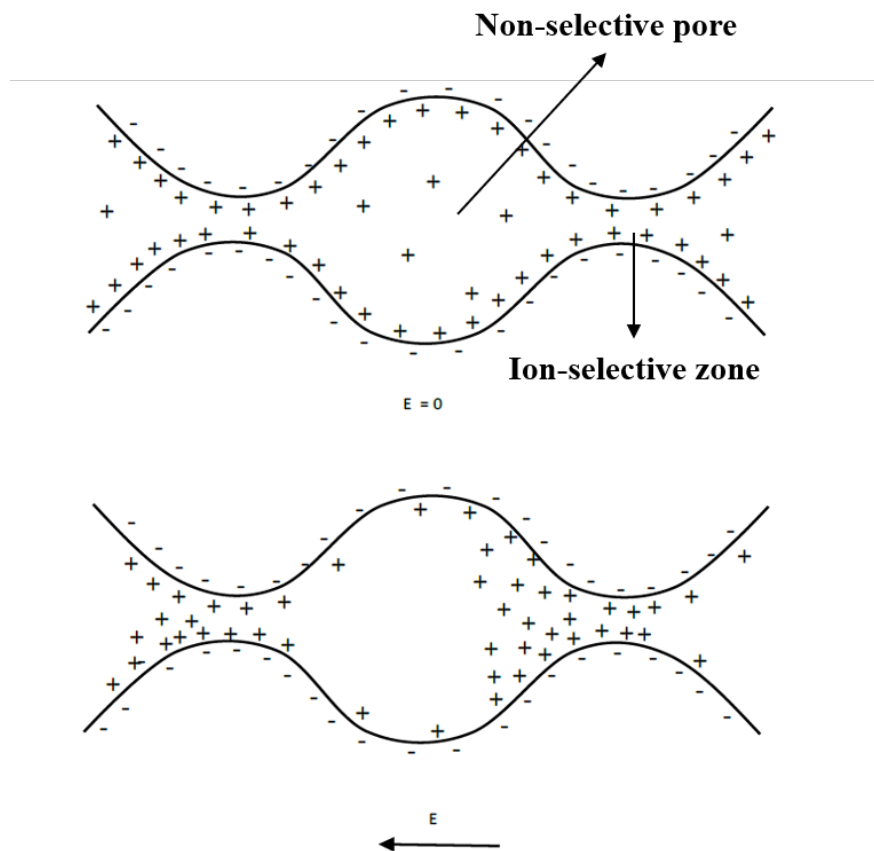


Figure 24. Conceptual sketch of the membrane polarization mechanism. The ion-selective zone existing at the pore throat cause the unbalanced cations and anions distribution to the left and right side of the pore throat while adding the external electrical field. Figure modified from Johansson (2016).

In Figure 24, a wide non-selective pore, as well as a narrow ion-selective zone, exist in a pore system surrounded by clay, for example. The ion-selective zone in clay is characteristically a positive ions selective zone which enhances the cations diffusion while passing through the narrow pore throat (Sumner, 2012). Inversely, the diffusion of the anions is weakened while passing the pore throat. As an external electrical field is added, comparatively more cations pass through the ion-selective zone existing at the pore throat and come to the positively charged side of the pore throat. By contrast, most of the anions are blocked to the negatively charged side of the pore throat due to the selective zone. Consequently, the accumulation of the cations to one side of the pore throat results in the unbalanced potential between both sides, causing the deviation of the voltage.

In time domain measurement, to quantify the effect of the polarization phenomenon, the residual area below the voltage decay curve after switching off the current injection is thus integrated (refer to Figure

25) (Reynolds, 2011, Binley, 2015). The integration result is then divided by the maximum measured voltage value and the outcome is denoted as apparent chargeability (m_i) [unit: $\text{mV}\cdot\text{s}/\text{V}$] brought up by Seigel (1959). The integration equation is displayed as below:

$$m_i = \frac{1}{(t_2 - t_1)} * \int_{t_1}^{t_2} \frac{V(t)}{V_p} dt \quad (2.4.5)$$

Note that here the $(t_2 - t_1)$ [unit: s] indicates an interval to carry out the integration beneath the decay curve. $V(t)$ [unit: mV] indicates the voltage value of the potential curve at the certain time point. V_p [unit: V] denotes the maximum measured voltage value of a potential decay curve.

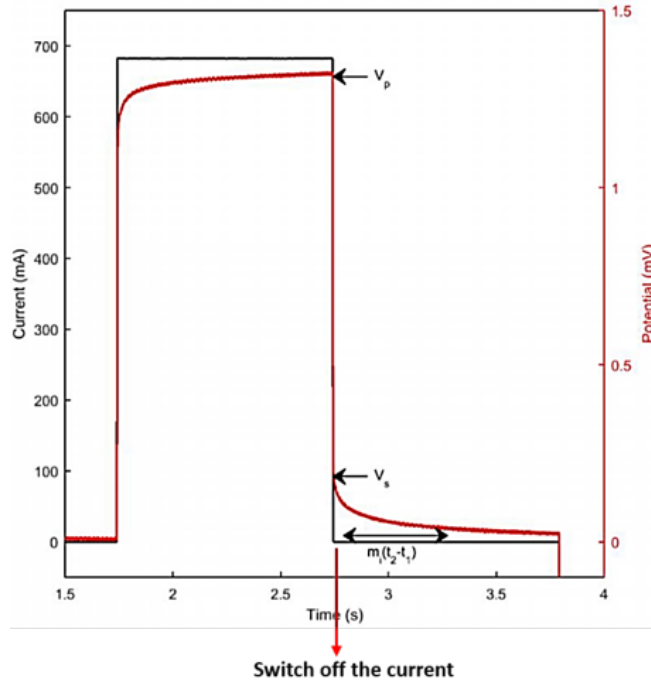


Figure 25. Clarification of time-domain IP measurement decay curve. The black solid line represents the current waveform while the red solid line represents the voltage response curve (Johansson, 2016).

The TDIP measurements are not only carried out with off-time waveform current injection. The 100% duty cycle current waveform is being increasingly adopted in the field measurements.

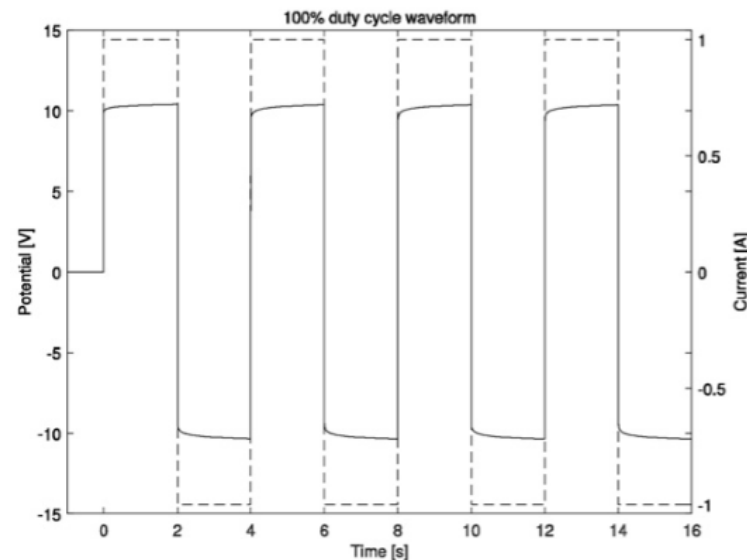


Figure 26. 100% duty cycle current waveform. Solid line represented the measured potential and the dashed-line represents the injected current (Olsson et al., 2015).

Figure 26 displays the 100% duty cycle current waveform. In comparison with IP measurement using the current waveform in Figure 25, the IP measurements carried out with 100% duty cycle waveform

adopts the on-time measurement. The adoption of such waveform can increase the signal-to-noise ratio by up to 100% (Gazoty et al., 2013). The detailed description of this type of waveform can be referred to Olsson et al. (2015).

The derived chargeability (m_i) in many cases does not necessarily reflect the authentic polarization properties. According to the definition brought up by Pelton et al. (1978), the chargeability can be classified as two paths, σ'_{bulk} with an apostrophe represents the real bulk conductivity, and σ'_{surf} with an apostrophe represents the real surface conductivity. The positive correlation between the chargeability and the ratio between the surface conductivity, and the bulk conductivity can be written as Equation (2.4.6) (Slater and Lesmes, 2002).

$$m_i \propto \frac{\sigma'_{surf}}{\sigma'_{surf} + \sigma'_{bulk}} = \frac{1}{1 + \frac{\sigma'_{bulk}}{\sigma'_{surf}}} \quad (2.4.6)$$

As can be implied from the equation above, the directly measured chargeability is strongly dependent on the bulk (fluid) conductivity. If the bulk conductivity is too large, it will possibly mask out the surface polarization effect and such influence has been demonstrated by David P. Lesmes (2001) and Slater and Lesmes (2002). To extract the surface polarization effect solely, the normalized IP parameter was initially brought up by Keller (1959) and referred to as “specific capacity”. The normalization can be achieved by the Equation (2.4.7):

$$MN = \frac{m_i}{\rho} \quad (2.4.7)$$

Where MN represents the normalized chargeability [unit: mS/m], and ρ represents the bulk electrical resistivity [unit: $\Omega \cdot m$].

2.4.2 Theoretical backgrounds of DCIP inversion

A commonly adopted method for two-dimensional DCIP inversion, which is also adopted in this commercial inversion software Res2DInv, is the finite least-squares method (Sasaki, 1989, deGroot-Hedlin and Constable, 1990, Oldenburg and Li, 1994).

Overall, such inversion process can be described as a process of comparison and modification. Here, the parameter for comparison is electrical resistivity. Specifically, in total, at least three subsurface pseudosection are generated to fulfil such comparison-modification process. Firstly, the subsurface area where the measurement was carried out is subdivided into a number of rectangular cells, the apparent resistivity values from the field measurement are assigned to each cell. These cells with apparent resistivity values, as a whole, can be referred to as measured apparent resistivity pseudosection.

The second pseudosection which is a artificial model, represents the “true resistivity” values in the subsurface. Likewise, it is achieved by subdividing the subsurface area into same number of rectangular cells. Subsequently, the resistivity values are also assigned to these cells. In Res2DInv, the first “true resistivity” pseudosection is assigned with the measured apparent resistivity values.

The third pseudosection represents the calculated apparent resistivity based on this original ‘true resistivity’ artificial model. The comparison between the calculated apparent resistivity values (the third pseudosection) and the measured apparent resistivity values (the first pseudosection) is then conducted.

Based on the result of the comparison, the ‘true resistivity’ model (the second pseudosection) is modified until the misfit between the measured and calculated apparent resistivity reaches a reasonable level. The finite ‘true resistivity’ model is called inversed model. Moreover, the misfit is eliminated through the steps of iterations, which can be further explained by the misfit function as below:

$$\Phi_d = \alpha(d - F(m)) \quad (2.4.8)$$

Where the Φ_d denotes the extent of misfit between synthesized ‘true resistivity’ model and measured apparent resistivity values; d represents the measured apparent resistivity data while the $F(m)$ represents the apparent resistivity values calculated from the synthesized ‘true resistivity’ model, and the subtraction indicates the process of comparison between them. Note that the α is the smoothing constraint which highly depends on the specific situation. The adoption of this factor helps to balance between the demand to decrease the misfit value as well as producing a more geologically realistic model (Loke, 2016).

In Res2Dinv, there are two regularized least-squares method to calculate the misfit rate and optimize the inverted model. They are smoothness constrained (or L_2 norm method) (deGroot-Hedlin and Constable, 1990), and blocky (or L_1 norm method) (Ellis and Oldenburg, 1994).

The L_2 norm least-squares optimisation method is given as (deGroot-Hedlin and Constable, 1990, Ellis and Oldenburg, 1994):

$$(J_i^T J_i + \lambda_i W^T W) \Delta r_i = J_i^T g_i - \lambda_i W^T W r_{i-1} \quad (2.4.9)$$

Where J represents the Jacobian matrix of the partial derivatives; λ represents the damping factor; g_i denotes the data misfit vector which is presented the match difference with the logarithms of the measured and calculated apparent resistivity models; Δr_i denotes the model parameter change for the i^{th} measurement, and the r_{i-1} denotes the model parameter vector for the previous step of iteration; W represents the first-order finite difference operator which acts as the roughness filter matrix in the x-, y-, and z- directions. This equation attempts to minimize the squares of data misfits of the model resistivity values, and thus gives greater attention to the larger data misfits while less attention to the minor data misfits (Loke et al., 2003). Such behaviour also makes it more sensitive to bad data points from the measurement (Farquharson and Oldenburg, 1998). This least-squares optimisation method is more appropriate to apply when the subsurface geology shows a smoothing behaviour (Loke, 2016).

In contrast, the L_1 norm least-squares optimisation method is given as (Loke et al., 2003):

$$(J_i^T R_d J_i + \lambda_i W^T R_m W) \Delta r_i = J_i^T R_d g_i - \lambda_i W^T R_m W r_{i-1} \quad (2.4.10)$$

Where R_m and R_d are weighting matrices. They are introduced so that the different parts of the data misfits, as well as model roughness vectors are given same weights during the inversion process. Consequently, with this least-squares optimisation method, the inversion process attempts to minimize the absolute changes in the model resistivity values instead (Loke, 2016). This optimisation method is more applicable to the cases where sharp resistivity boundaries occurs in the subsurface. Accordingly, the least-squares optimisation method chosen for the field data inversion highly depends on the understanding of the local geology settings.

2.4.3 Field measurement settings

The DCIP measurement was carried out with 4 horizontal lines. The location of these four horizontal profiles can be referred to [Figure 5](#). Line 1, Line 2 and Line 3 are parallel to each other with an interval of around 3.6 meters. Different from these three lines, the line 4 starts from the southwest corner of the building, with a slight angle (30°), running through the parking lot. Such arrangements make it convenient for the verification of DCIP measurement with other measurements including borehole logs, groundwater sampling, and MIP-sounding probes. Line 2, especially, crosses through several measurement points.

The measurement was implemented with an ABEM Terrameter LS 2, a fully integrated data acquisition system for resistivity and Induced polarization measurement.

In addition to the ABEM Terrameter LS 2, standard equipment used includes:

- Stainless-steel plate electrodes (10×10 cm)
- Electrode cables
- Electrode jumpers

Since the DCIP measurement was designed to be a constant monitoring, the electrodes should be kept still at the site with the least disturbing factors. These disturbing factors include the factitious and nonarbitrary shift of electrodes. Consequently, to free electrodes away from all those possible interference, profile electrodes were installed 40 cm beneath the ground surface. To attain a better contact between the electrodes and the soil, instead of employing the conventional stick electrodes, the electrodes adopted in this research work were Stainless steel plate-electrodes (Figure 27). The plate-electrodes were assembled on-site to the pigtails outlet cables with stainless bolts and nuts.



Figure 27. The left image displays the stainless-steel plate-electrode used at the Alingsås site. The right image indicates the electrodes were installed in the excavated trench at a depth of 40 cm.

The measurement was conducted with multiple-gradient arrays with 64 electrodes in each array. A sketch of the electrodes layout of the four horizontal DCIP lines is presented in Figure 28. The electrodes layouts of Line 1 to Line 3 are the same. The spacings of two electrodes are 2-meter from electrode 1 to 4 and from electrode 56 to 64 to achieve a greater depth of investigation around the area of interest, while the spacings of remaining electrodes are 1 meter. The electrodes layout of line 4 is slightly different with 1-metre spacings from electrode 1 to electrode 56 and 2-metre spacings for the rest of the electrodes. Consequently, the total length of line 1 to line 3 is 74 meters and the total length of Line 4 is 71 meters. Although, the actual array lengths deviate from them due to the operation errors during the field installations. The global coordinates employed in the inversion process can revise such aberration.

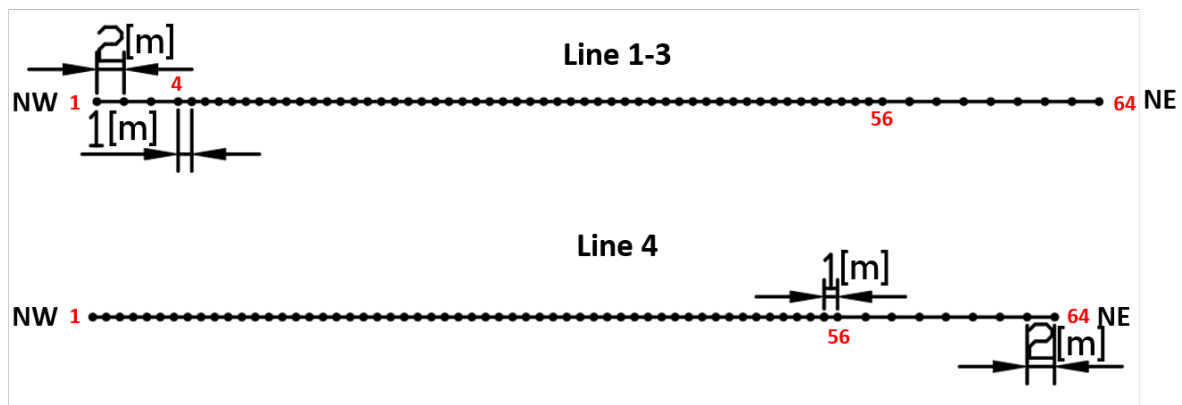


Figure 28. Electrodes layout of the horizontal DCIP lines. Red numbers denote the sequence number of the electrodes.

The background DCIP measurement at the Alingsås site provided, in total, four full sets of measurements 1st November 2017 to 4th November 2017. Each line was measured daily on these four

consecutive days. Theoretically, within such a short period without substantial man-induced interference, the results of the four profiles' DC measurement are supposed to only bear a subtle undulation caused by the random external factors such as soil humidity, temperature, telluric current. Consequently, the data here shown and discussed are from the third day (3rd November 2017) measurement. The detailed field measurement parameters can be referred to [Table 4](#) and [Table 5](#).

Table 4. Together with Table 5 are site DCIP measurement settings.

ID	Array Type	Length [m]	Quadrupoles No.	Injections No.	Measurement Time [min]	Max Channels No.
Line 1	Multiple gradient	74.21	1386	202	82	12
Line 2		74.21				
Line 3		74.03				
Line 4		71.12	1365	198	80	

Table 5. Together with Table 4 are site DCIP measurement settings. Applied current range, as well as the electrodes maximum ground contact are also included. The first-time ground contacts were measured on 6th Nov-2017.

ID	Delay Time [S]	Pulse Time [S]	Time Windows No.	Applied Current [mA]	Max Ground Contact [kohm] (6th Nov-2017)
Line 1	0.01	3.96	12	200.60-201.71	0.88
Line 2				107.83-160.91	0.9
Line 3				54.57-200.65	0.93
Line 4				68.84-200.65	0.94

Ahead of the following inversion steps in Res2Dinv, the first step is to extract the measured data from the Terrameter LS toolbox (data storage software). In this step, the key point is fallen on the IP measurement result especially. For this set of measurement, the first two measurement time windows of all extracted IP curves were deleted due to the irregular ascending trends of curves within these two time windows ([Figure 29](#)). The ascending trends of these two time windows appeared as delayed IP effects which might be due to the response time of the measuring system, or the negative electromagnetic (EM) induction at the point when the injected current alternates.

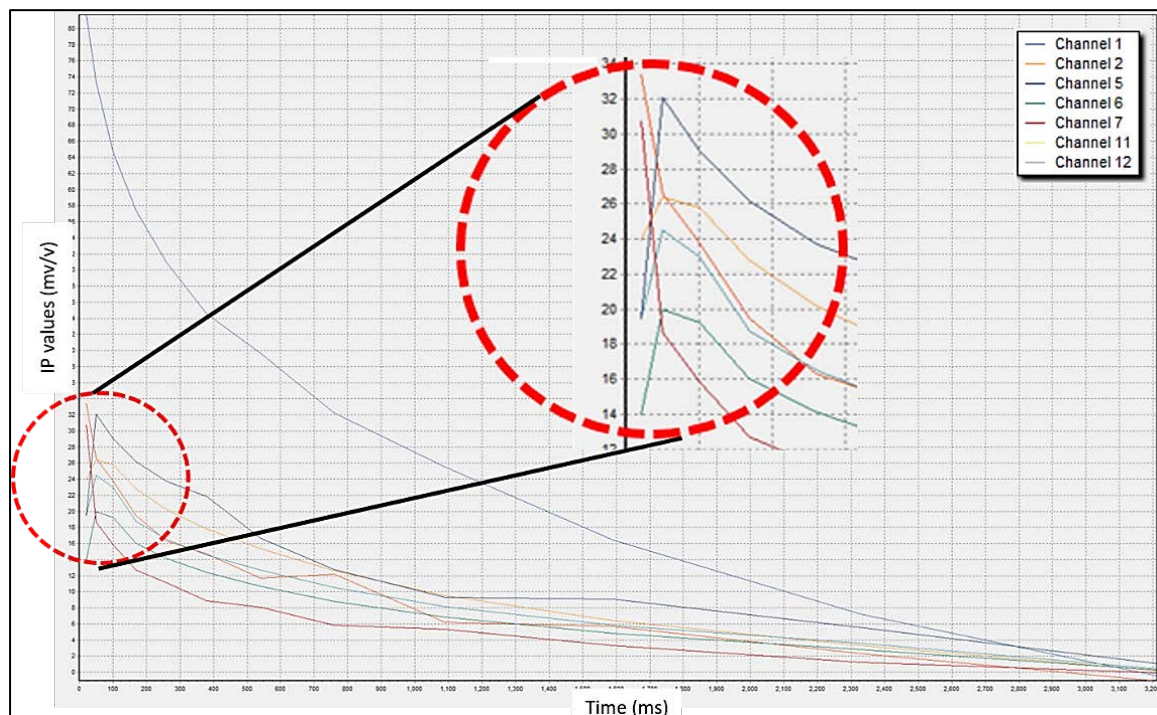


Figure 29. IP decay curves from the original field data. Red dashed line circle. Irregular zone of the curves is circled out with the dashed red line.

Afterwards, the extracted measurement data is put into Res2Dinv in order to pick out the “bad points”. These “bad points” come from various sources of noises, which can be subsequently categorized into two types, ‘systematic noise’ as well as ‘random noise’. The former type of noise is obvious and can be recognised and easily picked out (see Figure 30 and Figure 31). The reasons for the ‘systematic noise’ are various but most commonly it is caused by the poor ground contact which will result in the failure of current injection (Reynolds, 2011). In contrast, the random noise is caused by telluric currents and utilities (Reynolds, 2011).

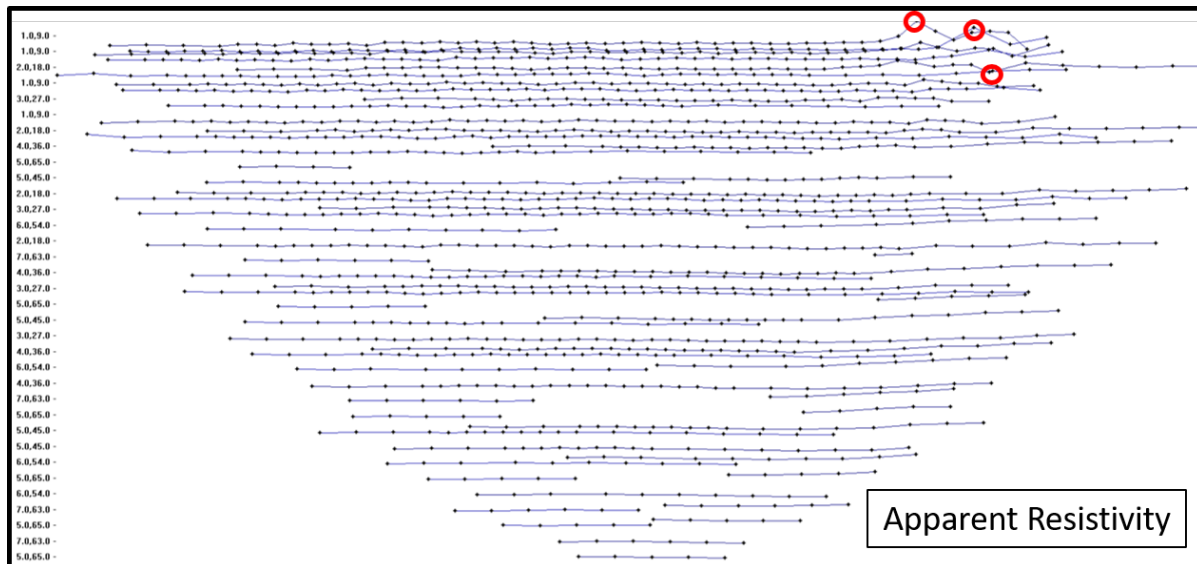


Figure 30. Apparent resistivity data points pseudosection along Line 1 (3rd November 2017), generated via Res2Dinv. Red circles indicate the 'bad points' caused by systematic noises.

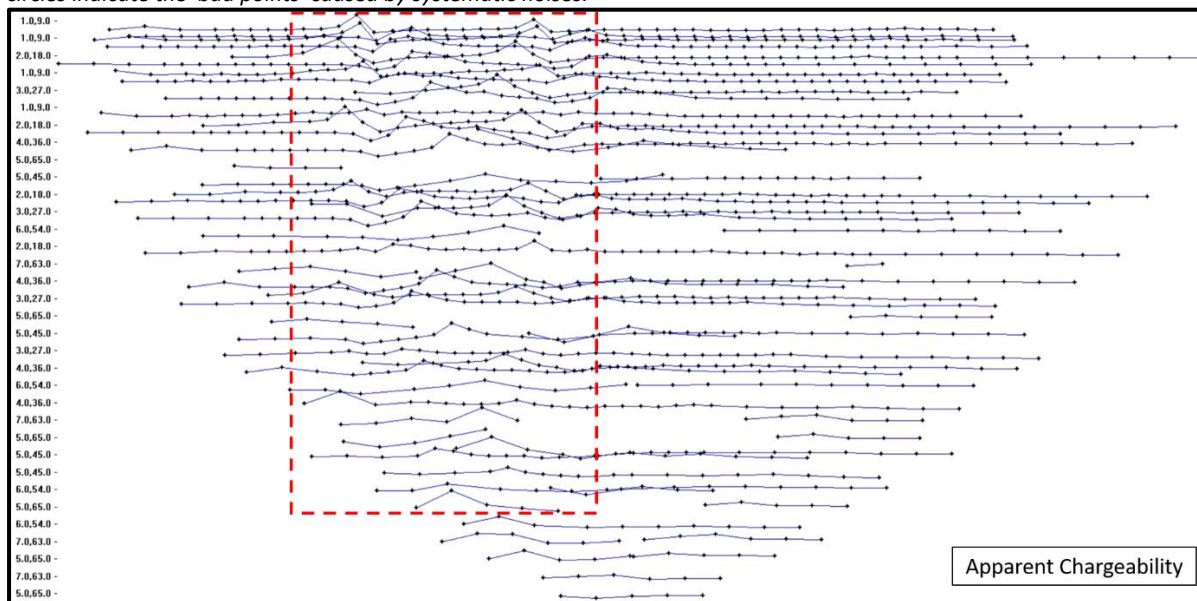


Figure 31. Pseudosection of the apparent chargeability data points along the Line 2 measured on 3rd November 2017, generated in Res2Dinv. Data points within the red dashed-line rectangular box show an extremely high noise.

The further data points cleaning was handled by running a pilot inversion in Res2Dinv. The blue bar charts in Figure 32 displays the distribution of the percentage difference between the calculated apparent resistivity values and the measured apparent resistivity values from the preliminarily inverted model. By moving the green line left and right, the data points within the certain range of data deviation percentage will be trimmed away, which will possibly raise the accuracy of the inversion result. This type of data points cleaning is aimed at eliminating random noise. To guarantee the resolution level of inversion results, misfit rate of 10.0% was selected as the cut-off error for all four DCIP lines.

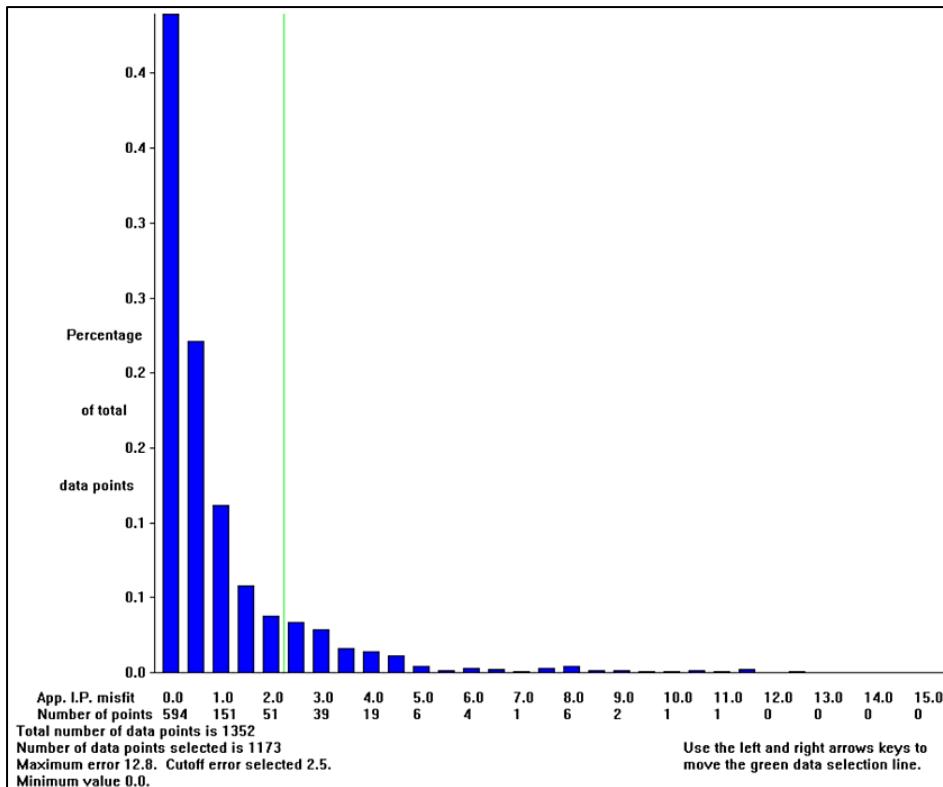


Figure 32. Quantified misfit errors of IP data points along Line 1 after a pilot inversion in Res2Dinv. By moving the green line left and right, data points of great errors can be removed from inversion process

Having been removed noisy points caused by both systematic and random noise, the number of leftover points for one full data set (data points that are contained in one horizontal ERT measurement line) was approximately 1300 data points. Around 20% of the measured points were removed.

Exceptional from the normal horizontal DCIP measurements, the electrodes for this set of measurements were put 0.4 meters beneath the ground surface. The minimum spacing between two electrodes is 1 meter. The roughly estimated minimum investigation depth would be 0.5 meters which is half of the minimum electrodes spacing. Circle with one electrode as a centre point and a radius of 0.5 meters, the soil layer above the electrodes is also included in the investigation range (Figure 33). The resistivity contribution from the topsoil layer above the electrodes cannot be neglected. Since the Res2Dinv does not have a direct option to input the electrodes as subsurface electrodes, borehole formats with a number of dummy electrodes were then employed suggested by Loke (2018). Specifically, the 64 electrodes were treated as 64 borehole electrodes put in 64 boreholes. To modify the depth of layers for the borehole format, the subsurface were synthetically divided into 21 layers with 22 electrodes (21 dummy electrodes and one real electrode). Layers start from 0.2 m bgl to 14.37 m bgl with the ascending intervals from 0.2 meters to 1.5 meters.

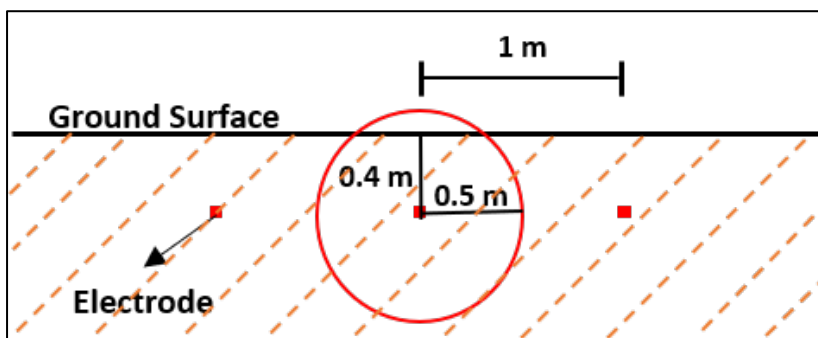


Figure 33. Sketch of subsurface electrodes.

The inversion results of both L_2 norm least-squares optimization (or smoothness-constrained) method and L_1 norm least-squares optimization (blocky) were tested and compared. The inversion results

derived from L1 norm least-squares optimization method tended to yield inverted models with a lower error rate. This is probably due to the relatively high resistivity contrasts existing in the subsurface. Also, from the layers information derived from borehole logs at the Alingsås site, the sand, soil, and bedrock reasonably create large contrasts. Such contrast was even more convinced to the software when the bedrock elevations from the borehole logs at the Alingsås site were input into the data file as the boundary layer information. Under such site condition, the L2 norm least-squares optimization method was adopted and supposed to yield a more accurate and stable inversion result (Dahlin and Zhou, 2004, Loke et al., 2003, Dahlin et al., 2007). Some of the main inversion parameters can be referred to [Table 6](#).

Table 6. Some of the main inversion parameters for all four DCIP lines.

	Line 1	Line 2	Line 3	Line 4
Number of Iterations	7	7	7	7
Used Data Points	1345	1319	1331	1350
Inversion method	L ₁ norm	L ₁ norm	L ₁ norm	L ₁ norm
Incorporate Bedrock Boundary	Yes	Yes	No	No

2.5 GeoScene3D

This research was mainly carried out with software applications in GeoScene3D, a three-dimensional geological modelling software developed by I-GIS (Danish company). This software is outstanding on the visualisation of various field data, which is extremely helpful in correlating different types of data and yielding a more comprehensive understanding of the engineering site.

GeoScene3D supports a variety of data types and have import wizards in place, making it easy to visualize data. Data types used in this thesis work include: geochemistry data points from groundwater sampling pipes and MIP-soundings, groundwater sampling pipes, degradation state estimations for all data points derived from MIP-soundings, DCIP inversion results, electrodes points for DCIP measurements, borehole logs, terrain data, pilot injection wells, inspected ground water levels, estimated storm-water pipes, time-domain reflectometer (TDR) sensors for soil humidity measurement. An overview of the data formats used in GeoScene3D can be referred to [Table 7](#).

Table 7. The formats adopted to input various field measurements data and instruments installations in GeoScene3D, together with related descriptions.

Data Type	Formats and Descriptions
Data points of MIP-soundings	Microsoft® Access.
Data points from groundwater sampling pipes	Microsoft® Access.
Groundwater chemical parameters notes	Microsoft® Access. Save paths of the notes pictures (PNG file) are included.
Degradation state estimations of MIP-soundings	Microsoft® Access.
DCIP inversion results	GeoSoft XYZ. DC, IP, and normalized IP inversion results.
Electrodes points for DCIP measurements	Microsoft® Access.
Borehole logs	Microsoft® Access. Legends file input as CSV file.
Pilot injection wells	Microsoft® Access.
Terrain data	Surfer 3D Grid file.
Storm-water pipes	Eris Shapefile.
Groundwater sampling pipes	Microsoft® Access. Inspected groundwater levels, screens, and casings are included.
TDR sensors	Microsoft® Access.

In addition to the data input, another main function employed in GeoScene3D is interpolation. Two-dimensional interpolation method was adopted to interpolate the bedrock surface as well as the inspected groundwater free table. Three-dimensional interpolation method was adopted to interpolate the geochemical data derived from MIP-soundings.

As a whole, interpolation is a statistical analysis method of constructing new data points within the range of a discrete set of the known data points. The Inverse distance weighed (IDW) interpolation, which is also the only type of interpolation method used in this thesis work, combines the idea of proximity from Thiessen Polygons. The main idea of this method is that the value of an attribute at an unsampled location is inversely proportional to its distance from the estimated value, which also involves the Tobler’s law, phased as “everything is related to everything else, but near things are more related than distant things” (Tobler, 1970). This method has also been compared with other interpolation methods when dealing with the geochemistry data in Lima et al. (2008) and Xie et al. (2011). Both sets of comparisons demonstrated that with this IDW interpolation method, when reasonable interpolation parameters are assigned, can produce a decent interpolation result. Detailed interpolation parameters can be referred to [Table 8](#).

Table 8. Main interpolation parameters adopted in this thesis work.

Interpolation Target	Interpolation Method	search radius (x) [m]	search radius (y) [m]	search radius (z) [m]	Exponent	Smooth
Bedrock surface	2D IDW	500	500	50	25	0
Groundwater free table	2D IDW	500	500	50	7	3
MIP-sounding data points	3D IDW	100	100	0.2	15	3

As can be noticed from [Table 8](#), the setup of the interpolation employed relatively high exponent which targeted on giving more consideration to the original data points. The interpolated points tend to be more affected by the closer point value and the extreme features can be preserved.

For the 3D IDW interpolation of MIP-sounding data points specially, the searching ellipsoid was limited to 0.2 meters which followed the distribution of the original data points. The shortest distance between two data points is 0.1 meters and the 0.2-meter searching ellipsoid limits the range where the points were considered. This avoids the further away points from also being taken into account.

3. Results

3.1 Interpolated Bedrock surface and Groundwater Free Surface

Corresponding to the description of bedrock elevation in section 2.1.2, and the description of the hydrogeological condition in section 2.1.3, the three-dimensional vision of the interpolated bedrock surface, and the groundwater free surface are presented in Figure 34. From top to bottom, terrain surface, interpolated groundwater surface (in green), as well as the interpolated bedrock surface (in orange) are exhibited. On the lower right corner is the zoomed 2D map showing groundwater sampling pipes visualized in three-dimensional vision. Of these, the groundwater sampling pipes with the recorded information of the screen level are marked out with a red-dashed line box.

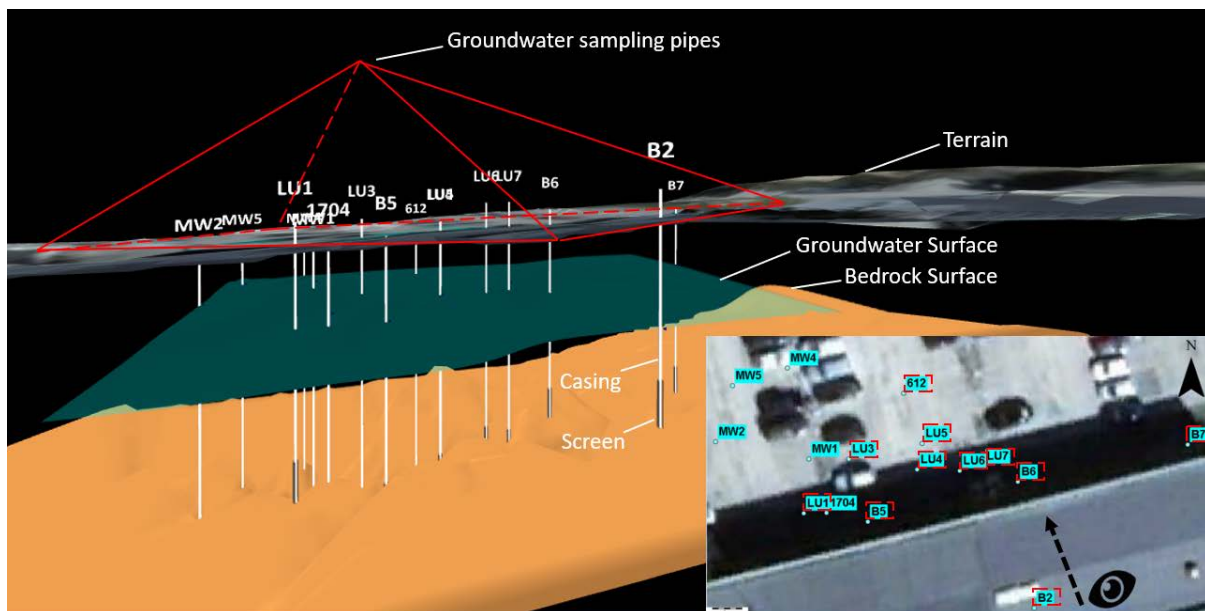


Figure 34. The 3D vision of the surfaces in the final refined geological model via Geoscene3D. Groundwater levels were inspected from the groundwater sampling pipes in the picture. However, only the groundwater sampling pipe labels with a red-dashed box contain screen (filter) information (seen from the map in the lower right corner of this picture). The dashed arrow and the eye icon in the right bottom corner map indicate the 3D vision angle.

In addition to the 3D vision of the interpolated groundwater free surface and bedrock surface, the spatial elevation changes of the bedrock surface, as well as the groundwater level are also displayed in the two-dimensional maps, Figure 35 and Figure 36 respectively.

The spatial variation of the interpolated bedrock surface elevation displayed in Figure 35 shows a relatively regular trend overall. Three yellow dashed lines show the manifest boundary of the bedrock surface elevation change. They are parallel with each other. The shallowest bedrock surface appears at point MIP 7 with around 1.5 meters below the ground surface level while the most profound bedrock elevation appears at the north-west corner of this raster map.

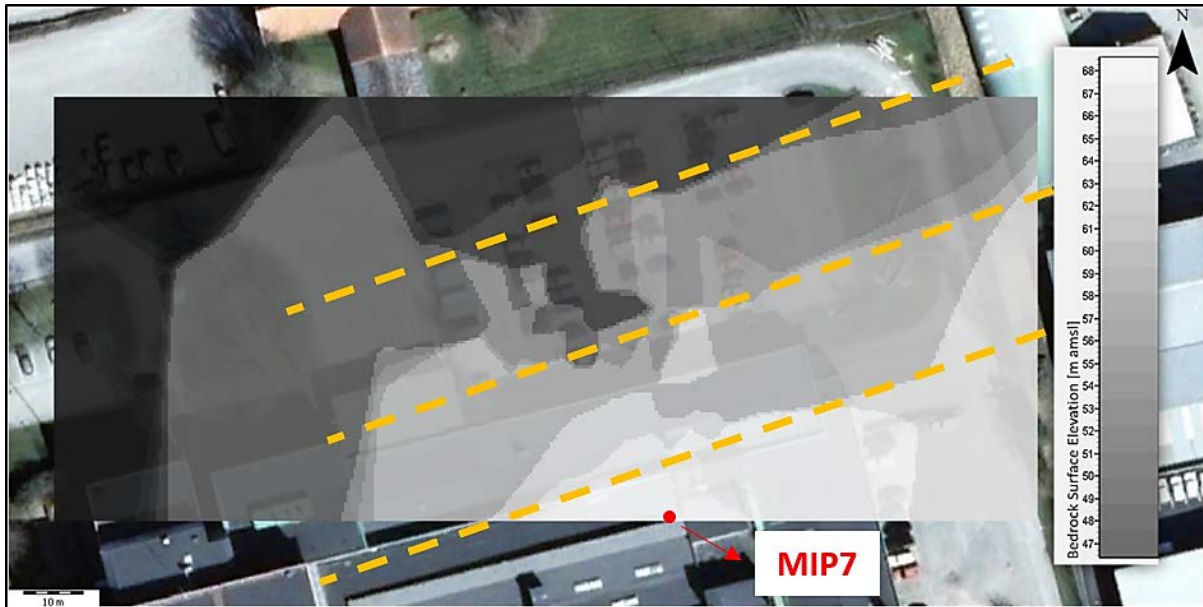


Figure 35. Raster map of the bedrock surface elevation of the Alingsås site. 2D interpolation of the bedrock surface was generated by IDW interpolation method in the GeoScene3D program. A polygon with a colour of lighter grey indicates a closer distance from the bedrock surface to the ground surface. Three paralleled yellow dashed lines show the manifest boundary of the bedrock surface elevation change

The interpolated groundwater free surface in the 2D map can be referred to Figure 36, the zones with B2 and B7 show the highest groundwater free surface level of around 67.2 meters above the mean sea level. In contrast, an evident groundwater drawdown can be noticed between LU1 and 1704 with a depression cone surrounding the LU1 point. This depression zone is suspected due to the clogged borehole. The whole trend of the groundwater free surface level is a bit irregular but still, the groundwater flow direction can be roughly estimated as the red arrow.

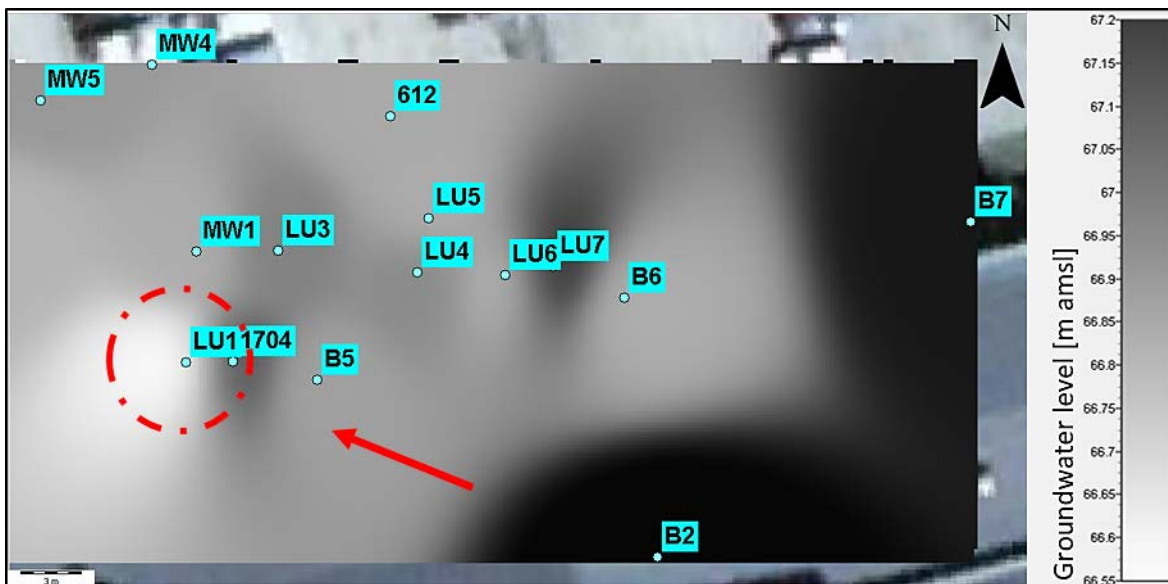


Figure 36. Raster map of the groundwater level of the Alingsås site. 2D Interpolation of the groundwater surface was generated by Inversed Distance Weight (IDW) interpolation method in the GeoScene3D program. Lighter grey indicates lower groundwater level, vice versa. Within the circle of the red-dashed line, an apparent groundwater depression zone can be witnessed.

3.2 Contaminants: three-dimensional distribution

The result of the contaminant distribution in the subsurface is based on two type of measurements, groundwater sampling through groundwater water sampling pipes, and MIP-sounding probes. These two measurements have been introduced in [section 2.3](#) and the detailed location of the measurements can be referred to [Table 4](#). The 3D interpolation was only conducted on the MIP-sounding measurement results, while that of the groundwater sampling pipes are only displayed as original data points in the GeoScene3D model. The exhibition of the contaminants' three-dimensional distribution is performed by cutting slices over the interpolated zone, both vertically and horizontally.

The former type of slices serves four main purposes. The first purpose is to have an overview of the vertical distribution of the contaminants on the southwest-northeast direction. To achieve this, three vertical slices were cut, crossing through two strings of MIP-sounding points (refer to Profile 1,2, and 5 in [Figure 37](#)). The second purpose is to have an overview of the vertical distribution of the contaminants on the Southeast-Northwest direction. This can be concluded from the vertical slice along the “cross-section”. Note that the vertical slices along the “cross-section” can be found in [Appendix C](#) due to the large size of the figures ([Appendix iii](#), [Appendix iv](#), and [Appendix v](#)). The third purpose is to verify the groundwater chemical analysis data with the MIP-sounding measurement. Two example slices along profile 3 and profile 4 are cut as representatives for the parking lot and inner-facility regions respectively. The fourth purpose is to verify the DCIP results with the contaminants vertical distribution along the four DCIP lines. The cross-sections of these four lines are put in [section 3.4](#).

The horizontal slices target on revealing the contaminants spatial distribution at different elevation levels (69.52 m amsl, 68.71 m amsl, 67.01 m amsl, 63.5 m amsl, and 60.27 m amsl).



Figure 37. The location of all the drawn profiles and cross-section for vertical slices. Small up-triangles represent all the MIP-sounding points. Small red squares represent all the groundwater chemistry data points. Profile 1, Profile 2, and Profile 5 are used for visualising contaminants vertical distribution on the southwest-northeast direction. Profile 3 and Profile 4 are used for the verification between groundwater chemistry data and MIP-sounding data. The cross-section is used for visualising contaminants vertical distribution on the Southeast-Northwest direction. The red solid-line box represents the estimated zone where the initial PCE leakage took place.

Measurement error is suspected for this anomalous zone. The black dashed lines are suspected to be the clay boundary. For TCE specifically, the dashed-line box ③ represents the zone with the highest TCE concentration in this slice cut. The dashed-line box ④ marks out a leftward horizontal extension trend of the high concentration TCE plume.

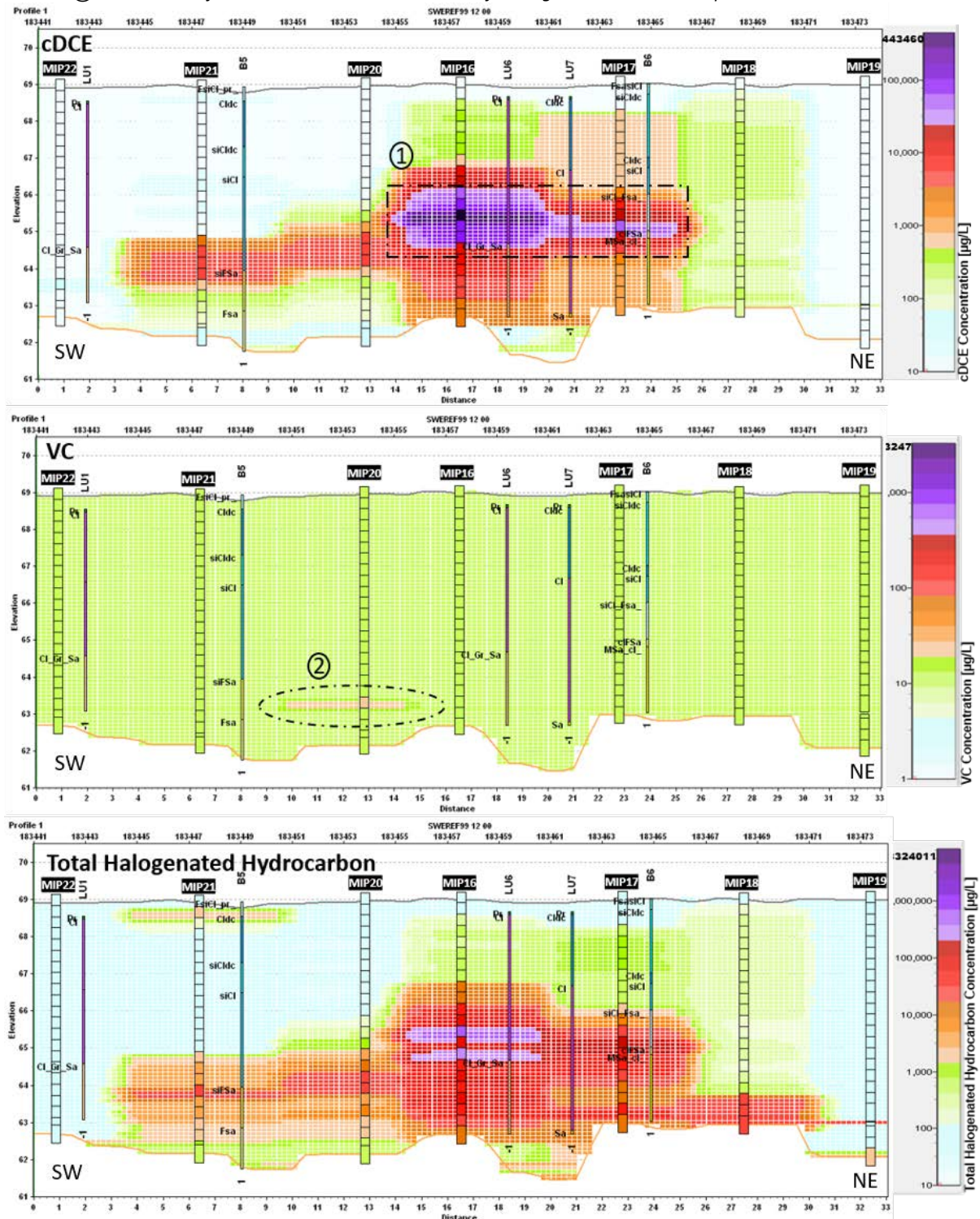


Figure 39. Together with Figure 38 are vertical slices along the profile 1 by contaminants. The dashed-line box ① marks out the highest cDCE concentration zone in the slice cut, which is slightly higher than that of TCE. The dashed-line box ② marks out the anomalous high VC concentration zone.

Profile 1 goes through seven MIP-sounding probes with five boreholes within the 1.5-meter buffer range. The concentrated data points, as well as the adjacently logged lithological information, make profile 1 an outstanding profile to be attended in the discussion section.

The concentration distribution trends of different contaminants can be clearly seen from the vertical slices. Of them, the contaminants such as PCE, TCE, and cDCE have relatively similar distribution behaviour, with the highest concentration occupying the zone in between MIP-sounding probe 20 and MIP-sounding probe 18. However, the elevation levels of these zones are not quite the same. Instead, from PCE to cDCE, they show a raising trend. For example, that zone of PCE (dashed-line box ② in Figure 38) is the closest to the bedrock surface. In comparison, that zone of TCE (dashed-line box ③ in Figure 38) is about 0.7 meters, with a horizontal leftward extension trend. The most concentrated zone of cDCE (dashed-line box ① in Figure 39) has the highest position in comparison with the other two, with more than 1-meter distance from the bedrock surface.

Different from the contaminants mentioned above, the concentration distribution of VC has a more constant behavior with around 10 µg/L in most of the area. However, an apparent higher concentration zone (dashed-line box ② in Figure 39) can be noticed surrounding MIP-sounding probe 20, at about 6 meters depth from the ground surface. The concentration of this anomalous zone is 24.62 µg/L. Another anomalous zone (dashed-line box ① in Figure 38) can also be identified from the profile section for PCE, which appears at the shallow part of MIP-sounding probe 21. Such anomalous higher concentration is suspected as measurement error.

The MIP-sounding data points themselves, in some cases, have very sharp changes by a factor of 10 between nearby data points within 10 cm. Such sharp concentration contrast might be caused by the occurrence of the impervious layer. The overall distribution feature of the total halogenated hydrocarbon is nearly the same as that of PCE due to the dominant concentration level of PCE.

3.2.1.2 Vertical slices along profile 2

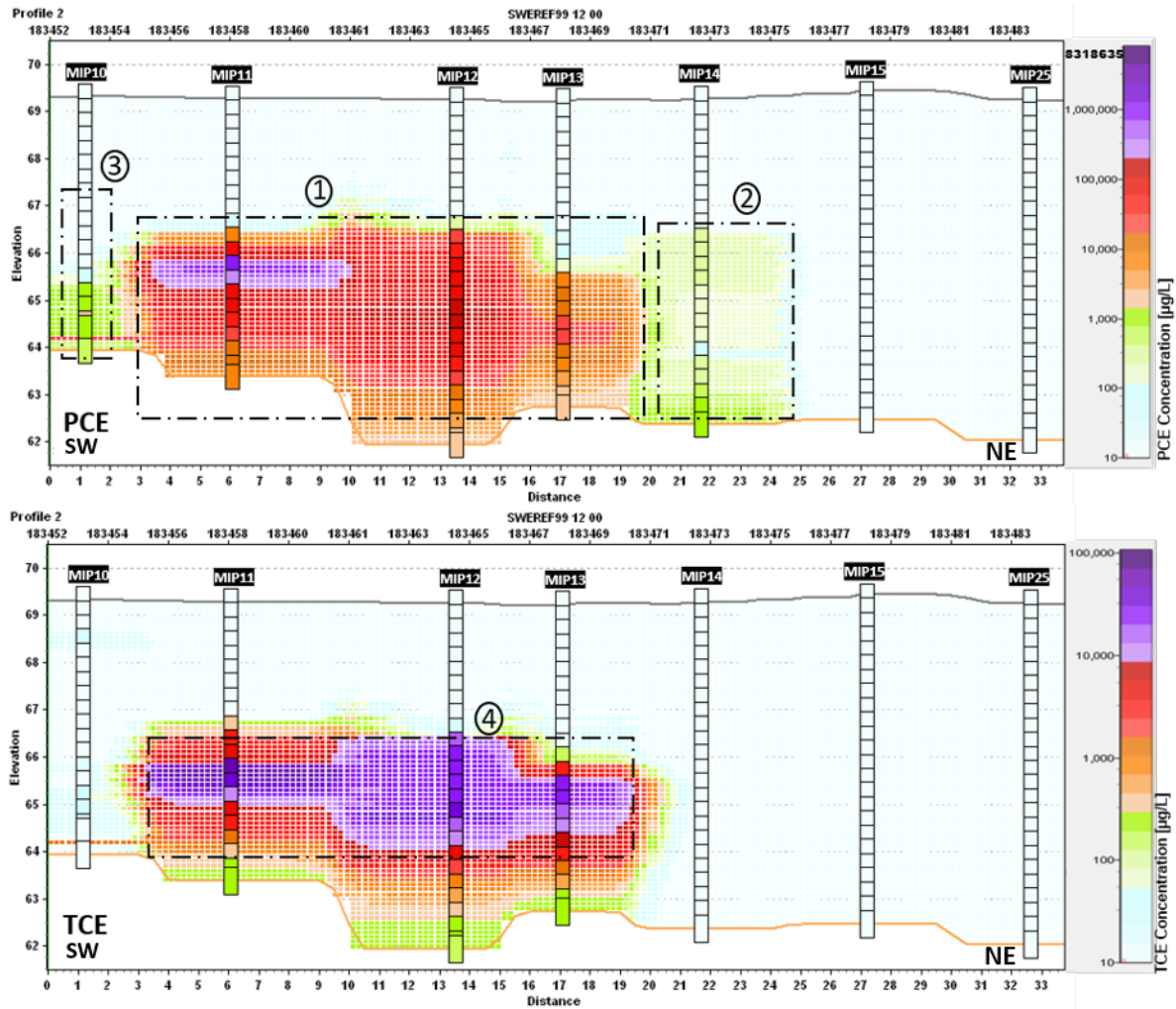


Figure 40. Together with Figure 41. For PCE specifically, the dashed-line box ① marks out the most concentrated zone of PCE. The dashed-line boxes ② and ③ mark out the apparent transition zones connecting the high concentration and low concentration zones. For TCE specifically, the dashed-line box ④ marks out the highest concentration zone.

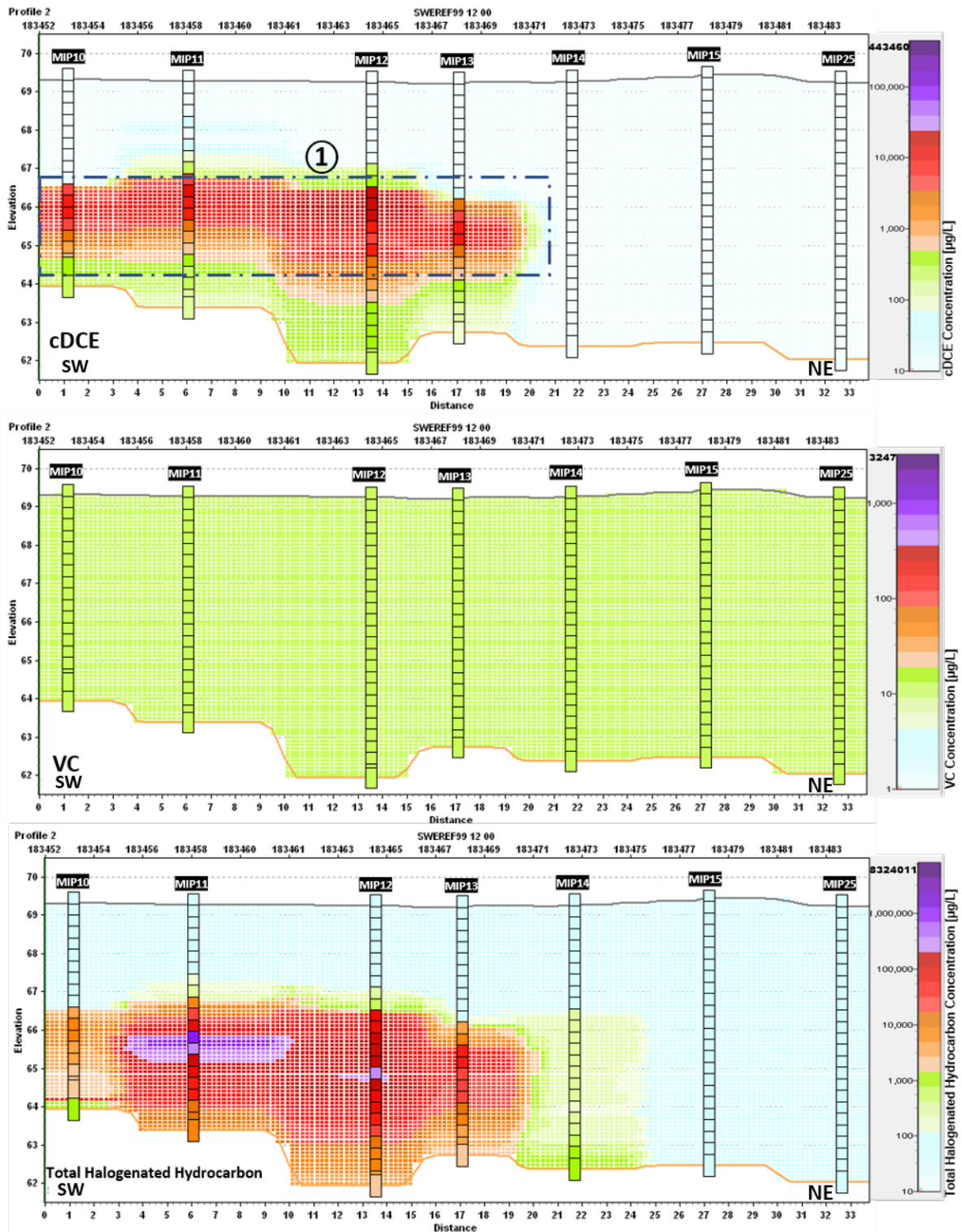


Figure 41. Together with Figure 40 display the vertical slices along the profile 2 by contaminants. Dashed-line box ① marks out the high concentration zone of cDCE.

Along the slices cut along the profile 2, the obvious high concentration zones can be found for PCE, TCE, and cDCE while the concentration of VC remains constant with around 10 µg/L.

For PCE specifically, the apparent concentration transition zones can be noticed surrounding both MIP10, and MIP-14. Since no high PCE concentration was detected on MIP15, it can be assumed that the PCE plume flow stopped between MIP14 and MIP15. In comparison, due to the relatively high PCE concentration being detected on MIP 10, it remains unknown at which position the PCE plume flow boundary occurs to the left of the MIP10.

It can also be noticed that on the bottom of the TCE plume and cDCE plume exist zones of lower concentration level, contacting the bedrock surface. However, it cannot be determined whether the high concentration zone will expand to this elevation level in the coming future.

3.2.1.3 Vertical slice along profile 3

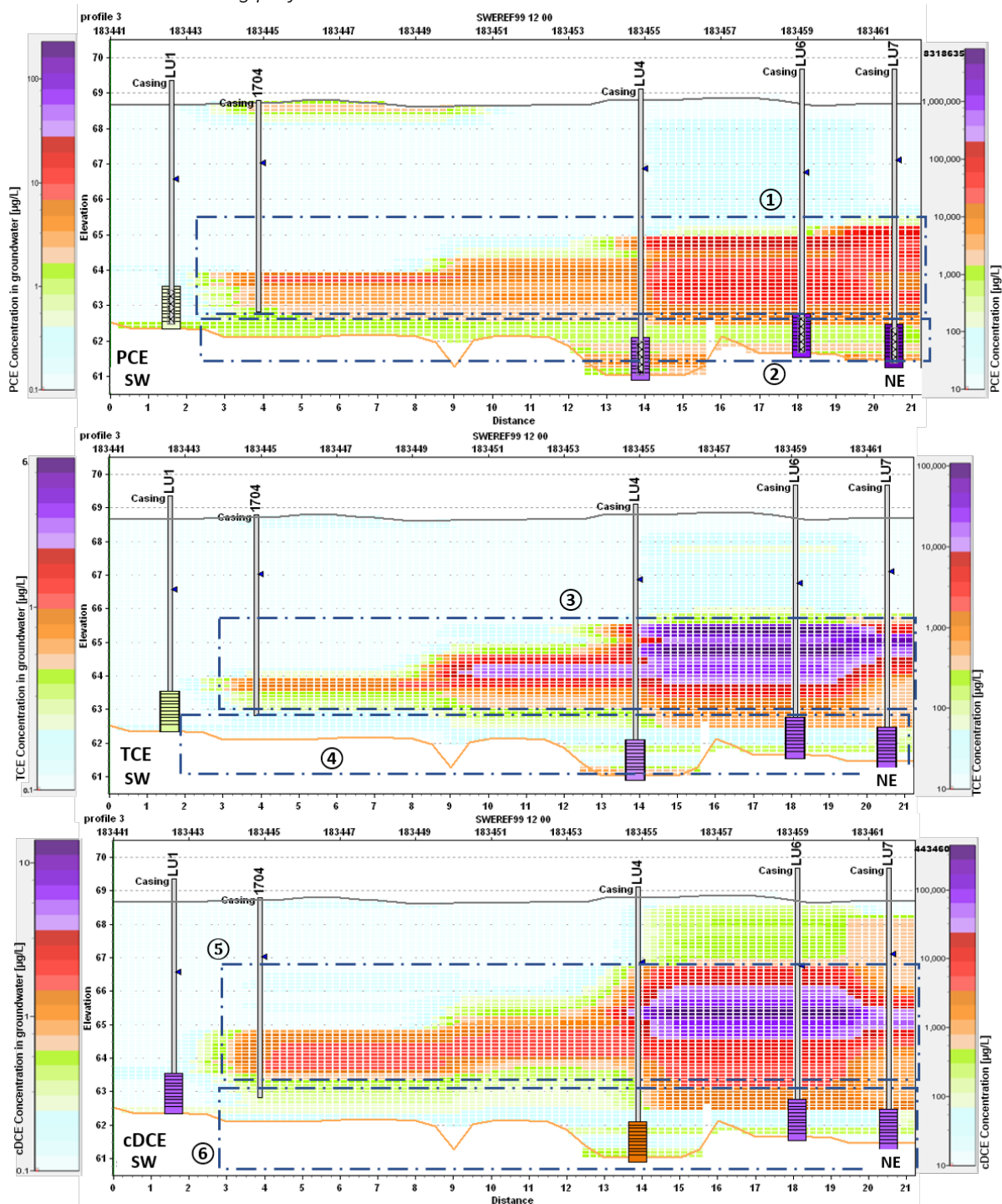


Figure 42. Together with Figure 43 are vertical slices along the profile 3 by contaminants visualising the interpolation result based on the MIP-sounding measurements. To the left side of the cross-sections are legends for contaminants concentration in groundwater (S. Åkesson, pers.com., 2018-04-05). To the right side of the cross-sections are legends for contaminants concentration derived from MIP-sounding probes. The dashed-line box ①, ③ and ⑤ mark out the main contamination zone along this slice cut for PCE and TCE and cDCE respectively, and the dashed-line boxes ②, ④ and ⑥ mark out the lower concentration zone, adjacent to the bedrock surface. The concentration values of contaminants in groundwater are much lower than those measured through MIP-sounding probes.

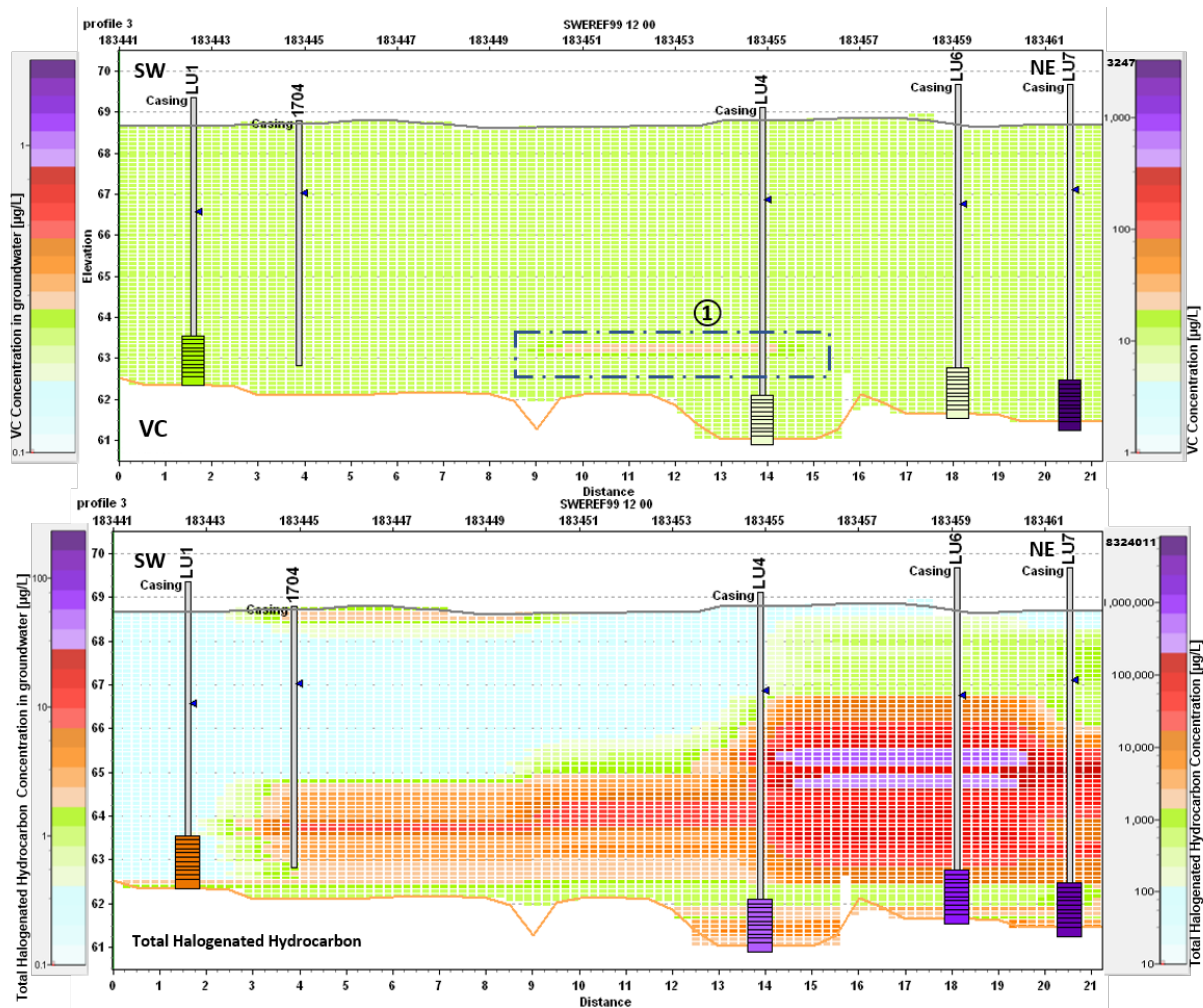


Figure 43. Together with Figure 42 are vertical slices along the profile 3 by contaminants. To the left side of the cross-sections are legends for contaminants concentration in groundwater (S. Åkesson, pers.com., 2018-04-05). To the right side of the cross-sections are legends for contaminants concentration derived from MIP-sounding probes. For VC specifically, the dashed-line box ① marks out an anomalous zone with slightly higher concentration.

Slices cut along the profile 3 involve both the groundwater chemistry data as well as the interpolation of MIP-sounding measurements. One apparent difference between these two measurements is that the concentration of each contaminant measured through the MIP-sounding probes is much higher than that derived from the groundwater sampling data. The overall MIP concentration trend of these four groundwater sampling wells (LU1, LU4, LU6, and LU7) correspond well with the MIP-sounding results. However, some exceptions can still be witnessed. For example, in the slice of cDCE distribution, the cDCE concentration in the groundwater sample from LU1 is higher than that from LU4. In the slice of VC distribution, the VC concentration in groundwater samples from LU1 and LU7 are higher than those from LU4 and LU6.

Inspecting the interpolated MIP-sounding data solely, the distribution behaviours of PCE, TCE, and cDCE are alike in some ways. For example, the main contamination zones of PCE, TCE, and cDCE have almost the same positions (see dashed-line boxes ①, ③ and ⑤ in Figure 42). Likewise, the dashed-line boxes ②, ④ and ⑥ in Figure 42 mark out the lower concentration zones of each contaminant, adjacent to the bedrock surface. The overall concentration distribution of VC still shows a constantly low concentration level almost everywhere.

3.2.1.4 Vertical slices along profile 4

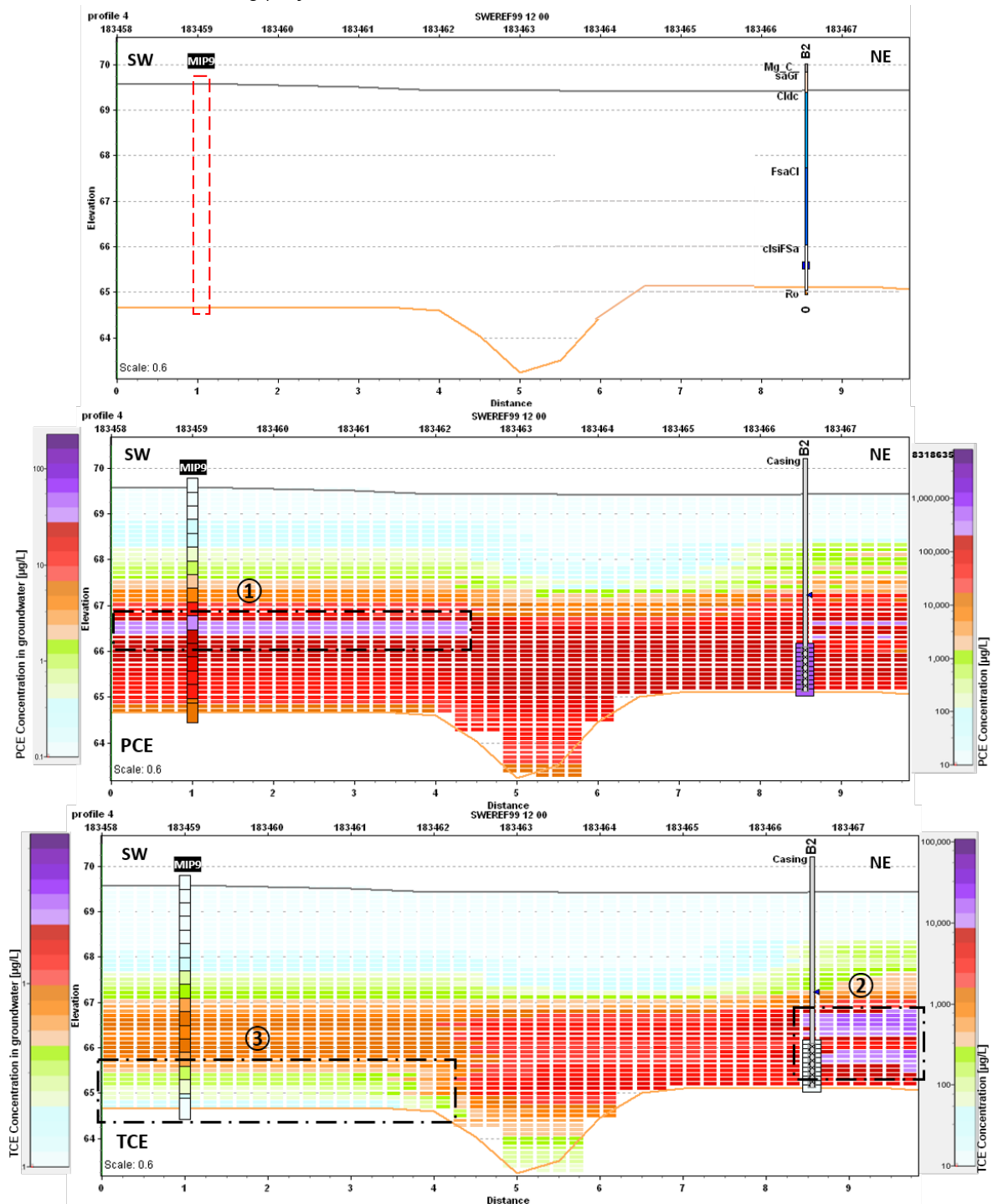


Figure 44. Together with the Figure 45 are vertical slices along the profile 4 by contaminants. To the left side of the cross-sections are legends for contaminants concentration in groundwater (S. Åkesson, pers.com., 2018-04-05). To the right side of the cross-sections are legends for contaminants concentration derived from MIP-sounding probes. The dashed-line boxes ① and ② mark out the highest concentration zones for PCE and TCE respectively. The dashed-line box ③ marks out the lower TCE concentration zone, adjacent to the bedrock surface.

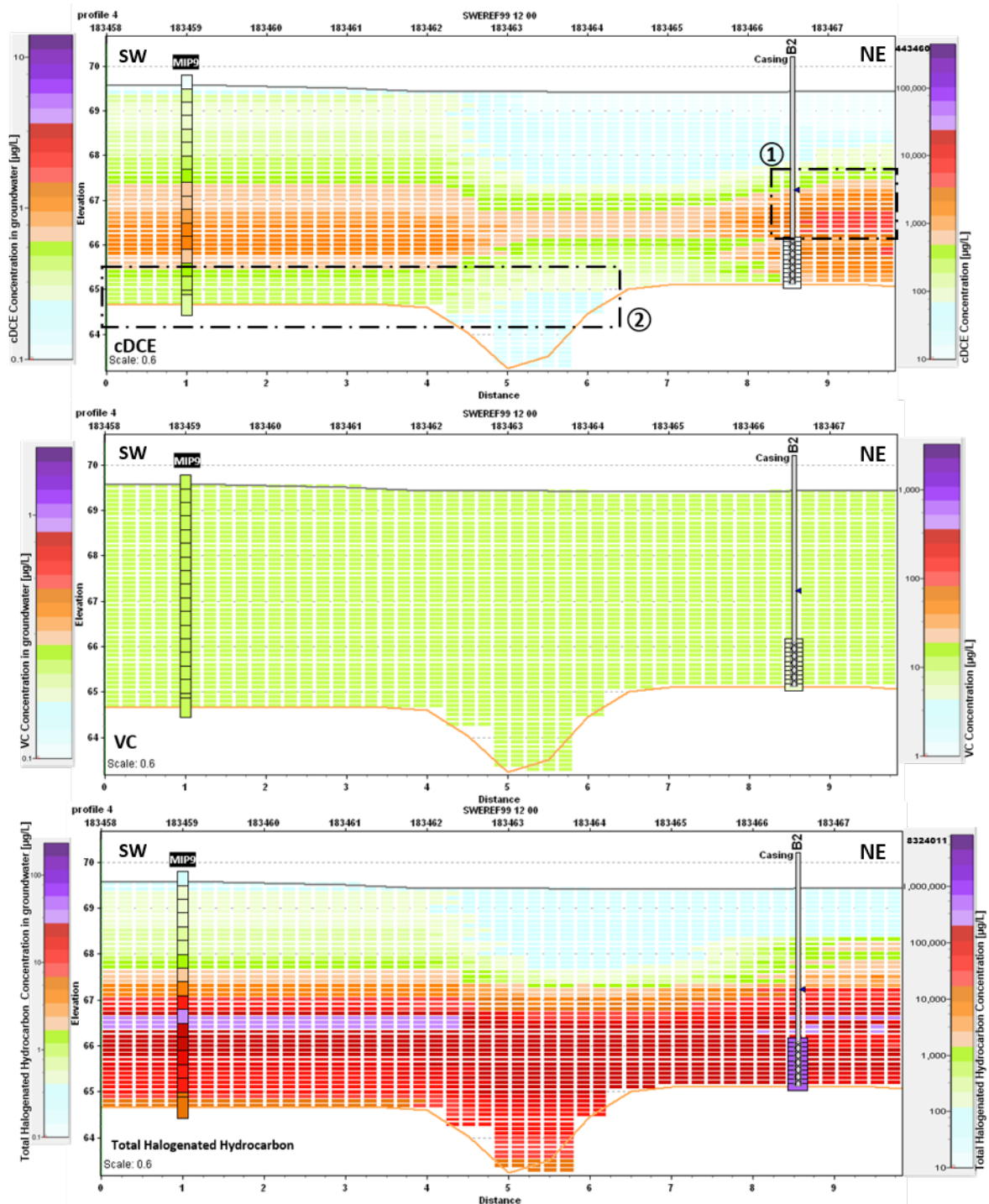


Figure 45. Together with Figure 44 are vertical slices along the profile 4. To the left side of the cross-sections are legends for contaminants concentration in groundwater (S. Åkesson, pers.com., 2018-04-05). To the right side of the cross-sections are legends for contaminants concentration derived from MIP-sounding probes. The dashed-line box ① marks out the highest concentration zone of cDCE while the dashed-line box ② marks out the lower concentration zone adjacent to the bedrock surface.

Similar to the slices along the profile 3, the slices along the profile 4 consists of both groundwater sampling data and MIP-sounding data, plus one borehole log B2 while the groundwater sampling pipe was installed. The concentration distribution of PCE is slightly different from TCE and cDCE, with the highest concentration zone located around the MIP-sounding probe 9 (see dashed-line box ① in Figure 44). In comparison, the highest concentration zones of TCE and cDCE both appear on the North-East side of B2 groundwater sampling pipe (see dashed-line box ② in Figure 44 and ① in Figure 45). Also,

in cross-sections of both TCE and cDCE, lower concentration zones adjacent to the bedrock surface can be identified (see dashed-line box ③ in Figure 44 and ② in Figure 45 respectively).

3.2.1.5 Vertical slices along profile 5

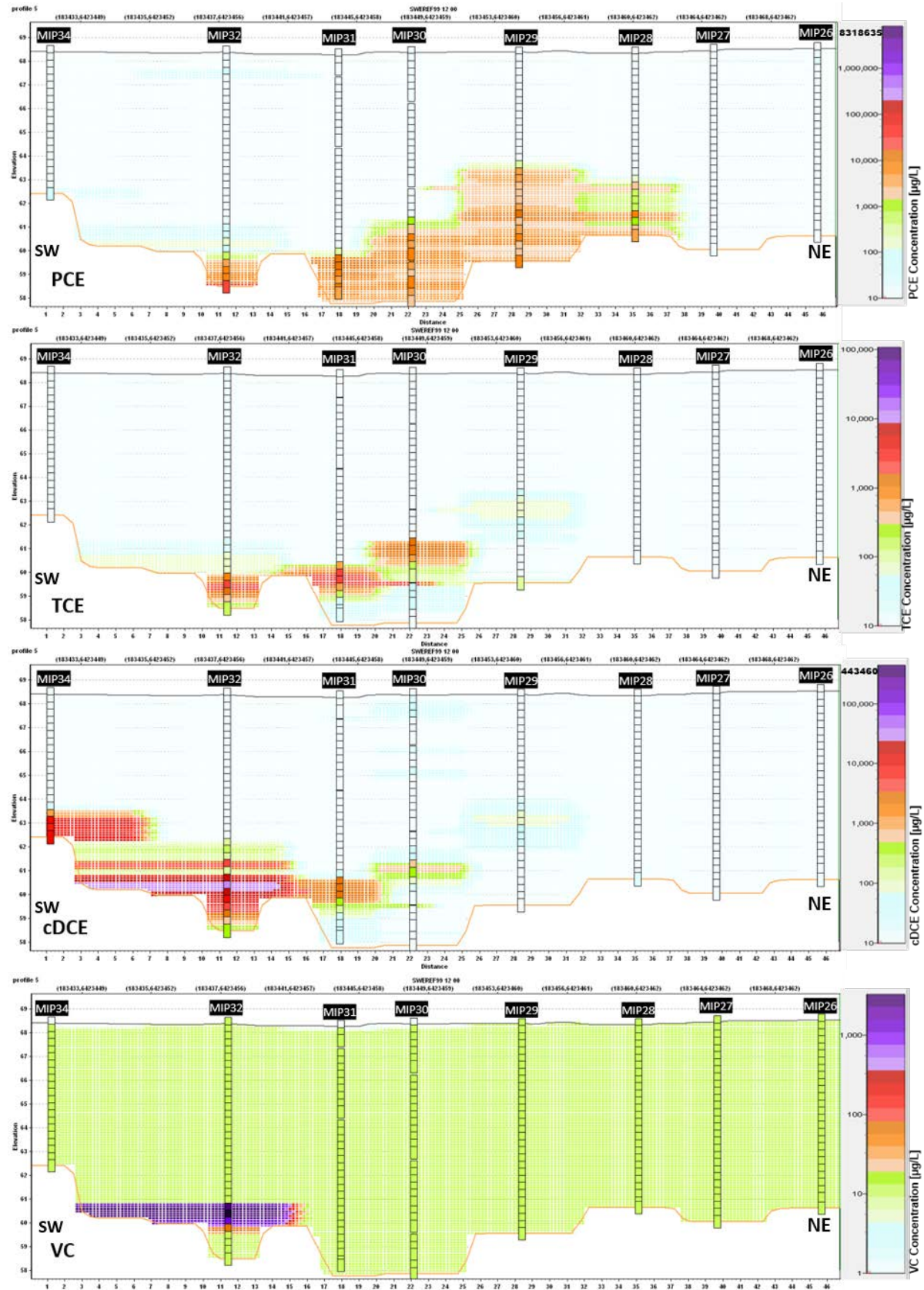


Figure 46. Together with Figure 47 are vertical slices along the profile 5 by contaminants.

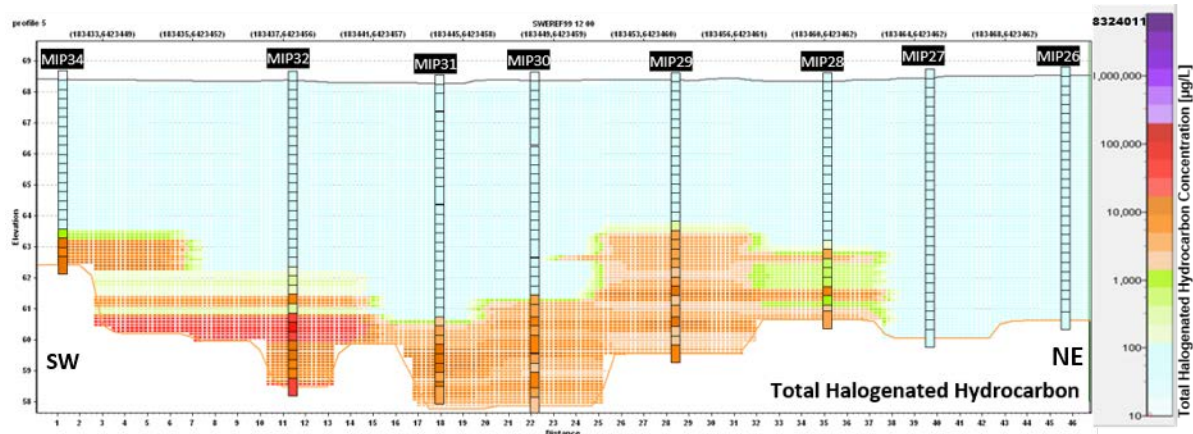


Figure 47. Together with Figure 46 are vertical slices along the profile 5.

The profile 5 is slightly different from other profiles. Instead of using a straight line to fit MIP-sounding probes, several line segments are used to perfectly cross the last eight MIP-sounding probes which are the remotest MIP-sounding probes from the dry-cleaning facility building.

As can be clearly noticed from the Figure 46 and Figure 47, all kinds of contaminants are situated close to the bedrock surface. However, different contaminants have quite distinct distribution features. For example, the high concentration zone of PCE is more extended to the North-East side of the profile 5, limited between MIP 32 and MIP 28. By contrast, the high concentration zone of TCE has a rather smaller area, between MIP32 and MIP30. The slightly higher concentration of TCE can also be found at MIP 29, both at the medium depth and bottom of the sounding probe.

The high concentration zone of cDCE has an opposite direction, in comparison with PCE. The bottom of the Sounding Probe MIP34 detected the relatively high cDCE, which does not detect the apparent concentration raise for PCE and TCE. Also, a sharp concentration transition can be noticed at the elevation of 61 m amsl of MIP-sounding probe 32.

Different from all the other vertical slices for VC, an extremely high concentration zone can be noticed at the lowest part of the MIP-sounding probe 32. The maximum concentration level of this zone is 3247 µg/L. Such high VC concentration zone is probably due to the intense degradation activities.

3.2.2 Horizontal slices over Alingsås site

Before visualising the horizontal slices, it is essential to explain how horizontal slices are cut to reasonably visualize the spatial distribution of the contaminants at different elevations horizontally. Due to the complex three-dimensional distribution of the contaminant, the horizontally cut slices cannot stand alone without considering the vertical changes. In other words, the horizontally spatial distribution of the contaminants changes by the elevation at which the slice is cut. However, not all slices can be cut and included here, only limited elevations of horizontal slices are extracted and exhibited in this thesis paper as representatives.

The terrain elevation, as well as that of the bedrock surface, has a distinct difference between the parking lot and the region inside the facility. If the horizontal slices are cut based on the general instructions such as depth from the terrain, or right above the bedrock surface, the result would not be able to achieve the purpose of these instructions due to the spatial elevation variation. Instead of adopting the general instructions while cutting horizontal slices, certain values of elevations are employed to better cover features. According to the conclusions from section 2.1.2, the trend of the elevation change is approximately southeast-northwest oriented, which can be assimilated to be perpendicular to the boundary between the boundary of the facility and the parking lot. Consequently, the orthodiagram (refer to Figure 48) of the drawn cross-section in Figure 37, can help determine the characteristic levels at which horizontal slices should be cut.

As can be concluded from Figure 48, in total, five horizontal slices were cut within the region where all the MIP-sounding probes were installed. The first horizontal slice was cut at the elevation of 69.52 m amsl, which targets on revealing the contaminant spatial distribution at the shallow area below the points MIP7, and MIP 8. The second slice was cut at the elevation of 68.71 m amsl, targeting on detecting the concentration level near the bedrock surface under the points MIP 7, and MIP8. Simultaneously, the shallow area below the major part of the facility can also be covered. The third slice was cut at the level of 67.01 m amsl, which is about 1.5 meters below the ground surface in the parking lot region. The fourth slice was cut at the elevation of 63.5 m amsl, which both covers the area around the bedrock surface under the inside facility region, and the medium depth beneath the parking lot region. The fifth slice was cut at the elevation level of 60.27 m amsl, which took care of the zone near the bedrock surface beneath the parking lot.

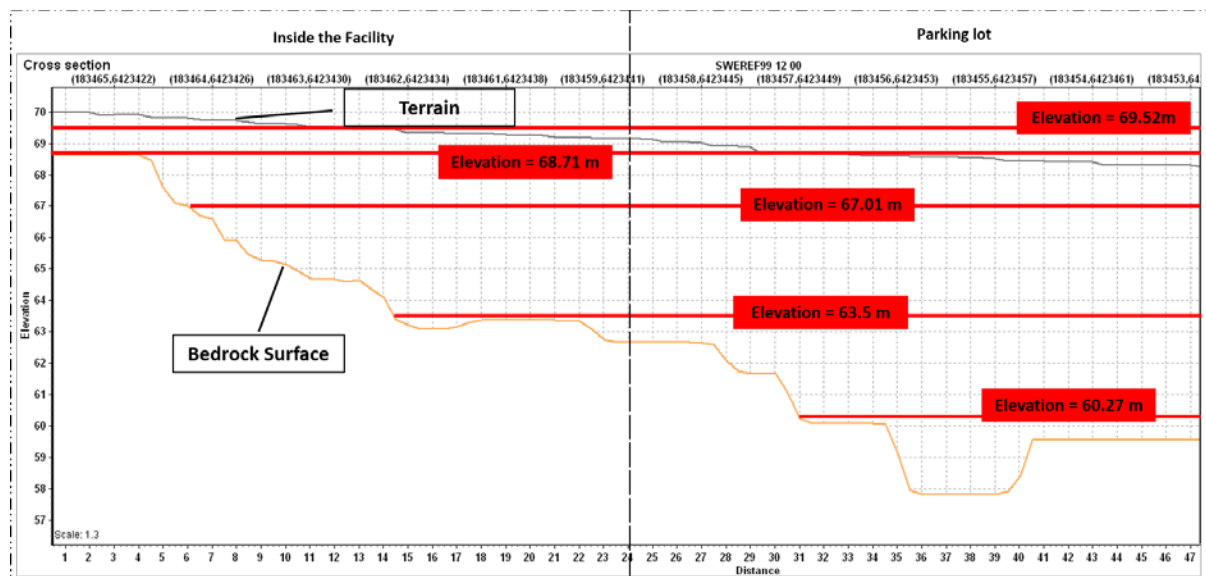


Figure 48. The sectional-drawing of the cross-section in Figure 37. Grey curve denotes the terrain surface while the orange curve denotes the bedrock surface. Red solid lines indicate how horizontal slices are cut, with the specific elevation value in red boxes. Two dashed-line box represents the region inside the facility, and the parking lot area respectively.

In this section, horizontal slices of five different elevation levels are displayed by contaminants. Since the distribution behaviour of the total halogenated hydrocarbon highly resembles that of the PCE, the

horizontal slices of the total halogenated hydrocarbon are not exhibited here. However, the distribution features inspected from these horizontal slices does not necessarily represent the real situation. This will be discussed in [section 4.2.1](#).

3.2.2.1 Horizontal slices for PCE by elevation levels:

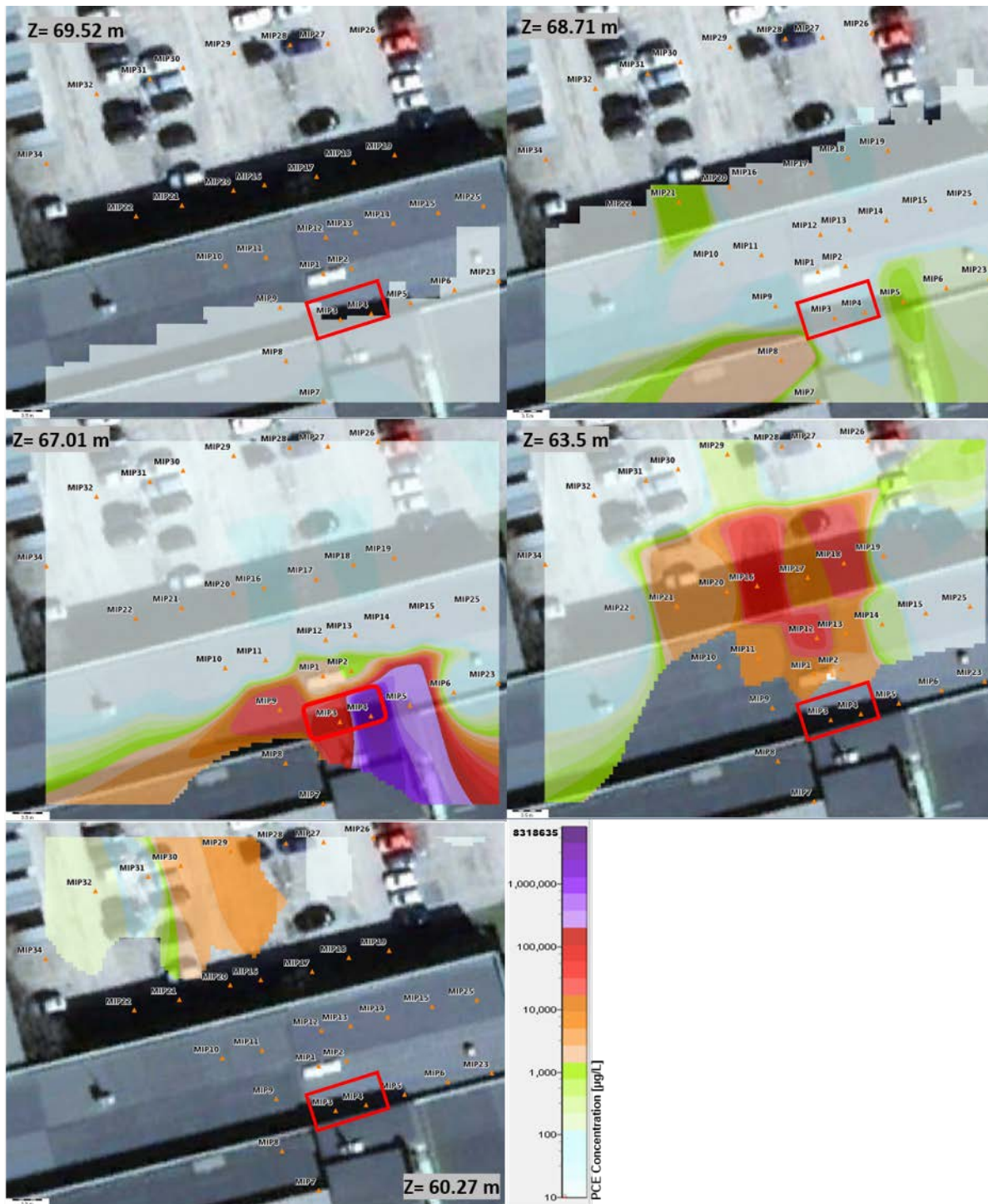


Figure 49. Horizontal PCE concentration distribution at different elevation levels of the Alingsås site. Red solid-line boxes represent the estimated position where the PCE leakage took place.

Figure 49 displays the horizontal slices for PCE at five different elevation levels. As can be illustrated, with the elevation level decreasing, the PCE concentration level displayed in corresponding horizontal slice goes higher. Such behaviour reflects the contaminants down-settling trend. Also, the highest PCE concentration level is found around MIP3 and MIP4 at the elevation level of 67.01 m amsl, among this set of horizontal slices. This corresponds will with the location where the historic leakage broke out

(red solid boxes). Due to the dissipation during the propagation process, the PCE concentration level near MIP31, MIP32, and MIP34 is much lower than the area closer to the leakage source.

Some confusing distribution behaviours can also be noticed. For instance, at the elevation level of 68.71 m amsl, two higher concentration zones can be witnessed surrounding MIP21 and MIP18. Since the contaminants are not supposed to move upwards, they are suspected to be measurement errors.

3.2.2.2 Horizontal slices for TCE by elevation levels:

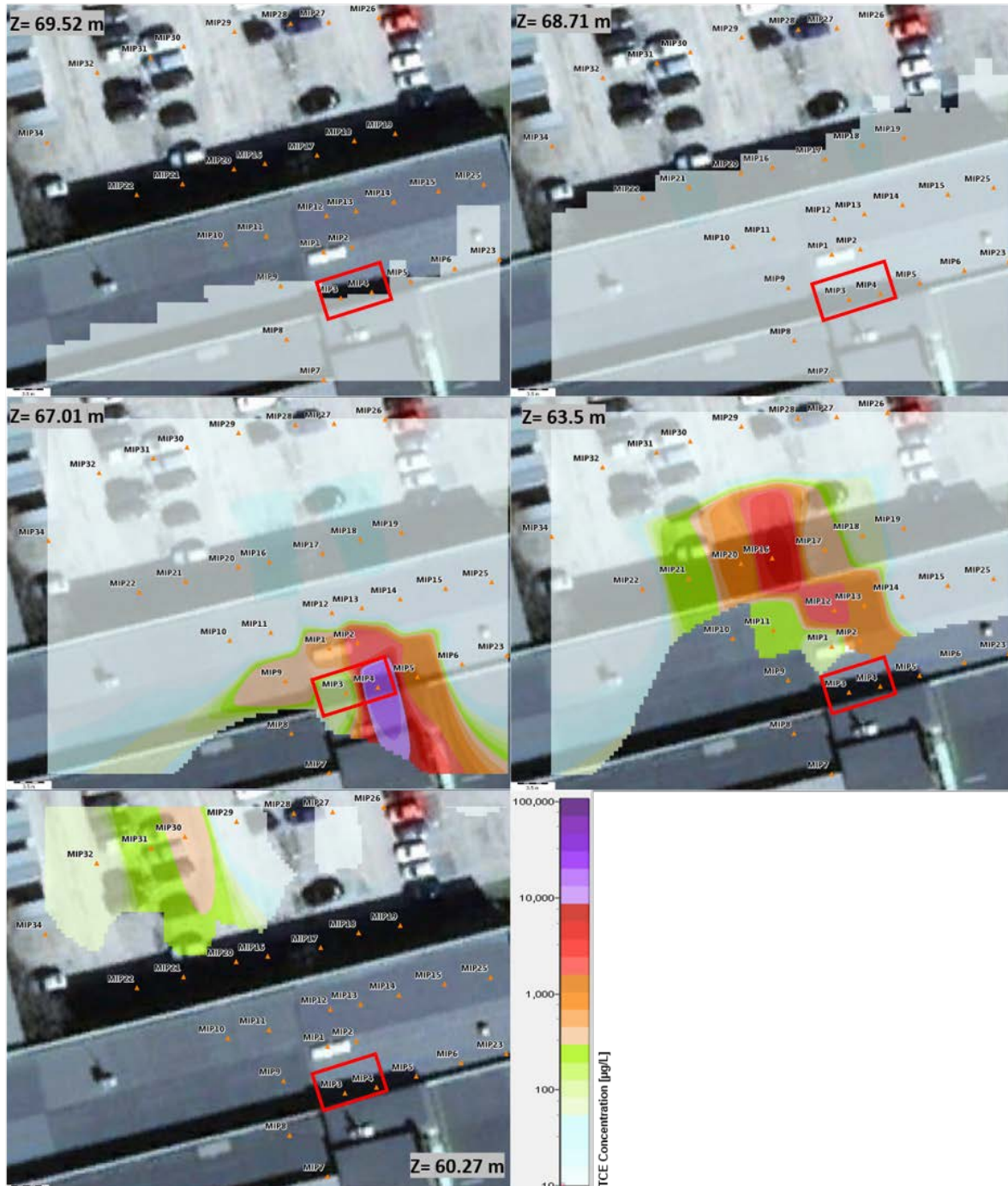


Figure 50. Horizontal TCE concentration distribution at different elevation levels of the Alingsås site. Red solid-line boxes represent the estimated position where the PCE leakage took place.

Figure 50 displays the horizontal slices for TCE at five different elevation levels. In comparison with the horizontal slices for PCE in Figure 49, TCE horizontal distributions have relatively similar behaviours. For example, with the elevation level decreasing, the TCE concentration level displayed in corresponding horizontal slice goes higher. Such behaviour reflects the contaminants down-settling

trend. Also, same type of confusing higher concentration zones can also be witnessed in TCE horizontal slices. Due to the same reason, they are suspected as measurement errors as well.

3.2.2.3 Horizontal slices for cDCE by elevation levels:

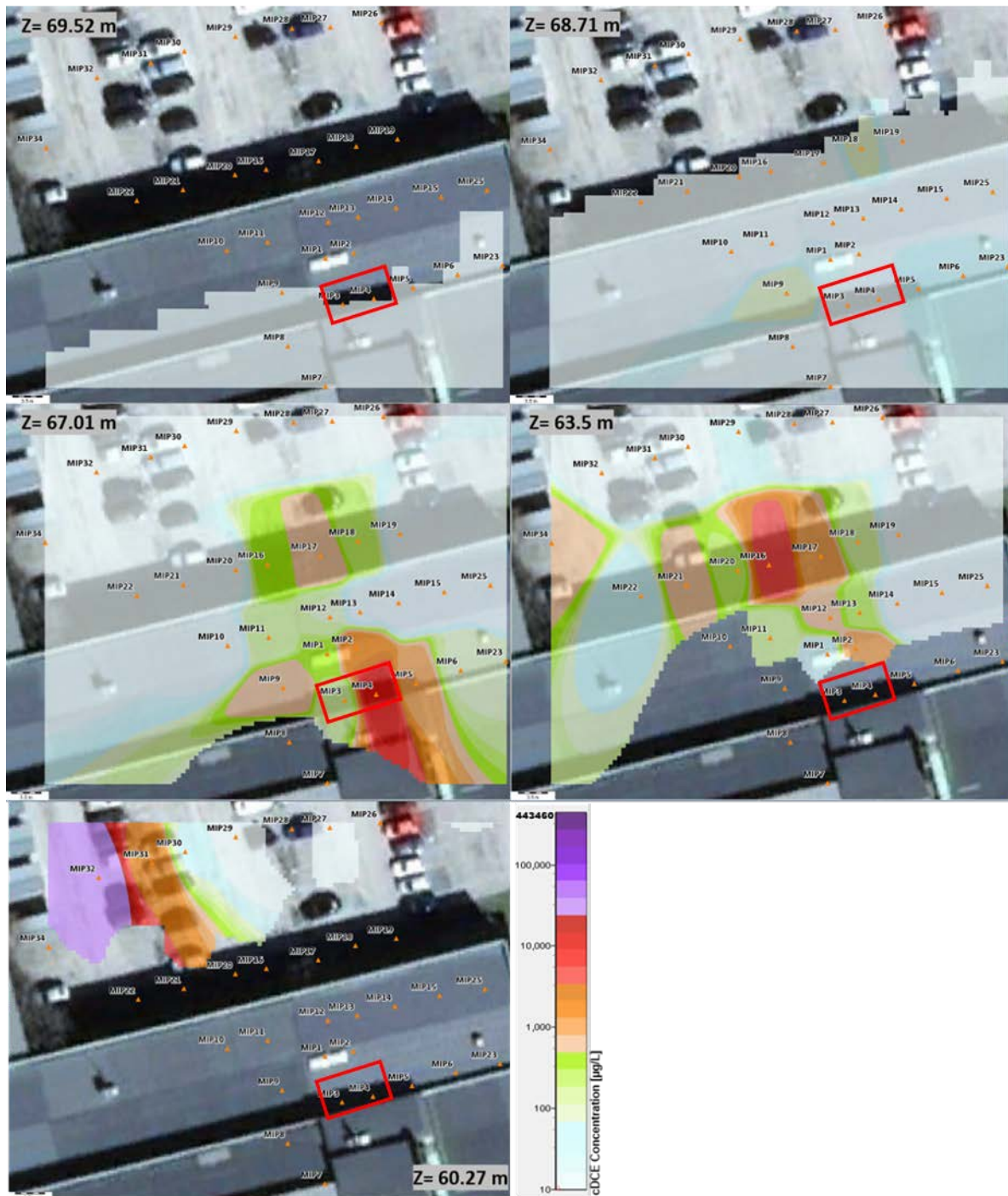


Figure 51. Horizontal cDCE concentration distribution at different elevation levels of the Alingsås site. Red solid-line boxes represent the estimated position where the PCE leakage took place.

Figure 51 displays the horizontal slices for cDCE at five different elevation levels. Similar to the horizontal slices for PCE in Figure 49 and horizontal slices for TCE in Figure 50, the general concentration level for cDCE increases with the reducing elevation level.

Another feature that is worthy of being mentioned is that the cDCE concentration level at the elevation level of 60.27 m amsl is above 10,000 µg/L. This concentration level is much higher than that of the PCE (above 100 µg/L) and TCE (above 400 µg/L) at the same elevation level.

3.2.2.4 Horizontal slices for VC by elevation levels:

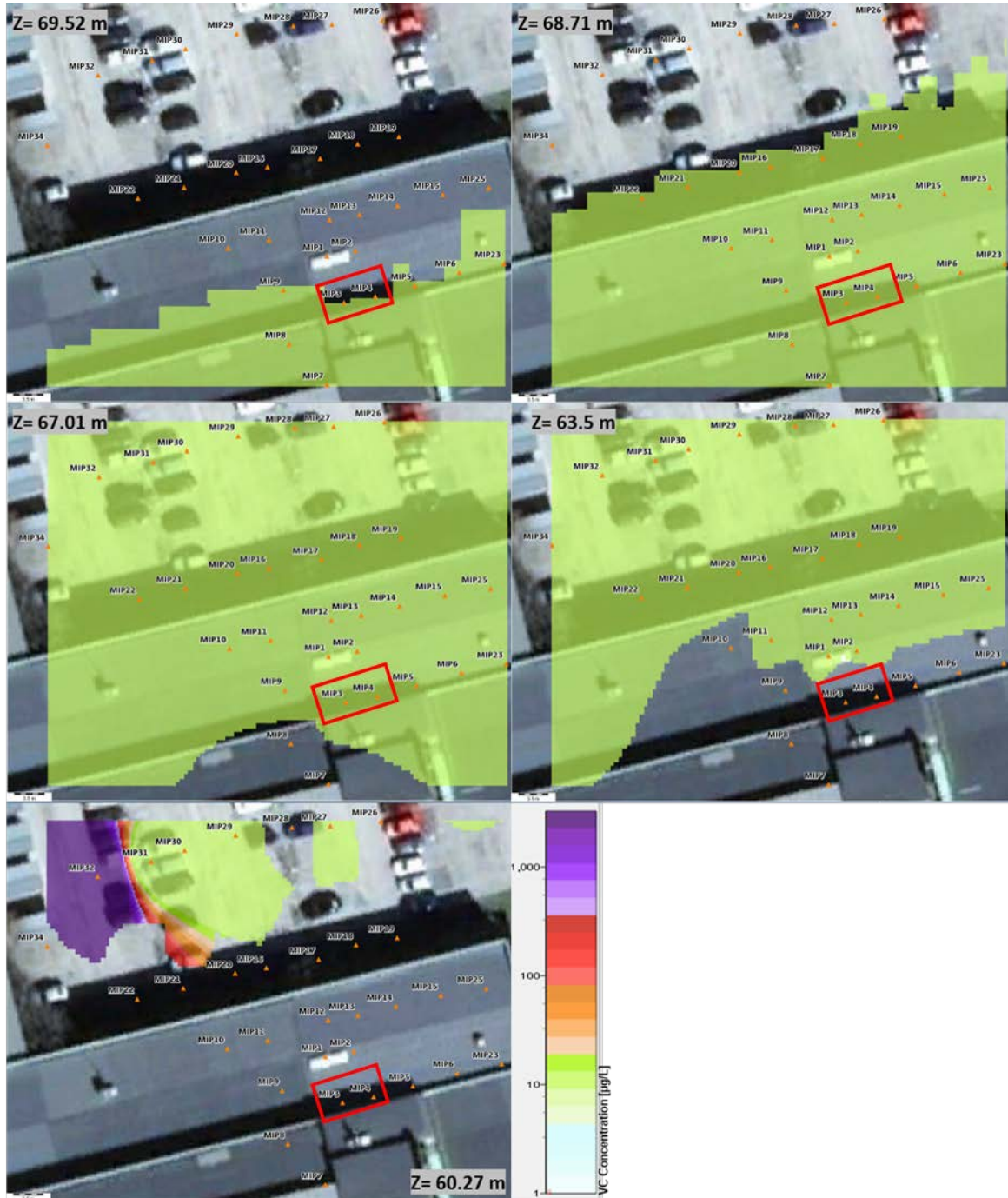


Figure 52. Horizontal VC concentration distribution at different elevation levels of the Alingsås site. Red solid-line boxes represent the estimated position where the PCE leakage took place.

The VC, as a whole, can be hardly detected at the site, at all elevation levels. One obvious exception is the high VC concentration zone surrounding the MIP32, with more than 1000 µg/L.

Overall, from the horizontal slices for PCE, TCE, cDCE, and VC, the concentration distributions of different contaminants show a considerable spatial difference. The tendency that concentration increases with the decreasing elevation level can be witnessed from horizontal slices for PCE, TCE, and cDCE, which reflects the down-settling trend for these three contaminants. Some confusing concentration distribution features can also be noticed in horizontal slices for PCE (Figure 49), and TCE (Figure 50), at the elevation levels of 68.71 m amsl and 67.01 m amsl. Since these two substances are not likely to be transported to such shallow region, these confusing distribution features are suspected to be measurement errors and will be further discussed in section 4.2.2.

3.2.3 Iso-surfaces generated for the Alingsås site

The iso-surfaces (Figure 53) generated for the Alingsås site are aimed at locating the positions of the highest concentration thresholds for different contaminants. In the top left corner of each small figure, the iso-value of each contaminant adopted to generate the iso-surface is marked out. They all are within the highest concentration range of each contaminant measured in this set of MIP-sounding.

The generated iso-surfaces can also be understood as contour surface in 3D. The contour surface is rendered where the value in the grid exactly matches the adopted iso-value. In this case, the volume that wrapped up by the 3D contour represents the higher concentration values in comparison with the adopted iso-values. Combined with the meaning of the adopted iso-value, the volumes that wrapped up by such 3D contour surface, consequently, represents the highest concentration body of each contaminant in this set of MIP-sounding. They are visualised as purple clouds in Figure 53.

The highest concentration zone of PCE appears inside the dry-cleaning facility at the MIP-sounding probe 3. The highest concentration zones of TCE and cDCE are the same, which are both situated at the MIP-sounding probe 16. However, the elevation levels of them vary a little bit. The highest concentration zone of VC is located at the MIP-sounding probe 32. The positions of these MIP-sounding probes can be looked up in Figure 52.

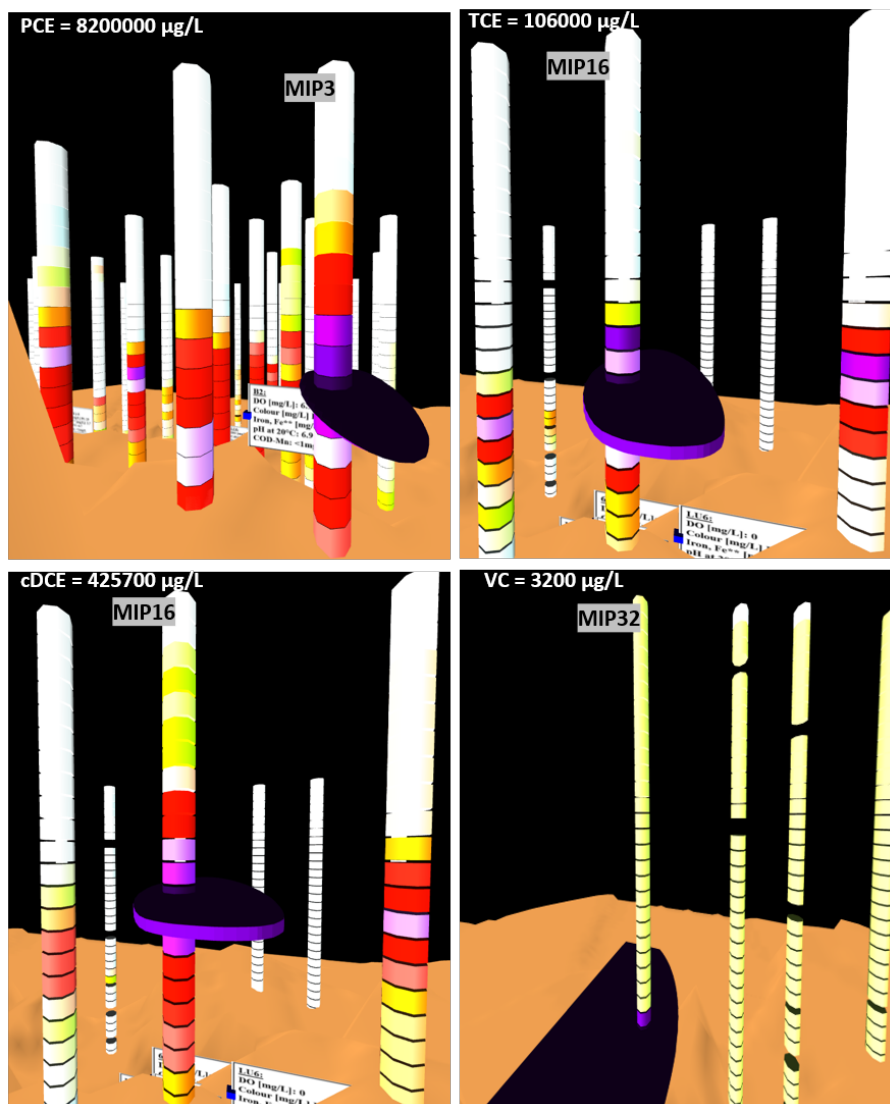


Figure 53. Iso-surfaces generated for different contaminants. The Iso-value of each iso-surface is displayed in the top left corner. These Iso-values represent the highest concentration range of each contaminant. The purple clouds are the volumes wrapped up by these generated iso-surfaces (contours). They represent the highest concentration bodies of PCE, TCE, cDCE, and VC in this set of MIP-sounding.

3.3 Degradation State for MIP-sounding Measurements

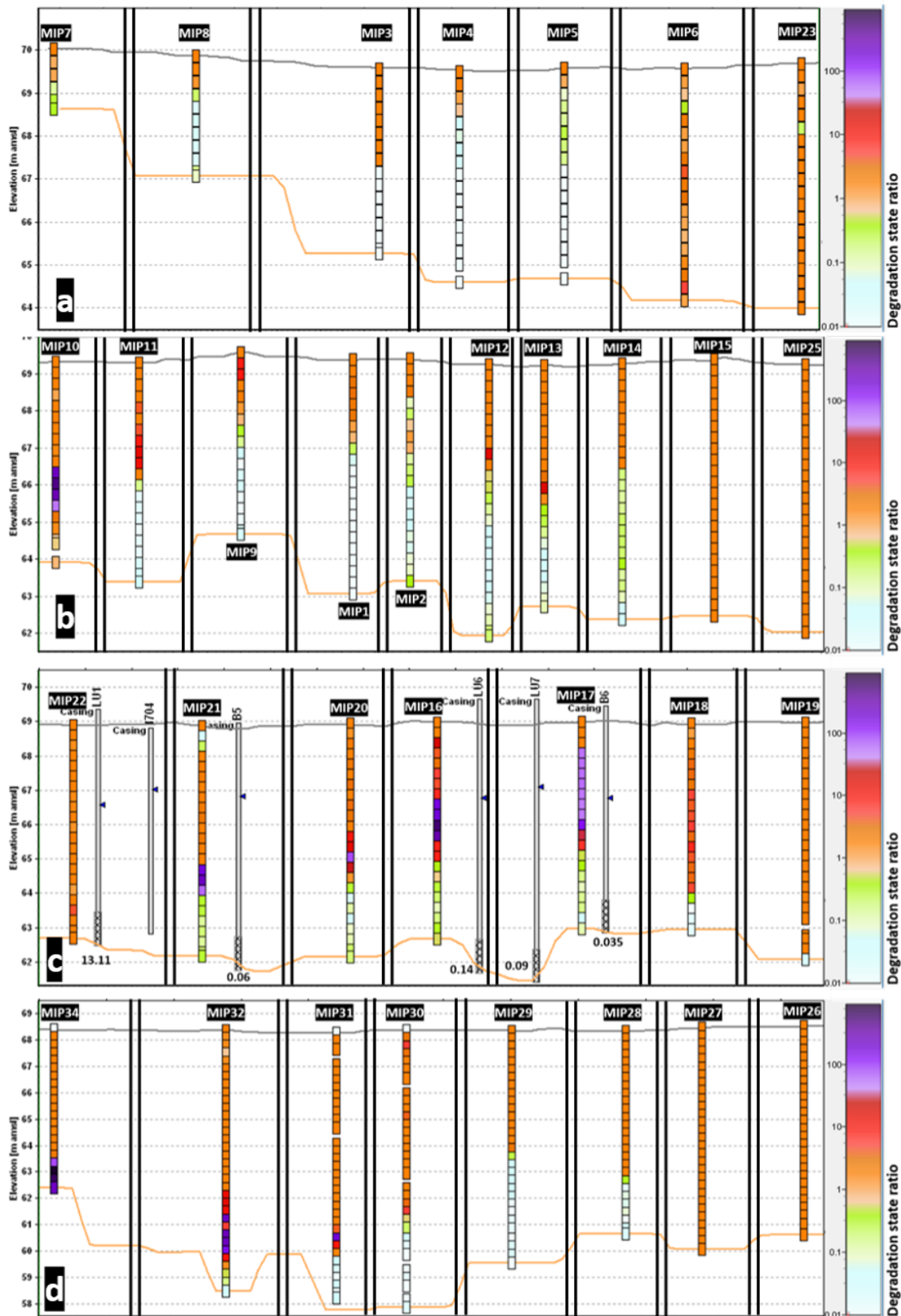


Figure 54. Profiles cuts for the visualization of the degradation state for all MIP-sounding measurements data points. The groundwater sampling pipes within two-meter buffer distance are also included here with the degradation states of the groundwater samples.

Figure 54 display the degradation state for all MIP-sounding data points. The location of these MIP-sounding probes can be referred to Figure 49. The MIP-sounding probes along Figure 54a and Figure 54b are installed inside the dry-cleaning facility, and closely situated to the PCE leakage position. MIP-sounding probes along Figure 54c and Figure 54d are installed outside the dry-cleaning facility, within the parking lot area.

The degradation state ratio of MIP-sounding probes installed inside the dry-cleaning facility generally have relatively low ratio values which possibly indicate a lower degradation level. However, MIP-sounding probes such as MIP10 and MIP11 are exceptions. Some high ratio values can be witnessed along these two MIP-sounding probes.

The degradation state ratio of MIP-sounding probes installed outside the dry-cleaning facility, overall, have relatively higher ratio values, which can be related to the more intense degradation activities. Medium elevation level of MIP16, MIP17, MIP20, and MIP21, as well as lower elevation level of MIP31, MIP32, and MIP34, all show considerably high ratio values. At these positions, the total halogenated hydrocarbons are dominated by the metabolites.

Groundwater samples within 2-meter buffer distance are also visualised in Figure 54c. The ratio values among these groundwater samples correspond well with those of nearby MIP-sounding data points.

3.4 DCIP inversion results

In this section, the inversion results of all four DCIP horizontal lines from the third-day measurement (3rd November 2017) are shown here. Note that only the inversions of line 1 and line 2 use the bedrock boundary information from the borehole logs along these two lines. However, no bedrock boundary information is used for the inversions along line 3 and line 4.

Line 1 is closely situated nearby the dry-cleaning facility building with a distance of 1.1 meters approximately. Consequently, this line is potentially under considerable 3D effect caused by the dry-cleaning facility building. Figure 55 displays inverted sections of DCIP line 1 with superposed geological reference data (a-c). The top grey line represents the terrain surface while the bottom orange line represents the bedrock surface. Figure 55a displays the resistivity inversion section along line 1 and the black points denote the buried electrodes for DCIP measurement. The near surface zone shows a relatively high resistivity level. A high-resistive anomaly can be noticed in dashed line box ②. Figure 55b exhibits the IP inversion section along line 1. The chargeability values are generally high with four extreme higher anomalies (dashed line boxes). Figure 55c displays the normalized chargeability profile. The general high background IP response, and the four chargeability anomalies are still visible in this profile. Figure 55d displays the chemical reference data (total halogenated hydrocarbons) along this line. However, the provided chemical reference data can be barely correlated with the resistivity and IP anomalies. Also, no anomalies of DCIP inversion results can be correlated with the stormwater pipes.

Line 2 is parallelly situated approximately 3.2 meters northward of line 1. The DCIP inverted sections with superposed geological reference data (a-c) can be seen in Figure 56. Figure 56a displays the resistivity inversion section. The black points in the shallow part represent the buried electrodes. Two point anomalies are marked out with dashed line box ①. The anomaly in dashed line box ② can also be noticed in line 1 and line 3. Two vertical lower resistive zones are marked out with dashed line box ③ and ④. Figure 56b displays the IP inversion section. Four manifest anomalies are marked out with four dashed line boxes. Figure 56c displays the section of the normalized chargeability. The central anomalies (dashed line boxes ⑤ and ⑥) in Figure 56b are still visible in the normalized chargeability profile. Four assumptions are brought up in regards of these anomalies and discussed in section 4.3. Figure 56d displays the chemical reference data (total halogenated hydrocarbons). This chemical reference data does not have strong correlation with the resistivity and IP data. Two strings of black points can be noticed near MIP20 and LU7, they represent the TDR sensors.

Line 3 is parallelly situated approximately 3.6 meters northward of line 2. [Figure 57](#) presents inverted sections along this line with superposed geological reference data (a-c). [Figure 57a](#) displays the resistivity inversion profile and the black points in the shallow part represent the buried electrodes. A layer of manifest high resistivity values can also be witnessed at this shallow part. To the right edge, an anomaly is marked out with dashed line box ❶. [Figure 57b](#) displays the IP inversion section and two anomalies are marked out with dashed line boxes. They are suspected to be caused by bulbous effect. [Figure 57c](#) displays the normalized chargeability section. The central anomalies (dashed line boxes ❷ and ❸) in ([Figure 57b](#)) are still visible in [Figure 57c](#), though the one below the bedrock surface is not as apparent as in [Figure 57b](#). [Figure 57d](#) displays the chemical reference data (total halogenated hydrocarbons). The shape of the contaminant plume approximately follows the shape of the bottom high resistivity layer in [Figure 57a](#).

[Figure 58](#) shows sections of DCIP line 4 with superposed geological reference data (a-c). [Figure 58a](#) displays the resistivity inversion section and the black points in the shallow part represent the buried electrodes. A layer of manifest high resistivity values can also be witnessed at this shallow part. [Figure 58b](#) exhibits the IP inversion section. The chargeability is generally very low. However, one evident anomaly can be seen at the bottom. This anomaly is invisible after chargeability normalization ([Figure 58c](#)). [Figure 58d](#) displays the chemical reference data (total halogenated hydrocarbons). The shape of the contaminant plume approximately follows the shape of the bottom high resistivity layer in [Figure 58a](#).

3.4.1 Inversion results along line 1

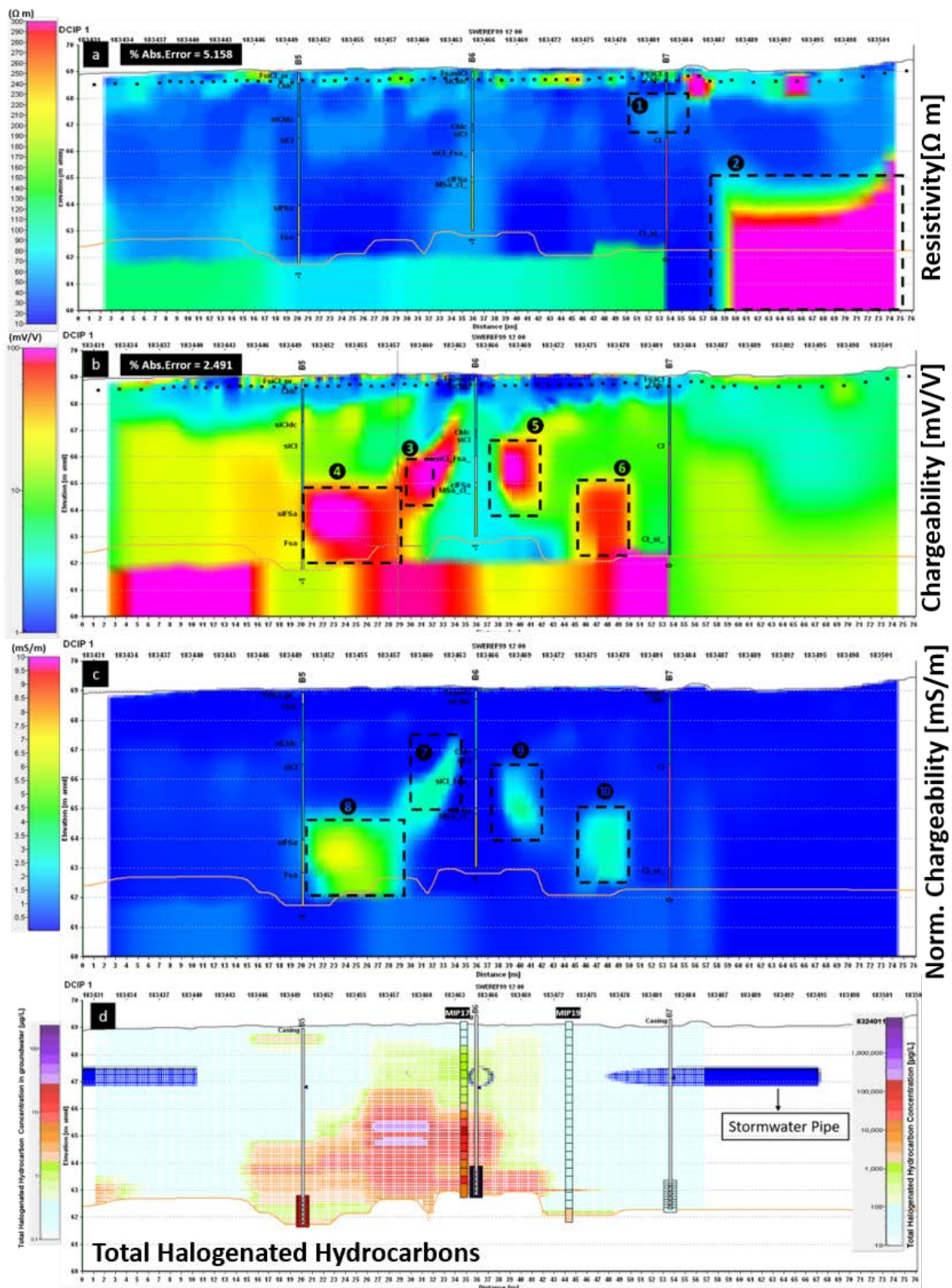


Figure 55. Inverted sections of DCIP line 1 with superposed geological reference data (a-c). The top grey line represents the terrain surface while the bottom orange line represents the bedrock surface. a) The black points denote the buried electrodes for DCIP measurement. The near surface zone shows a relatively high resistivity level. An obvious resistivity contrast zone can be seen in B7 between the dry clay layer and clay layer (dashed line box ①). Also, a high-resistive anomaly can be noticed in dashed line box ②. b) The chargeability values are generally high with four extreme higher anomalies (dashed line boxes). High anomalies can also be detected below the bedrock surface. c) The general high background IP response, and the four chargeability anomalies are still visible in the normalized chargeability profile. However, the anomaly below the bedrock surface can be barely distinguished. d) The chemical reference data can be barely correlated with the resistivity and IP

anomalies. To the left side of the cross-sections are legends for contaminants concentration in groundwater (S. Åkesson, pers.com., 2018-04-05). No anomalies can be correlated with the stormwater pipes either.

3.4.2 Inversion results along line 2

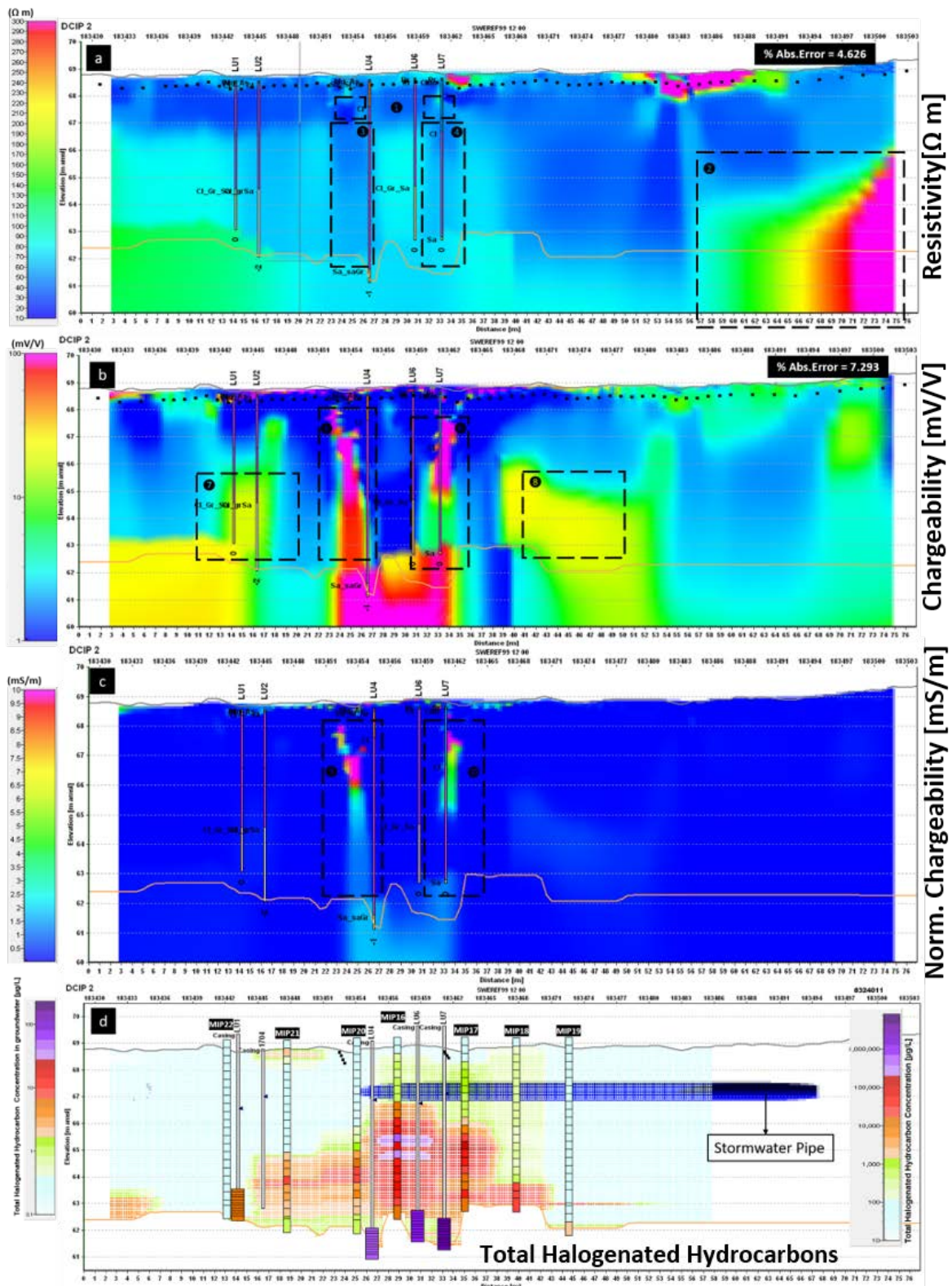


Figure 56. Inverted sections of DCIP line 2 with superposed geological reference data (a-c). The top grey line represents the terrain surface while the bottom orange line represents the bedrock surface. a) The black points in the shallow part represent the buried electrodes. Two point anomalies are marked out with dashed line box ①. The anomaly in dashed line box ② can

also be noticed in line 1 and line 3. Two vertical lower resistive zones are marked out with dashed line box ③ and ④. b) Four manifest anomalies are marked out with four dashed line boxes. c) The central anomalies (dashed line boxes ⑤ and ⑥) in (b) are still visible in the normalized chargeability profile. d) The chemical reference data does not have strong correlation with the resistivity and IP data. To the left side of the cross-sections are legends for contaminants concentration in groundwater (S. Åkesson, pers.com., 2018-04-05). Two strings of black points can be noticed near MIP20 and LU7, they represent the TDR sensors.

3.4.3 Inversion results along line 3

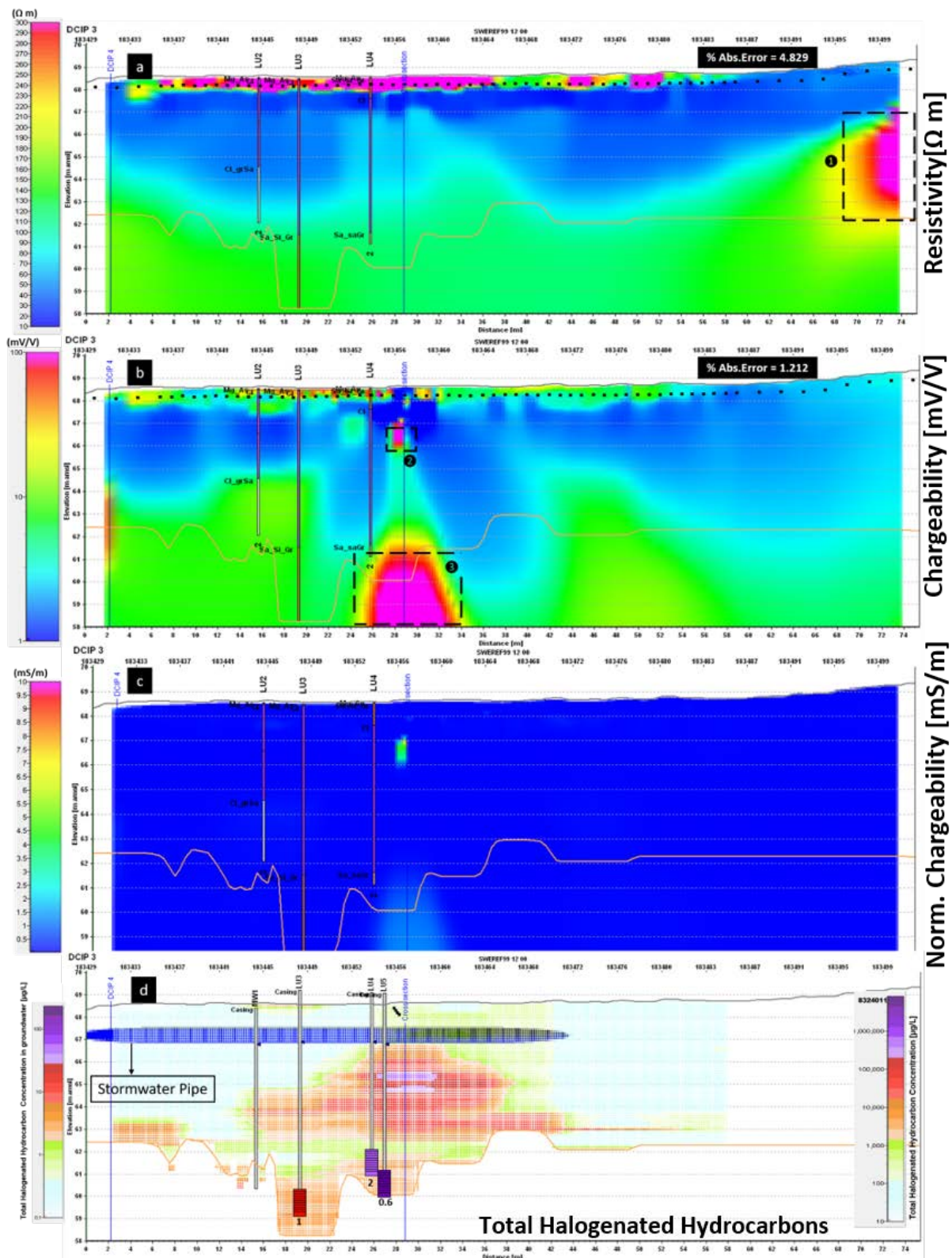


Figure 57. Inverted sections of DCIP line 3 with superposed geological reference data (a-c). The top grey line represents the terrain surface while the bottom orange line represents the bedrock surface. a) The black points in the shallow part represent the buried electrodes. A layer of manifest high resistivity values can also be witnessed at this shallow part. To the right edge, an anomaly is marked out with dashed line box ①. The high resistivity layer goes higher than the recorded bedrock level. b) Two anomalies are marked out with dashed line boxes. c) The central anomalies (dashed line boxes ② and ③) in (b) are still visible in c), though the one below the bedrock surface is not as apparent as in (b). d) The shape of the contaminant plume

approximately follows the shape of the bottom high resistivity layer in a). To the left side of the cross-sections are legends for contaminants concentration in groundwater (S. Åkesson, pers.com., 2018-04-05).

3.4.4 Inversion results along line 4

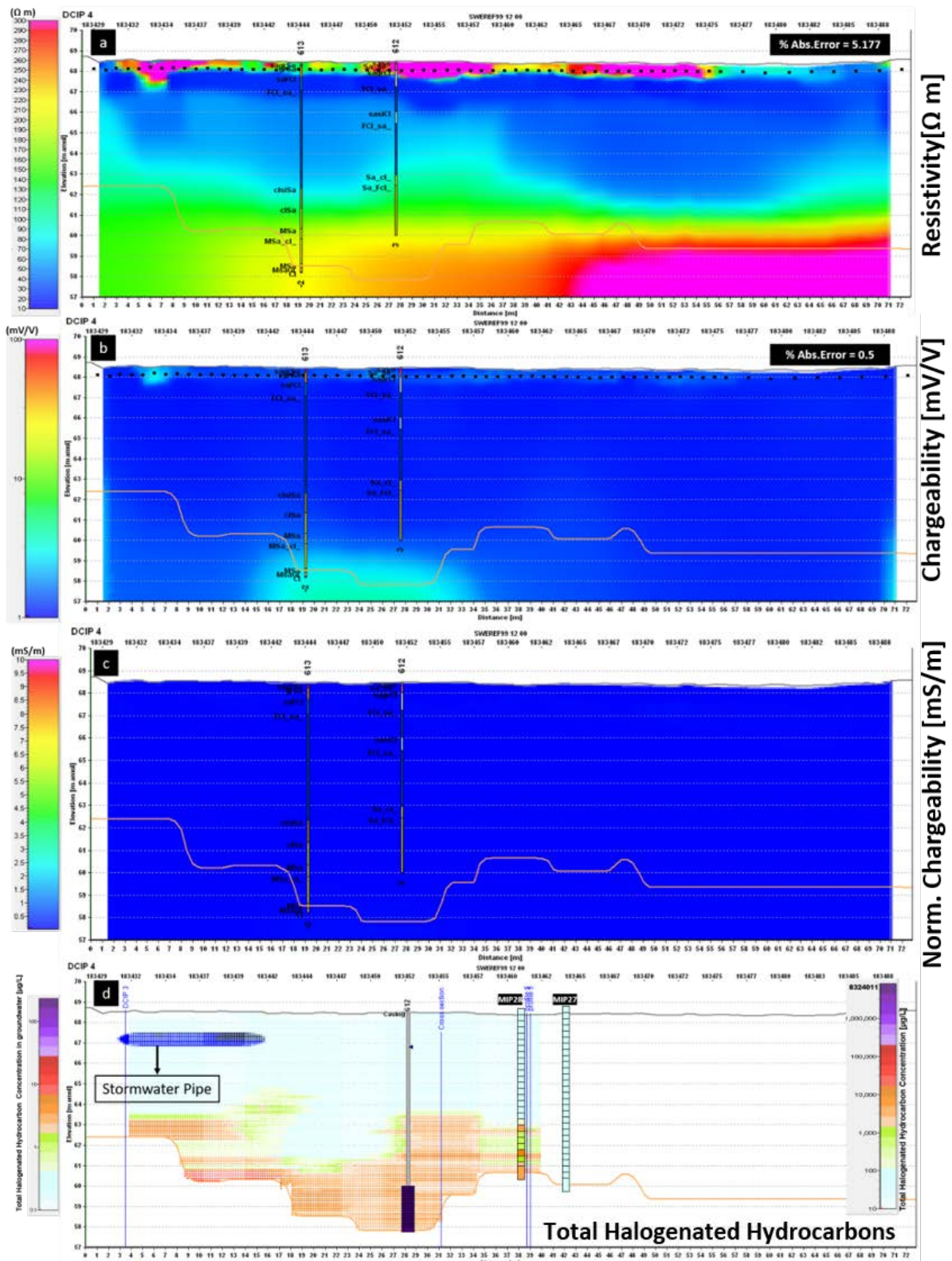


Figure 58. Inverted sections of DCIP line 4 with superposed geological reference data (a-c). The top grey line represents the terrain surface while the bottom orange line represents the bedrock surface. a) The black points in the shallow part represent the buried electrodes. A layer of manifest high resistivity values can also be witnessed at this shallow part. Bottom high

resistivity zone goes above the bedrock level. b) The chargeability is generally very low. However, one evident anomaly can be seen at the bottom. c) The bottom anomaly is invisible in normalized chargeability profile. d) The shape of the contaminant plume approximately follows the shape of the bottom high resistivity layer in a). To the left side of the cross-sections are legends for contaminants concentration in groundwater (S. Åkesson, pers.com., 2018-04-05).

4. Interpretation & Discussion

4.1 Interpolated surfaces

Interpolated groundwater free surface, interpolated bedrock surface, and the terrain surface provide the most important boundary information in this refined geological model. Consequently, it is quite important to evaluate how well these boundaries are fitted to the reality. Setting aside the terrain layer which is directly provided by © Lantmäteriet, the interpolated surfaces can be assessed by comparing with the corresponding results from previous investigations.

For example, the evaluation of the interpolated bedrock surface can be implemented by comparing between [Figure 8](#) and [Figure 35](#). Despite the fact that different sets of the measurement points were adopted to provide bedrock elevation information, the overall trends of the spatial variation of the bedrock surface elevation in the interpolated bedrock surfaces are quite alike. However, some disparities should also be noticed. Within the dry-cleaning facility area, at point MIP 7 especially, the depth of the bedrock in this thesis work is 1.4 meters approximately (according to the field notes), which was collected while installing the MIP-sounding probe 7. In contrast, the corresponding position in [Figure 8](#) shows that the depth of the bedrock is 4 meters, which is approximately three times deeper. A possible reason for such large discrepancy might be due to potential errors related to point MIP 7. Firstly, in the previous investigation, while the bedrock surface was interpolated, no bedrock information was provided at the position of the MIP 7 point. The isoline of the depth to bedrock surface displayed around the MIP 7 point position in [Figure 8](#) was only a rough estimation according to the overall spatial distribution of the bedrock depth. Secondly, the bedrock information provided by the MIP 7 point is based on the assumption that all the MIP sounding probes were installed until the bedrock surface was reached. The installation of the MIP probe 7 might have been intervened at that elevation level, caused by other issues. However, no installation log can be found with respect to MIP sounding probes. Overall, the variance of the bedrock depth will affect the estimation of the volume of the contaminated soil.

Overall, in spite of the potential errors related to the bedrock information at the point MIP 7, the interpolated bedrock surface is quite reasonable, which is by virtue of the moderately densely distributed bedrock elevation data points provided. By contrast, the limited, and unevenly distributed groundwater free surface level points make it even harder to interpolate a fairly accurate result. In comparison with the interpolated groundwater free surface in this thesis work ([Figure 36](#)), the hydrogeological condition concluded from the previous investigation ([Figure 11](#)) shows a more regular trend of the groundwater level spatial change.

Another factor that might also lead to the poor interpolation result is the absent calibration of the inspected groundwater free surface levels. As is described in [section 2.1.3](#), the local hydrogeological setting is likely confined or leaky confined aquifer. For the groundwater surface level measurement under such hydrogeological conditions, two points need to be noticed.

Firstly, the directly inspected groundwater surface from the well casing does not necessarily represent the authentic groundwater level in the aquifer, instead, this directly inspected groundwater level can only be referred to as groundwater free surface level. As is illustrated in [section 2.1.3](#), one representative feature of such confined (or leaking confined) aquifer is the pressurized groundwater in the bottom sand layer (Fetter, 2013). Due to such pressure, the inspected groundwater level will rise a considerable distance above the top surface of the aquifer, which is described in [Figure 59](#).

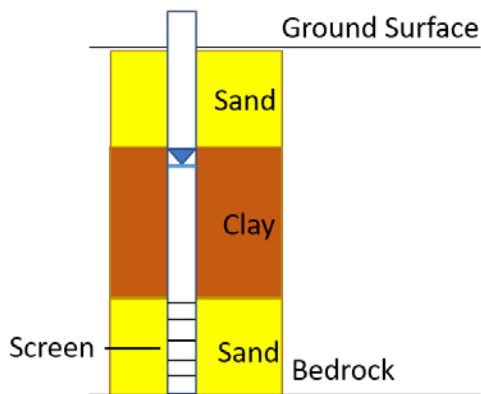


Figure 59. The well is placed through the confined aquifer. Due to the pressurized zone under the clay, the inspected groundwater level stays in the clay layer.

In our case, the inspected groundwater levels mostly stay in the clay layer (refer to Figure 60), which confirmed the aquifer to be confined aquifer in general.

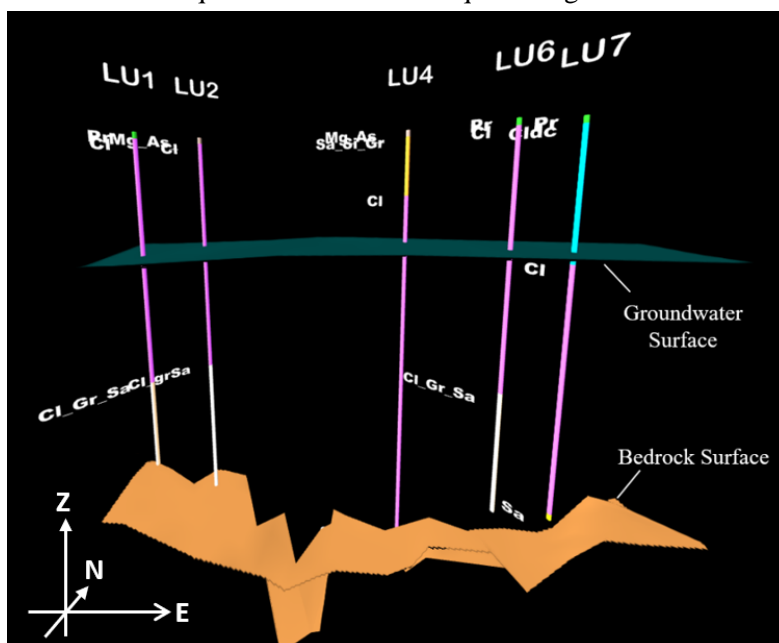


Figure 60. The inspected groundwater level of the Alingsås site mostly stays in the clay layer.

Secondly, the screen level, as well as the surrounding geological material of the screen is essential. Although the directly inspected groundwater level cannot provide the authentic groundwater level in the aquifer, the groundwater free surface level can still provide other information such as the hydraulic gradient of the aquifer. However, to attain this, the inspected groundwater levels are in need of careful calibrations based on the surrounding geological materials of the screens. For example, if one of the screens is surrounded by a layer of clay which bears an extremely low permeability, the groundwater can hardly flow into the well through the screen. This will result in a relatively low groundwater level inspected from the well. While another screen is surrounded by a layer of coarse sand which tends to have a considerably high permeability. Correspondingly, the groundwater can flow through the screen into the well in a smoother way without any barriers. This will result in a high inspected groundwater level, which can also reflect the authentic groundwater free surface level.

The Alingsås site is even more complex, with the undulating bedrock level, as well as the layers in a mixture of clay, sand, and gravels. Even if the screens are installed at the same depth below the ground surface, the complex condition mentioned above cannot guarantee that groundwater flows into the well at the same flow rate. Not to say the missing filter levels of five groundwater sampling pipes, it is a pity that the groundwater surface was interpolated from these inspected groundwater levels without proper correction. Conservative attitudes should be held while verifying the interpolated groundwater surface

with the result from the geophysical measurements since this interpolated groundwater surface cannot truly reflect the spatial trend of the groundwater level.

Also, both the highest and lowest groundwater level of the previous investigation at the Alingsås site are higher than that of this thesis work. It is probably due to the seasonal groundwater elevation change between spring and autumn. The groundwater depression zones from both investigations do not exactly correspond to each other but are quite close. Nevertheless, it is rather hard to determine the exact cause of the depression zone and the shift of it with the limited hydrogeological information provided. However, one suspicion was drawn that borehole LU1 might be clogged. The dredging of the borehole LU1 will be conducted in the coming fieldwork and it awaits to be seen if this is the cause of depression.

4.2 Contaminants three-dimensional distribution

4.2.1 Assessment of the 3D interpolation of MIP-soundings

Besides the original data points which were directly derived from the MIP-sounding probes and the groundwater sampling pipes, the perception of the contaminants three-dimensional distribution highly relies on how well the interpolation of these original data points was carried out. Before going deep into the analysis of the contaminants distribution features, it is essential to evaluate the interpolation result.

The evaluation of the interpolation results can be conducted through the slices along profile 1 and profile 2 (Figure 38, Figure 39, Figure 40, and Figure 41). Both profiles cross through seven MIP-sounding probes. As can be examined from these four figures, the concentration values of the interpolated points follow the concentration values of the original data points well. Even when the abrupt concentration change (more than a factor of 10) occurs between two adjacent points (with 0.1 meters), this feature is also well preserved by the interpolated points, and the corresponding sharp boundaries can be seen, such as the dashed-line boxes ② and ③ in Figure 38.

Albeit, interpolation points seem to follow the features of the original data points well, the interpolation results should be taken with a grain of salt due to the unevenly distributed data points. As a statistical analysis method, how close the interpolation result is to the reality is determined by how evenly and densely the given data point is distributed. At the Alingsås site, the vertical direction has denser data original data points in comparison with the horizontal direction. According to Figure 37, the distribution of the MIP-sounding points made up five parallel lines. The distance between two horizontally adjacent point range from 2 meters to more than 10 meters. With no extra data points provided in between such a large distance, the horizontal interpolation is not as reliable as the vertical interpolation. Under some conditions when the two horizontally adjacent sounding probes have a considerably large concentration gap, such as the MIP-sounding probe 13 and MIP-sounding probe 14 in Figure 40 for TCE, the gradient of the concentration transition is hard to be precisely predicted without more information provided. As can be noticed from the right edge of the dashed-line box ④ in Figure 40, the input smoothing factor is forcing the plume to smooth out the concentration gap, which follows the natural behaviours in most of the cases. Even if in some zones a considerable sharp concentration change occurs between two adjacent points, such natural behaviour might not be fully applicable here.

In addition to the general evaluation of the interpolation result, some other suspicions should be harboured towards the zones close to the terrain surface and bedrock surface. For example, in Figure 38 for PCE, at the distance between 17 meters to 22 meters, a bowl-shaped groove can be noticed. The distribution of the PCE concentration tends to be a bit irregular with the right part of the bowl tends to be more affected by MIP17 and the left part of the bowl tends to be more influenced by the lower concentration level of MIP 20 and MIP 21. However, in the reality, the concentration level inside this groove might not be affected by neither of sides if the bedrock is assumed to bear a poor permeability. Such local boundary limitation is actually not taken into consideration when the interpolation is carried out. Instead, the perfectly fit interpolation along the terrain as well as the bedrock surface is simply a

cut-off function when the interpolation is finished. Analogous examples can be identified from the inverted pyramid at the distance of 5 meters in [Figure 44](#) for TCE.

Overall, it is a fairly satisfying three-dimensional interpolation result. However, due to the original data points distribution as well as the controversial interpolation zones near the terrain and bedrock surface, the interpolation results should not be over-interpreted. The vertical concentration interpolations are likely to be more reliable than the horizontal interpolations. Vertical slices crossing through MIP-sounding probes have the highest credibility.

4.2.2 Contaminants Distribution features

Speaking of the overall distribution behaviours of the contaminants at the Alingsås site, vertical slices along profile 1, profile 2 and profile 5 ([Figure 38](#), [Figure 39](#), [Figure 40](#), [Figure 41](#), [Figure 46](#), and [Figure 47](#)), vertical slices along cross-section ([Appendix iii](#), [Appendix iv](#), and [Appendix v](#)), and horizontal slices ([Figure 49](#), [Figure 50](#), [Figure 51](#), and [Figure 52](#)) can help to yield a clear grasp of the Alingsås site. Those slices also cover the different characteristic parts of the MIP-sounding area.

By inspecting these figures, one of the most apparent features is that the contaminants (PCE, TCE, and cDCE) mainly accumulate at the lower part of the quaternary layer and even contact the bedrock surface. However, whether the contaminants have penetrated into the bedrock remains unknown. It depends on the situation of fractures on the bedrock surface. It is also unlikely to conduct the bedrock drilling at the Alingsås site since nobody wants to risk creating the synthetic fractures for the contaminants and worsen the situation.

Also, the contaminant plume has a much wider horizontal extension by contrast with the vertical extension. This probably thanks to the existence of the clay layers in the subsurface. Firstly, due to the high density of the DNAPL, the contaminants will continue migrating vertically until a layer of low permeability is confronted. However, instead of staying steady at that low-pervious zone, the contaminants will move laterally and seek for the possible pathways that permit its penetration into a deeper zone. This is owing to its relatively high hydraulic conductivity which has been numerically described in [section 2.2](#). Secondly, with the horizontal hydraulic conductivity five to ten time higher than the vertical hydraulic conductivity (Bouwer, 1978), the contaminants spread much faster in the horizontal direction than on the vertical direction.

In addition to the general characteristics discussed above, some local features are also marked out with dashed-line boxes in the vertical slices. However, it is extremely hard to give answers to all these detailed features instantly with the limited information provided. The likely concurrent existing phases at the field demand many more investigations at the site before the exact transport mechanism is understood. However, some of the features are still of great interest to be discussed here.

Inspect the slices cut along the profile 1, the highest concentration zone of PCE can be found in dashed-line box ② in [Figure 38](#). Sharp concentration contrasts can be noticed at the MIP-sounding probe 16 and 17. It is hard to decide how exactly the PCE plume progressed in the subsurface and started to accumulate at this position. To figure out this process involves the characterization of the contaminants phase as well as a more complete layer information. However, another feature might be of interest. The position of the concentration contrast point of MIP 16 is slightly lower than that of MIP 17. This might be caused by a leftward-dipped clay layer, overlaying a layer consists of coarser material. Due to the lower permeability of the clay, the contaminant plume chose the preferential pathway which is beneath the boundary of two layers. Such dipping clay layer boundary can be proved by the borehole log LU6 and borehole log B6. The coarser material layer of B6 starts at a higher elevation than that of the LU6 borehole. The similar feature can be spotted to the South-West side of the dashed-line box ② in [Figure 38](#). An apparent concentration contrast division fits well with the layer boundary between silty clay and silty fine sand in borehole B5.

In the same figure, the anomalous zone marked out with the dashed-line box ① is a bit mysterious. Since the contaminants cannot be transported upwards due to the higher density, it is not so reasonable to see this obvious higher concentration zone at such a shallow position. Capillary force is once suspected as the reason for this, but in between the anomalous zone and the high concentration zone at the bottom is a zone with fairly lower concentration level. Consequently, such anomaly cannot result from the upward capillary force. Also, from the horizontal slice at the elevation of 68.71 m amsl (see [Figure 49](#)), the MIP-sounding probes 11-25 all show a reasonably lower concentration level. Consequently, the contaminants source of this anomalous zone cannot come from the region inside the facility.

Man-induced interference was deduced as the main reason for this anomaly afterwards. At the site, not only the people in this project conducted the groundwater samplings. Another group of people, from previous investigations, also did the groundwater sampling. However, instead of disposing of the sampled groundwater properly, they poured the water directly onto the land. Accordingly, the contaminants in the groundwater samples slowly settled down from the ground surface and got detected at the shallow part. Similar anomalies can also be found in horizontal slices for TCE and cDCE at the elevation levels of 68.71m and 67.01 m ([Figure 50](#) and [Figure 51](#) respectively).

4.2.3 Groundwater sampling data

In response to the second purpose of the vertical slices, the attention is shifted to vertical slices along profile 3 and profile 4. Although no water sample was taken from the exact same point where the MIP-sounding was carried out, the interpolated concentration values along these two profiles are still believed to be accurate enough to be verified with groundwater chemistry data. Because both of them are situated close to the original MIP-sounding probes within 2-3 meters.

It can be noticed at ease that the legends for the contaminants concentrations in groundwater are quite diverse in comparison with these for MIP-sounding measurement result. For the same contaminant, measured at the same position, the concentration level measured through the water sample tends to be much lower than that measured through the MIP-sounding probe. For example, in [Figure 42](#) for PCE, at the same level where the groundwater samples were taken, the interpolated concentration is around 1000 µg/L. However, the concentrations measured in groundwater samples are about 10 times lower than that, and the PCE concentration measured in groundwater is far from reaching its solubility limits, according to [Table 3](#). Such phenomenon can be found quite often in many other cases as well (Huling and Weaver, 1991). This can be attributed to three main reasons.

Firstly, from the aspect of hydraulics, some diffusional limitations might be involved in the process of organic compounds' dissolution and dilution (Wilson and Conrad, 1984). The detailed factors await for further investigations.

Secondly, the solubility itself is also affected by numerous variables. The temperature, for example, will largely affect the solubility of the contaminants in the water. The given solubility value in [Table 3](#) is under the standard condition when the temperature is 25 °C. However, in the field, the recorded temperature when those samples were taken was about 10 degrees lower than the standard temperature. Though the solubility-temperature curve of these four contaminants is nowhere to be found till now, the temperature factor will certainly contribute to the lower solubility of the contaminants. Feenstra (1990) also pointed out that the presence of other soluble compounds, the heterogeneous distribution of DNAPL in the subsurface, and the potential dilution effect occurring during the long intake length of the monitoring wells could all lead to the lower concentration level in groundwater.

Thirdly, the phases at which the contaminants exist at the certain area and time will also affect how much DNAPL can be dissolved in the groundwater. For example, if the aqueous DNAPL volatilize as gas and fill in the soil pores, not much aqueous DNAPL is left and available to be dissolved in the water phase. The tendency of the volatilization can be numerically described with the Henry's Law constants in [Table 3](#). The higher Henry's constant is the higher possibility of DNAPL being volatilized into the

gaseous phase. Consequently, in comparison with PCE, TCE and cDCE have a much higher tendency of being volatilized. In addition to volatilization, the DNAPL might also partition onto the soil phase. The wettability will then determine how much DNAPL at the soil phase can be substituted out by the groundwater (Wilson, 1990). It is not possible to determine the exact mechanism behind this phenomenon unless more investigation is conducted. Also, it could also be likely that the situation will have been altered by the next investigation is conducted. The longer contact time between the DNAPL and the moving groundwater is expected to promote the dissolution process (Huling and Weaver, 1991).

These mechanisms mentioned above could also serve as an explanation for the unmatched trend of the contaminants concentration variation in different groundwater sampling wells. For example, in [Figure 43](#) for VC, the interpolated VC concentration values are the same everywhere, but the VC concentration levels measured in the water samples taken from different sampling pipes diverge from each other.

4.2.4 Degradation state

Setting aside the investigation conducted by SGI, which evaluated the natural degradation potential of the Alingsås site, a large amount of the degradation products (TCE, cDCE, and VC) could be a strong demonstration for the ongoing natural degradation process at the field. Some very interesting features can be witnessed by generating the iso-surfaces of different contaminants.

[Figure 53](#) exhibits the iso-surfaces generated for PCE, TCE, cDCE, and VC respectively. Due to the extremely high iso-values input for the iso-surfaces generation, the bulks wrapped up by these iso-surfaces represents where the highest concentration body of each contaminant can be found. For instance, the highest concentration body of PCE can be found at the lower part of MIP-sounding probe 3. This corresponds well with the fact that the approximate initial PCE leakage position occurred at this zone (refer to the red solid-line box in [Figure 37](#)).

Worthy of note, the highest concentration bodies of both TCE and cDCE are at the same location, MIP-sounding probe 16. Though the latter one has a slightly higher elevation than that of the former one. Seen from other vertical and horizontal slices cut for TCE and cDCE, the positions of the high concentration zones always overlap with each other. It can be suspected that strong degradation activities have been going on in this zone. But the reason for the slight elevation variation remains unknown.

The highest concentration body of VC is situated at the bottom part of the MIP-sounding probe 32, which is also the edge of the MIP-sounding zone. The VC concentration in this highest concentration body is significantly higher than other parts of the MIP-sounding zone, where the concentration of VC tends to be 10 µg/L almost everywhere.

In addition to the generated iso-surfaces, the “Metabolites/Parent Compounds” ratio is also introduced to evaluate the degradation state at the Alingsås site. MIP-sounding probes located within the dry-cleaning facility generally have lower ratio values. This corresponds well with the location of the leakage source where most of the parent compounds probably exist as dense nonaqueous liquids in the subsurface. The high concentration level of these parent compounds might mask out the degradation activities in the ratio Equation (2.3.1) itself.

Although some extremely high ratio values can be witnessed in MIP-sounding points, it is really hard to say if these ratios authentically indicate higher natural degradation activities have been going on at these positions. First of all, the natural degradation activities should be demonstrated with the biological sampling data which is unfortunately absent from this investigation stage. Also, the ratio value itself only stands for a rough assessment of the degradation state. For example, the ratio might be affected by the mobilities of the contaminants. The degradation product of one zone might move to another zone where no degradation process is happening, but a high ratio value may occur in this zone. Also, some impermeable layers may trap the degradation products from other degradation points. This will also result in the extremely high ratio values in some zones. In all, no definite conclusion should be made according to these ratio values.

4.3 DCIP inversion results

Figure 55 shows the inverted results from line 1 together with geological and chemical reference data. Although no reference data is positioned precisely on the line1, instead, they are located within 2-meter buffer distance. The top layer stands out with manifest higher resistivity values. Such feature can also be witnessed in the other three DCIP lines (Figure 56a, Figure 57a, and Figure 58a). This is probably due to the loose backfilled topsoil. As it is mentioned in section 2.4.3, to install all the subsurface electrodes, trenches along four DCIP lines were dug. The set of data used for the inversion in this thesis work was measured shortly after the trenches were refilled. The uncompacted unsaturated topsoil with its large pores contribute to the relatively higher resistivity of the top layer. Below this high resistive layer, the average resistivity value is below 100 Ω m. This is in agreement with the extensively existing clayey layer according to the geological reference data derived from the nearby borehole logs. However, the slight differences in humidity and grain sizes result in the resistivity variations. For example, the anomaly in dashed line box ① is likely caused by dry clay layer from borehole B7.

The evident anomaly located in the right bottom corner of line 1 (dashed line box ②) can also be witnessed on the right edges of line 2 (dashed line box ② in Figure 56) and line3 (dashed line box ① in Figure 57). Such high anomaly zone is suspected to be caused by the manhole located just outside the right edge of the facility. However, no solid information can be provided regarding this manhole. Further inspection is needed in the field. Also, the location of the anomaly zones is at the edges of these three inverted sections. It is possible that such anomaly is also enhanced by the border effect, but the physical cause of this zone cannot be ruled out. The bottom high resistivity layer follows the bedrock surface well, which attributes to the incorporated boundary information during the inversion. The bedrock boundary information is also incorporated to line 2 during the inversion. However, the higher resistive bedrock layer in the inversion result of line 2 (Figure 56a) is not as evident as that in inversion results along line 1. This implies that there is no sharp resistivity boundary between the bottom of the unconsolidated layer and bedrock surface along line 2. This might be due to fractures existing on the bedrock surface which is filled with the groundwater and consequently shows a relatively lower resistivity value.

In both Figure 55b and Figure 55c, four manifest anomalous zones are visible. However, the high chargeability zone below the bedrock surface can be barely seen after the normalization. This indicates that this high chargeability zone might be caused by the high bulk resistivity. Another possible source of high chargeability value is the bottom sandy clay mixture layer, according to the nearby borehole such as B6 and B7. The fine sand may get clogged in the narrow pore throat of clay and cause strong IP effect. However, it cannot be demonstrated here since no borehole logs are exactly on the line. Also, the 3D effect from the dry-cleaning building cannot be totally ruled out. The distance between the line1 and the facility building is only about 1 meter and the edge of the bedrock high chargeability zone stops at B7, which is also at the edge of the facility building. With all these possibilities, it is not inclined to draw any conclusions from this high chargeability zone.

Figure 56 shows the inverted results from line 2 superposed with geological and chemical reference data. Different from line1, most of these reference data is perfectly situated on the line2, which makes the interpretation more convinced. In Figure 56a, two anomalous points with higher resistivity values can be witnessed in dashed line box ①. The location of these two anomalies corresponds well with the location of TDR sensors (shallow black points in Figure 56d). These TDR sensors are used to trace the soil moisture changes and the higher resistivity might be caused by the insulated shell.

Two vertical lower resistive zones can also be noticed in Figure 56a, marked out with dashed line boxes ③ and ④. These two zones also bear extremely high chargeability (dashed line boxes ⑤ and ⑥ in Figure 56b). They are also visible in the normalized chargeability profile (dashed line boxes ⑨ and ⑩ in Figure 56c). Due to the limited information provided, three conjectures can be brought up:

Assumption 1: TDR sensors.

It is still possible that the high chargeability values at the anomaly centre are triggered by the metal part of the TDR sensors. The location of the anomaly zone is just slightly lower than that of the TDR sensors and the long vertical anomaly might be as a result of the artefacts. However, such artefacts seem to be too deep, and the IP response might be too strong to be an artefact.

Assumption 2: Microbial activities.

Though no evident clue can be concluded from the corresponding chemical reference data (Figure 56d), the relatively high degradation state ratio on MIP-sounding probe 20 and MIP-sounding probe 17 might indicate the intense microbial activities at these two zones (Figure 54c). The acid environment resulted from the intense bacterial actions on hydrocarbons will promote the dissolution of the surroundings and produce leachates with higher conductivity (Sauk, 1998). This can thus explain the two vertical zones with lower resistivity values. However, such high IP response and lower resistivity behaviour do not happen to MIP16, where the degradation state ratio is also extremely high.

Assumption 3: leaking pipes.

As can be noticed in Figure 56d, a piece of pipe crosses the line 2 about 2 meters below the ground surface. The two vertical zones with higher IP responses as well as the lower resistivity values might be due to the leaky liquid and metallic pipe corrosion from two leaking points on the pipe. Also, this might also explain the high IP response at the bedrock surface, which was also not removed after the chargeability normalization. The lower resistivity liquid also results in the lower resistivity zone on the bedrock surface. Even if several boundary information points are incorporated into the inversion process, the division between two layers can be hardly seen in this line 2. Another proof comes from the comments of the LU7's borehole log. At the range between 2-6 meters below the ground surface, the description of the geological samples was "grey, very wet, liquid sample". The similar comments can also be found on LU4's borehole log. The description of the bottom sample was "grey, a lot of water". However, the water samples taken from these two groundwater sampling wells did not show a very high conductivity value. Consequently, it remains unsure if the pipe leakage is the actual case here.

The general high chargeability seen in Figure 56b cannot be determined if it is caused by the overall high clayey materials or the 3D effect from the facility, since the line 2 is still quite close to the building with an approximately 4-meter distance.

The inversion results from Line 3 and Line 4 share some similarities. For example, the bedrock layers are considerably obvious without the incorporation of the boundary information. Also, the surface high resistive layers are more apparent in these two lines, in comparison with the line 1 and line 2. This is probably due to the layer of gravelly macadam as well as the top man-made asphalt surface. One interesting feature that can be noticed in both lines is that the shape of the bottom high resistive layer fits well with that of the interpolated contaminants plume. However, several doubts should still be held towards such behaviour. Firstly, the high resistive zone at the bottom appears in conjunction with the bedrock layer, and no clear division can be seen between the interpolated contaminant plume as well as the bedrock surface. Such well-fit trend might just be a coincidence of the inversion artefact due to the lower data resolution level in the deeper part of the subsurface. Secondly, the high resistive responses are usually found in cases when the contaminants appear as the free-phase contaminants, identified from the soil samples, such as the site investigation done by Johansson et al. (2015), and lab analysis done by Orlando and Renzi (2015). In this case, the location of the DCIP line 4 is relatively far away from the source of the leakage. There is a low chance that the contaminates along this line exist as free-phase. On the other side, the contaminants plume is a result of the MIP-sounding measurements interpolation, which means the shape of the contaminants plume might not represent the authentic contaminants distribution.

The relatively high chargeability zones in Figure 57b and Figure 58b are hardly visible in corresponding normalized chargeability profile sections (Figure 57c and Figure 58c). This is probably due to the relatively high resistivity values in these zones, which does not reflect the actual IP effect. Also, the left anomalies in normalized chargeability profile sections are likely caused by the bulbous effect.

Overall, the inversion results from the DCIP measurements do not show a strong correlation with the geochemistry data. Although some high IP response zones and high resistive layers are suspected to have connections with contaminants plume, the existing contradictions and limited information cannot fully stand for the conjectures.

The first two DCIP lines are closely situated nearby the dry-cleaning facility building and the 3D effects from the building can be more or less noticed in the inversion results of the first two lines. The extensive clay material at the field results in the generally low resistivity values at the site, which might also mask out the higher resistive contaminants. Also, the mixture of clay material with sand and gravels has a high IP effect potential, which also makes it hard to distinguish the contaminants from the induced polarization.

The existing pipes in the subsurface are hardly discerned in the resistivity measurements, which is probably caused by the surrounding low resistive clays. In line 2, two strong IP anomalies are suspected to be the leakage points of the pipe, which is also sponsored by comments from the nearby borehole logs. However, due to the poor information provided about the pipes situations, no inclined conclusions can be drawn from it.

In spite of the poor correlation between the DCIP inversion results and the geochemistry data in this baseline measurement, the possible changes in inversion results are believed to be visible after the pilot injection. However, such change can be caused by both the enhanced degradation activities, and injection itself. The former one, due to the biological activities, should result in the decrease of resistivity values. The resistivity changes caused by the latter one is hard to predict with the limited information provided at this stage. On the one side, one of the injection products such as ERD-CH4TM consists of conductive substances (iron for example), and these conductive substances will decrease the subsurface resistivity. On the other side, the injection itself will loose the soil formation during the process, which will raise the subsurface resistivity on the contrary. Consequently, further investigations are needed to isolate the DCIP response to the enhanced degradation activities only.

5. Conclusions and Recommendations

5.1 Conclusions

This thesis work constructs a refined three-dimensional geological model of a chlorinated hydrocarbon contaminated site in Alingsås via GeoScene3D. This refined 3D model includes geological layers, soil and water chemistry data from groundwater samplings and MIP-soundings, as well as the geophysical measurement results (DCIP inversions). Such entirety offers a better site visualization, as well as facilitate the verification of different types of data. This thesis work mainly evaluates the three-dimensional distribution behaviours of the contaminants and correlates the baseline DCIP measurements with the superposed geological and geochemistry data. Through the contaminants distribution visualization, we can draw following conclusions:

- Most halogenated hydrocarbons concentrate on the lower part of the unconsolidated layer. In some locations, the high concentration zones closely touch the bedrock surface. However, it remains unknown if the contaminants have penetrated into the bedrock layer.
- In the latest set of measurement, the highest PCE concentration point is found inside the facility building, which corresponds well with the source of leakage. The highest concentration points of TCE and cDCE are found at the same position right outside the facility, with a slight difference in elevation level. VC generally has a relatively low concentration over the whole region but a zone with extremely high concentration is found at the MIP-sounding probe 32.
- Contaminants found in groundwater samples are much lower than the that derived from the MIP-sounding probes. Three assumptions are made towards this difference, but the confirmation demands further investigations.

The DCIP inversion results over four buried horizontal lines are verified with superposed geological and geochemistry data. However, strong correlations can be hardly found between contaminants and DCIP responses. Some conjectures were put forward towards anomalies, but no inclined conclusion can be made due to limited information.

5.2 Recommendations

Firstly, more precise terrain data is needed to yield a more accurate top boundary for the refined geological model. In some geochemistry data measurements such as MIP-soundings, the measured data is given by the depth below the ground surface instead of the absolute elevation based on the mean sea level. The inaccurate terrain data will result in the mistaken elevations of the geochemistry data.

Secondly, bedrock surface can be refined by another geophysical method, such as seismic refraction. The refined bedrock layer can provide a more accurate estimation of the volume of the contaminated soil at the certain range of concentration level. Also, the boundary information can be incorporated into all four DCIP lines and produce a more realistic inversion result.

Thirdly, the groundwater level calibration is needed due to the possible artesian aquifer condition. The directly inspected free water table from groundwater sampling wells cannot reflect the authentic groundwater level condition at the Alingsås site.

Last but not the least, the future inversion results are better to be correlated with the more recent geochemistry reference data, in case of the changing geochemistry data due to the ongoing degradation process. 3D inversions can also be attempted which might eliminate the 3D effects witnessed in the 2D inversion results.

Reference

- AIZEBOKHAI, A. P. & OYEYEMI, K. D. 2014. The use of the multiple-gradient array for geoelectrical resistivity and induced polarization imaging. *Journal of Applied Geophysics*, 111, 364-376.
- ALAMRY, A. S., VAN DER MEIJDE, M., NOOMEN, M., ADDINK, E. A., VAN BENTHEM, R. & DE JONG, S. M. 2017. Spatial and temporal monitoring of soil moisture using surface electrical resistivity tomography in Mediterranean soils. *CATENA*, 157, 388-396.
- ATEKWANA, E. A. & ATEKWANA, E. A. 2010. Geophysical Signatures of Microbial Activity at Hydrocarbon Contaminated Sites: A Review. *Surveys in Geophysics*, 31, 247-283.
- ATEKWANA, E. A., SAUCK, W. A. & WERKEMA, D. D. 2000. Investigations of geoelectrical signatures at a hydrocarbon contaminated site. *Journal of applied Geophysics*, 44, 167-180.
- BALZARINI, T. 2017. EnISSA campaign WSP SVERIGE AB.
- BENNETT, P., HE, F., ZHAO, D., AIKEN, B. & FELDMAN, L. 2010. In situ testing of metallic iron nanoparticle mobility and reactivity in a shallow granular aquifer. *Journal of Contaminant Hydrology*, 116, 35-46.
- BINLEY, A. 2015. 11.08 - Tools and Techniques: Electrical Methods A2 - Schubert, Gerald. *Treatise on Geophysics (Second Edition)*. Oxford: Elsevier.
- BINLEY, A., SLATER, L. D., FUKES, M. & CASSIANI, G. 2005. Relationship between spectral induced polarization and hydraulic properties of saturated and unsaturated sandstone. *Water Resources Research*, 41.
- BOUWER, H. 1978. *Groundwater hydrology*, McGraw-Hill, 1978.
- BRONDERS, J., VAN KEER, I., TOUCHANT, K., VANERMEN, G. & WILCZEK, D. 2009. Application of the membrane interphase probe (MIP): an evaluation. *Journal of Soils and Sediments*, 9, 74-82.
- CAIRNEY, T. 2002. *Contaminated land: problems and solutions*, CRC Press.
- CHAMBERS, J. E., LOKE, M. H., OGILVY, R. D. & MELDRUM, P. I. 2004. Noninvasive monitoring of DNAPL migration through a saturated porous medium using electrical impedance tomography. *Journal of Contaminant Hydrology*, 68, 1-22.
- CHEN, G. 2004. Reductive dehalogenation of tetrachloroethylene by microorganisms: current knowledge and application strategies. *Applied microbiology and biotechnology*, 63, 373-377.
- DAHLIN, T. & LEROUX, V. 2012. Improvement in time-domain induced polarization data quality with multi-electrode systems by separating current and potential cables. *Near Surface Geophysics*, 10, 545-565.
- DAHLIN, T., WISÉN, R. & ZHANG, D. 3D effects on 2D resistivity imaging—modelling and field surveying results. Near Surface 2007-13th EAGE European Meeting of Environmental and Engineering Geophysics, 2007.
- DAHLIN, T. & ZHOU, B. 2004. A numerical comparison of 2D resistivity imaging with 10 electrode arrays. *Geophysical Prospecting*, 52, 379-398.
- DAHLIN, T. & ZHOU, B. 2006. Multiple-gradient array measurements for multichannel 2D resistivity imaging. *Near Surface Geophysics*, 4, 113-123.
- DAVID P. LESMES, K. M. F. 2001. Influence of pore fluid chemistry on the complex conductivity and induced polarization responses of Berea sandstone. *Journal of Geophysical Research: Solid Earth*, 106, 4079-4090.
- DEGROOT-HEDLIN, C. & CONSTABLE, S. 1990. Occam's inversion to generate smooth, two-dimensional models from magnetotelluric data. *Geophysics*, 55, 1613-1624.
- DOHERTY, R. E. 2000. A History of the Production and Use of Carbon Tetrachloride, Tetrachloroethylene, Trichloroethylene and 1,1,1-Trichloroethane in the United States: Part

- 1--Historical Background; Carbon Tetrachloride and Tetrachloroethylene. *Environmental Forensics*, 1, 69-81.
- EJLSKOV 2017. CAT100/ ERD-CH4 Olé Ego - Injection Summary Memo.
- ELLIS, R. & OLDENBURG, D. 1994. Applied geophysical inversion. *Geophysical Journal International*, 116, 5-11.
- ENGELKE, F. 2007. Alingsåstvädden- Undersökning av potential för naturlig självrening av klorerade alifater vid Alingsåstvädden. SGI.
- EPA 2009. National Primary Drinking Water Regulations. In: AGENCY, U. S. E. P. (ed.).
- FARQUHARSON, C. G. & OLDENBURG, D. W. 1998. Non-linear inversion using general measures of data misfit and model structure. *Geophysical Journal International*, 134, 213-227.
- FEENSTRA, S. Evaluation of multi-component DNAPL sources by monitoring of dissolved-phase concentrations. Proceedings of the Conference On Subsurface Contamination by Immiscible Fluids, International Association of Hydrogeologists, Calgary, Alberta, 1990.
- FETTER, C. W. 2013. *Applied Hydrogeology: Pearson New International Edition*, Pearson Education Limited.
- GAZOTY, A., FIANDACA, G., PEDERSEN, J., AUKEN, E. & CHRISTIANSEN, A. V. 2013. Data repeatability and acquisition techniques for time-domain spectral induced polarization. *Near Surface Geophysics*, 11, 391-406.
- GEOPROBE-SYSTEMS®. 2018. *MIP (Membrane Interface Probe)* [Online]. Available: <https://geoprobe.com/mip-membrane-interface-probe> [Accessed 02/21 2018].
- GILL, R. 2010. *Igneous rocks and processes: a practical guide*, John Wiley & Sons.
- GLASGOW, T. G. S. O. 2007. *Igneous Rocks* [Online]. Available: <https://www.geologyglasgow.org.uk/local-rocks/igneous-rocks/> [Accessed 06/06 2018].
- GLOVER, P. 2015. Geophysical properties of the near surface Earth: Electrical properties.
- GOOGLEMAPS. 2018. *Google Maps*. [Online]. Available: <https://www.google.com/maps/place/Alingsås/@57.9309199,12.5293658,14.54z/data=!4m5!3m4!1s0x46454db45f82dc37:0x4019078290e91c0!8m2!3d57.9300205!4d12.5362113> [Accessed 06/16 2018].
- GUÉGUEN, Y. & PALCIAUSKAS, V. 1994. *Introduction to the Physics of Rocks*, Princeton University Press.
- HAGLUND, K. 2010. Tvätteriet Alingsås-Avslutande provtagning av klorerade alifater samt utvärdering och förslag till vidare hantering. Statens Geotekniska Institute (SGI).
- HAGLUND, K., LARSSON, L., ENGELKE, F. & ARVIDSLUND, O. 2012. Praktikfall Tvätteriet Alingsås-utvärdering av metoder för undersökning och provtagning av klorerade alifater. SWEDISH GEOTECHNICAL INSTITUTE.
- HULING, S. G. & WEAVER, J. W. 1991. *Dense nonaqueous phase liquids*, Superfund Technology Support Center for Ground Water, Robert S. Kerr Environmental Research Laboratory.
- IARC. 2015. *List of classifications in alphabetical order* [Online]. Available: <http://monographs.iarc.fr/ENG/Classification/ClassificationsAlphaOrder.pdf> [Accessed 06/06 2018].
- JIA, C., SHING, K. & YORTSOS, Y. 1999. Visualization and simulation of non-aqueous phase liquids solubilization in pore networks. *Journal of Contaminant Hydrology*, 35, 363-387.
- JOHANSSON, S. 2016. *From microstructure to subsurface characterization. Spectral information from field scale time domain induced polarization*. Licentiate, Lund University.
- JOHANSSON, S. 2017. Resistivity and induced polarization. *Field investigation methodology*. Live@Lund.
- JOHANSSON, S., FIANDACA, G. & DAHLIN, T. 2015. Influence of non-aqueous phase liquid configuration on induced polarization parameters: conceptual models applied to a time-domain field case study. *Journal of Applied Geophysics*, 123, 295-309.
- KAYA, A. & FANG, H.-Y. 1997. Identification of contaminated soils by dielectric constant and electrical conductivity. *Journal of Environmental Engineering*, 123, 169-177.

- KELLER, G. V. 1959. Analysis of some electrical transient measurements on igneous, sedimentary and metamorphic rocks. *Overvoltage Research and Geophysical Applications*.
- KNIGHT, R., NUR, A. & RAISTRICK, I. Modelling the electrical response of sandstones with an equivalent circuit. SPWLA 26th Annual Logging Symposium, 1985. Society of Petrophysicists and Well-Log Analysts.
- LANTMÄTERIET, K. 2009. *Lantmäteriets översiktskarta. Höjddata* [Online]. Available: <https://zeus.slu.se/get/?drop=get> [Accessed 06/16 2018].
- LERNER, D., KUEPER, B., WEALTHALL, G., SMITH, J. & LEHARNE, S. 2003. An illustrated handbook of DNAPL transport and fate in the subsurface.
- LIMA, A., PLANT, J., DE VIVO, B., TARVAINEN, T., ALBANESE, S. & CICHELLA, D. 2008. Interpolation methods for geochemical maps: a comparative study using arsenic data from European stream waters. *Geochemistry: Exploration, Environment, Analysis*, 8, 41-48.
- LINAK E, L. A., YOSHIDA Y 1992. *Chlorinated Solvents*. In: *Chemical Economics Handbook*, Menlo Park, CA.
- LIVSMEDELSVERKETS, F. O. Ä. I. 2017. Livsmedelsverkets föreskrifter om ändring i Livsmedelsverkets föreskrifter (SLVFS 2001:30) om dricksvatten.
- LOKE, M. H. 2016. *Tutorial: 2-D and 3-D electrical imaging surveys* [Online]. Available: www.geotomosoft.com [Accessed 14/02 2018].
- LOKE, M. H. 2018. *RE: Personal comment: Inversion of 2D line with buried electrodes in Res2Dinv*.
- LOKE, M. H., ACWORTH, I. & DAHLIN, T. 2003. A comparison of smooth and blocky inversion methods in 2D electrical imaging surveys. *Exploration Geophysics*, 34, 182-187.
- LUNDIN, C. 2017. Lägesbeskrivning av arbetet med efterbehandling av förorenade områden 2016 In: ENERGI-DEPARTEMENTET, M.-O. (ed.). Naturvårdsverket.
- MARSHALL, D. J. & MADDEN, T. R. 1959. INDUCED POLARIZATION, A STUDY OF ITS CAUSES. *GEOPHYSICS*, 24, 790-816.
- MILIEU LTD, Ö., RISK & POLICY ANALYSTS (RPA) AND RIVM 2017. Study for the strategy for a non-toxic environment of the 7th Environment Action Programme. European Commission.
- MIRACHL. 2017. *MIRACHL* [Online]. Lund university. Available: <http://mirachl.com/> [Accessed 12.05 2017].
- MJONES, L. 1984. Diagram of zeta potential and slipping planeV2 in a dispersion medium. Wikimedia Commons.
- NATURVÅRDSVERKET. 2005. *The Swedish EPA-Contaminated sites* [Online]. Available: http://www.iccl.ch/download/meeting_paris_05/sweden.pdf [Accessed 09/02 2018].
- NATURVÅRDSVERKET. 2012. *Sweden's Environmental Objectives—An Introduction* [Online]. Available: <http://www.swedishepa.se/Documents/publikationer6400/978-91-620-8620-6.pdf> [Accessed 08/02 2018].
- NAUDET, V., GOURRY, J.-C., MATHIEU, F., GIRARD, J.-F., BLONDEL, A. & SAADA, A. 2011. 3D Electrical Resistivity Tomography to locate DNAPL contamination in an urban environment. *EAGE Near Surface 2011, 17th European Meeting of Environmental and Engineering Geophysics*. Leicester, United Kingdom.
- OLDENBURG, D. W. & LI, Y. 1994. Inversion of induced polarization data. *GEOPHYSICS*, 59, 1327-1341.
- OLSSON, P.-I., DAHLIN, T., FIANDACA, G. & AUKEN, E. 2015. Measuring time-domain spectral induced polarization in the on-time: decreasing acquisition time and increasing signal-to-noise ratio. *Journal of Applied Geophysics*, 123, 316-321.
- ORLANDO, L. & RENZI, B. 2015. Electrical permittivity and resistivity time lapses of multiphase DNAPLs in a lab test. *Water Resources Research*, 51, 377-389.
- PELTON, W., WARD, S., HALLOF, P., SILL, W. & NELSON, P. H. 1978. Mineral discrimination and removal of inductive coupling with multifrequency IP. *Geophysics*, 43, 588-609.
- REYNOLDS, J. M. 2011. *An Introduction to Applied and Environmental Geophysics*, Wiley.

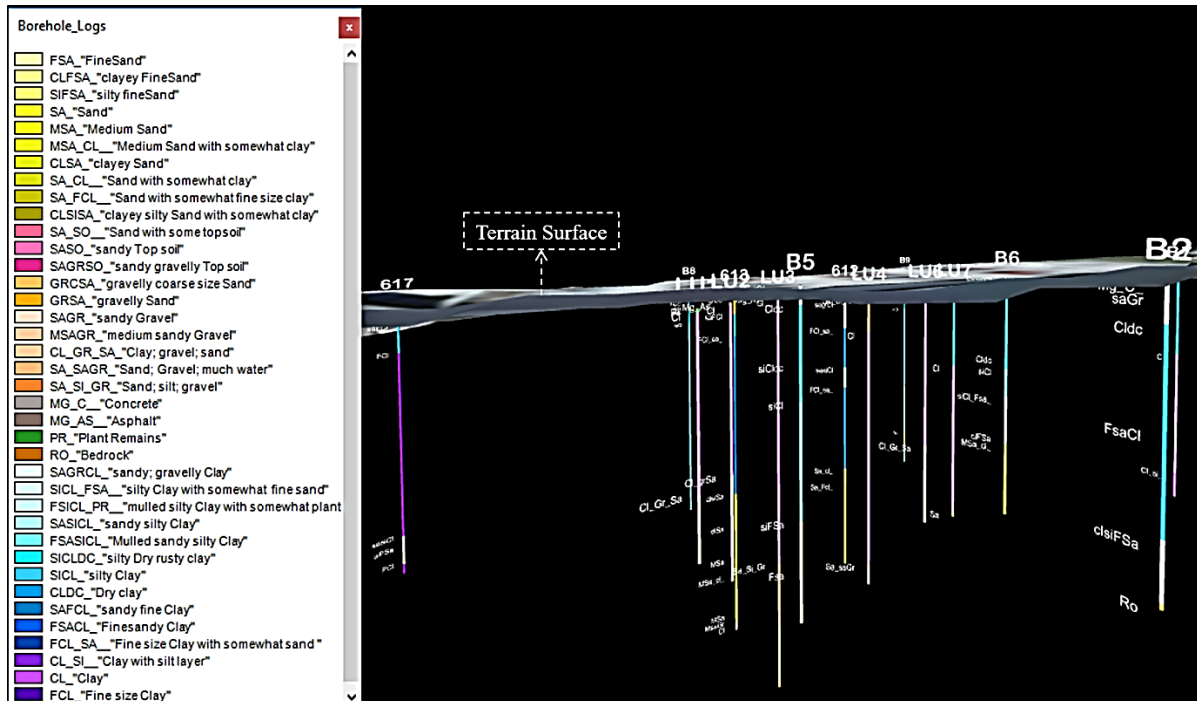
- SASAKI, Y. 1989. Two-dimensional joint inversion of magnetotelluric and dipole-dipole resistivity data. *Geophysics*, 54, 254-262.
- SAUCK, W. A. A conceptual model for the geoelectrical response of LNAPL plumes in granular sediments. Proceedings of the Symposium on the Application of Geophysics to Engineering and Environmental Problems, 1998. 805-817.
- SCOTT, J. B. & BARKER, R. D. 2003. Determining pore - throat size in Permo - Triassic sandstones from low - frequency electrical spectroscopy. *Geophysical Research Letters*, 30.
- SEIGEL, H. O. 1959. Mathematical formulation and type curves for induced polarization. *Geophysics*, 24, 547-565.
- SGF. 2016. *Berg och jord beteckningsblad* [Online]. Available: <http://www.sgf.net/web/page.aspx?refid=2674> [Accessed 06/16 2018].
- SGU. 2012. *Quaternary deposits: 1:25000, Alingsås kommun. SGUs Kartgenerator*. [Online]. Available: http://apps.sgu.se/kartgenerator/maporder_en.html [Accessed 05/26 2018].
- SLATER, L. D. & LESMES, D. 2002. IP interpretation in environmental investigations. *GEOPHYSICS*, 67, 77-88.
- STYLES, P. 2012. *Environmental Geophysics: Everything You Ever Wanted (needed!) to Know But Were Afraid to Ask!*, EAGE.
- SUER, P. & ANDERSSON-SKÖLD, Y. 2011. Biofuel or excavation?-Life cycle assessment (LCA) of soil remediation options. *Biomass and Bioenergy*, 35, 969-981.
- SUMNER, J. 1976. Principles of induced polarization for geophysical prospecting. Elsevier, Amsterdam.
- SUMNER, J. S. 2012. *Principles of induced polarization for geophysical exploration*, Elsevier.
- TOBLER, W. R. 1970. A computer movie simulating urban growth in the Detroit region. *Economic geography*, 46, 234-240.
- TRAVIER, N., GRIDLEY, G., DE ROOS, A. J., PLATO, N., MORADI, T. & BOFFETTA, P. 2002. Cancer incidence of dry cleaning, laundry and ironing workers in Sweden. *Scandinavian journal of work, environment & health*, 341-348.
- WARD, S. H. The resistivity and induced polarization methods. Symposium on the Application of Geophysics to Engineering and Environmental Problems 1988, 1988. Society of Exploration Geophysicists, 109-250.
- WIEDEMEIER, T. H. 1999. *Natural attenuation of fuels and chlorinated solvents in the subsurface*, John Wiley & Sons.
- WIEDEMEIER, T. H., WILSON, J. T., KAMPBELL, D. H., MILLER, R. N. & HANSEN, J. E. 1995. Technical Protocol for Implementing Intrinsic Remediation with Long-Term Monitoring for Natural Attenuation of Fuel Contamination Dissolved in Groundwater. Volume II. PARSONS ENGINEERING SCIENCE INC DENVER CO.
- WILSON, J. L. 1990. *Laboratory investigation of residual liquid organics from spills, leaks, and the disposal of hazardous wastes in groundwater*, Robert S. Kerr Environmental Research Laboratory, Office of Research and Development, US Environmental Protection Agency.
- WILSON, J. L. & CONRAD, S. H. Is physical displacement of residual hydrocarbons a realistic possibility in aquifer restoration. Proceedings of the NWWA/API Conference on Petroleum Hydrocarbons and Organic Chemicals in Ground Water—Prevention, Detection, and Restoration, The Intercontinental Hotel, Houston, Texas, 1984. 274-298.
- WONG, J. 1979. An electrochemical model of the induced - polarization phenomenon in disseminated sulfide ores. *GEOPHYSICS*, 44, 1245-1265.
- WSP 2017. Former dry cleaner "Alingsåstvätten"- Results from MIP-soundings and soil/groundwater sampling, proposal for pilot test.
- XIE, Y., CHEN, T.-B., LEI, M., YANG, J., GUO, Q.-J., SONG, B. & ZHOU, X.-Y. 2011. Spatial distribution of soil heavy metal pollution estimated by different interpolation methods: Accuracy and uncertainty analysis. *Chemosphere*, 82, 468-476.

YAMAMOTO, N., OKAYASU, H., MURAYAMA, S., MORI, S., HUNAHASHI, K. & SUZUKI, K. 2000.
Measurement of volatile organic compounds in the urban atmosphere of Yokohama, Japan,
by an automated gas chromatographic system. *Atmospheric Environment*, 34, 4441-4446.

ZVI, I. Z.-V. I. 2016. Provect-IR™ Antimethanogenic ISCR Reagent.

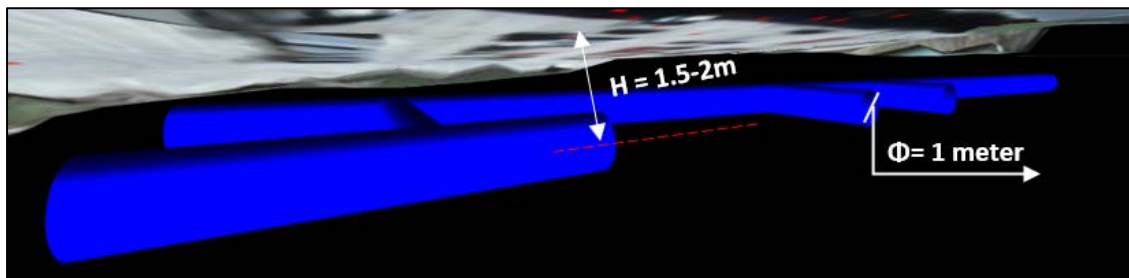
Appendix A. 3D Vision Clips in GeoScene3D

A-1. 3D vision of borehole logs in GeoScene3D



Appendix i. The 3D vision of borehole logs in GeoScene3D together with the legend for geo symbols.

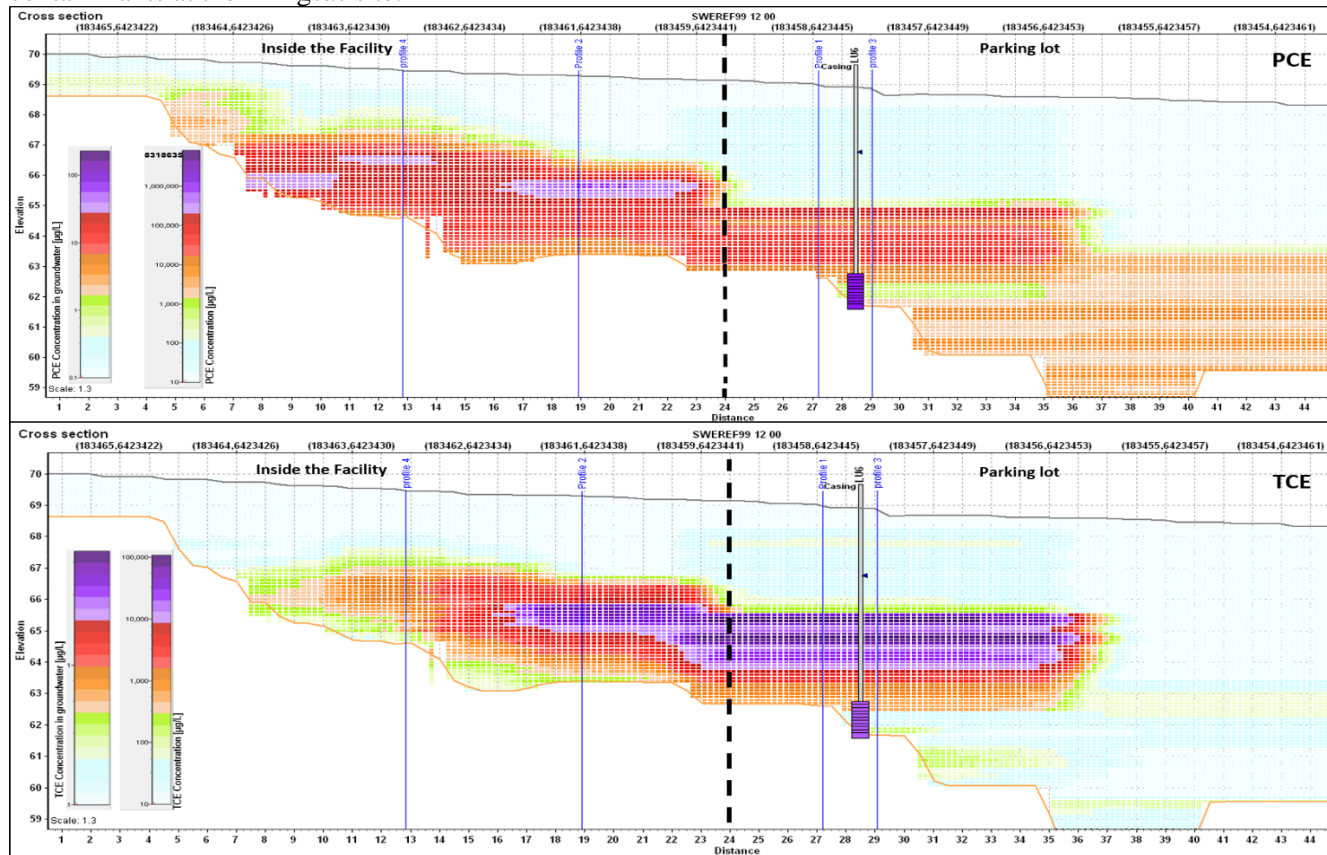
A-2. 3D vision of borehole logs in GeoScene3D



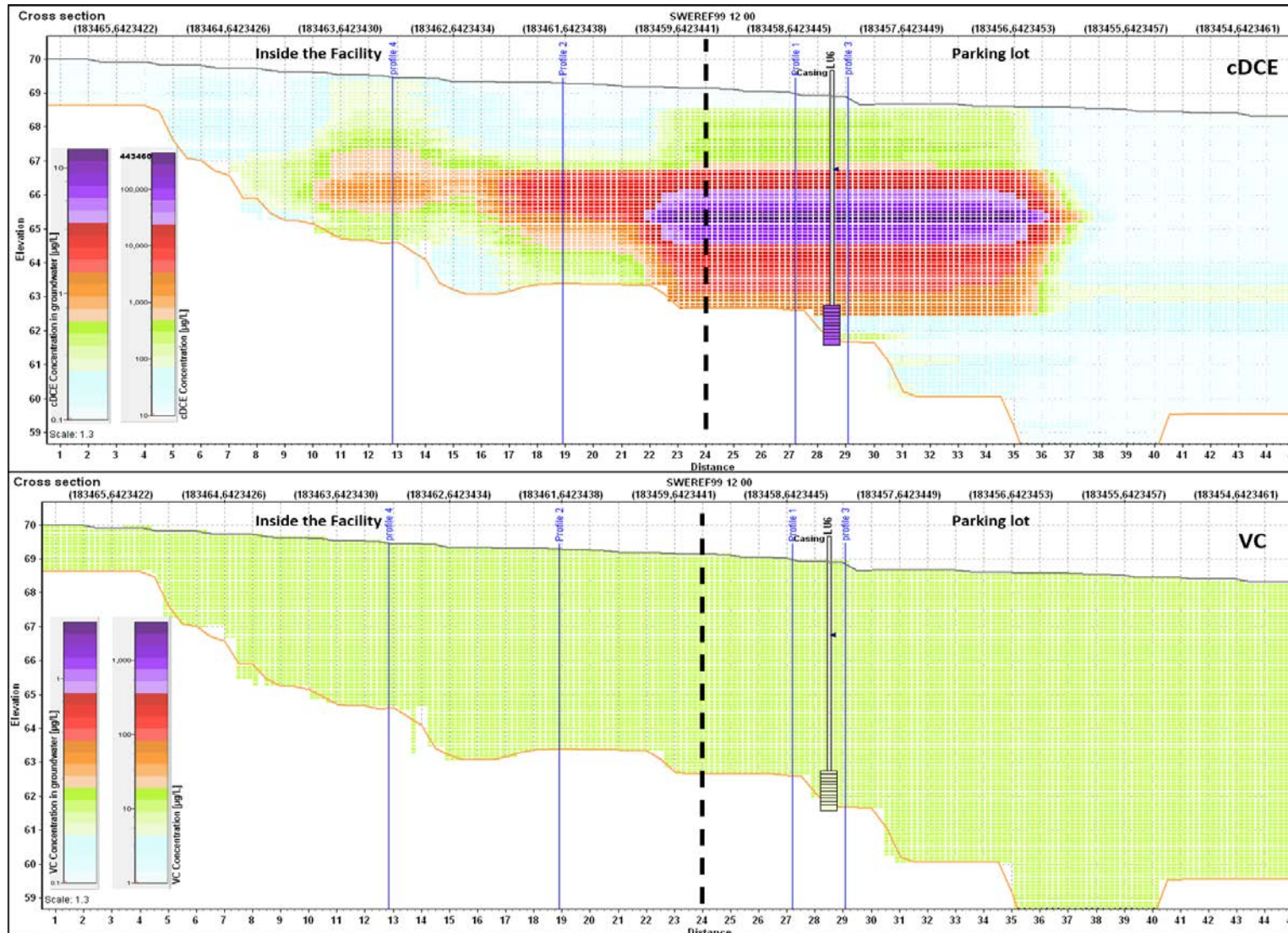
Appendix ii. The 3D vision of the storm-water pipes at the Alingsås site via GeoScene3D. The assumed diameter of the storm-water pipe is 1 meter and the depth of the pipe ranges from 1.5m to 2m below the ground surface due to the topography variation.

Appendix B. Vertical Slices Along the Cross-section

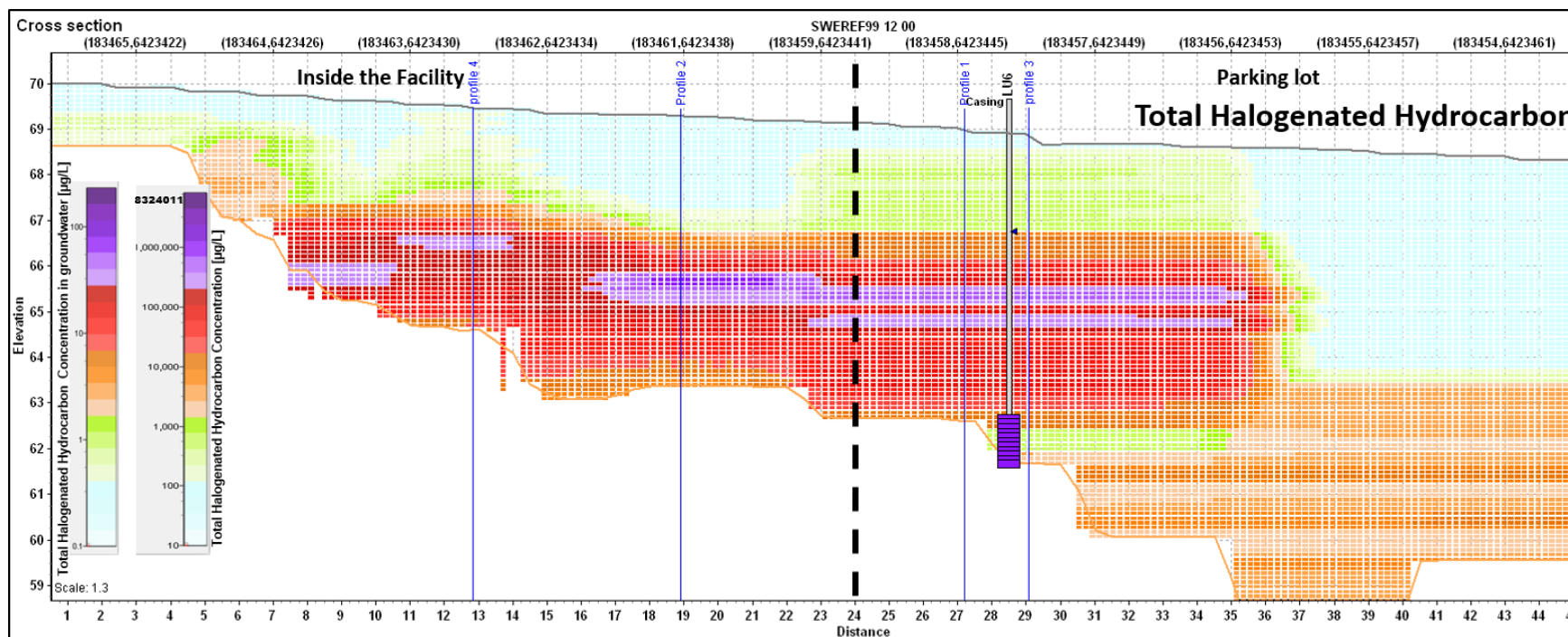
Appendix B displays the vertical slices along the cross-section in [Figure 37](#) by contaminants. Different from the vertical slices exhibited in [section 3.2.1](#), vertical slices displayed here cross through both the region inside the dry-cleaning facility as well as the parking lot area. It offers an overview of the vertical distribution of contaminants at the Alingsås site.



Appendix iii. Together with Appendix iv and Appendix v are vertical slices along “cross-section” Appendix iv. Geochemical groundwater data can be referred to personal communication (S. Åkesson, pers.com., 2018-04-05). The black dashed line is the boundary drawn between the inner facility region and the parking lot area. This cross-section also passes through the four profiles displayed in the [section 3.2.1](#). The crossing points with these four profiles are also marked out.



Appendix iv. Together with Appendix iii and Appendix iv. Geochemical groundwater data can be referred to personal communication (S. Åkesson, pers.com., 2018-04-05). The black dashed line is the boundary drawn between the inner facility region and the parking lot area. This cross-section also passes through the four profiles displayed in the Section 3.2.1. The crossing points with these four profiles are also marked out.



Appendix v. Together with Appendix iii and Appendix iv are vertical slices along “cross-section”. Geochemical groundwater data can be referred to personal communication (S. Åkesson, pers.com., 2018-04-05). The black dashed line is the boundary drawn between the inner facility region and the parking lot area. This cross-section also passes through the four profiles displayed in the [section 3.2.1](#). The crossing points with these four profiles are also marked out.

Along with this slice cut, the distributions of all four contaminants vary from each other and some apparent features can be extracted. For example, PCE plume has the widest higher concentration horizontal extension in comparison with the other three, with the highest concentration zone within the dry-cleaning facility. TCE and cDCE plumes have medium horizontal extensions with the latter one slightly wider than the former one. The highest concentration zones of TCE and cDCE cross the boundary between two regions. Though the highest concentration zone of the latter one is about to leave the region within the facility. Also, the zone above the highest cDCE concentration zone has a slightly higher concentration level than the corresponding zones of the other two.

The VC plume has a considerably homogeneous distribution in this slice cut, with a concentration of less than 10 µg/L everywhere.